Implementation of shingled magnetic recording towards a few grains per bit

ANG SHIMING

NATIONAL UNIVERSITY OF SINGAPORE

2013

Implementation of shingled magnetic recording towards a few grains per bit

ANG SHIMING

(B. Eng. Hons.), NTU

A THESIS SUBMITTED

FOR THE DEGREE OF MASTER OF ENGINEERING

DEPARTMENT OF ELECTRICAL AND COMPUTER ENGINEERING

NATIONAL UNIVERSITY OF SINGAPORE

2013

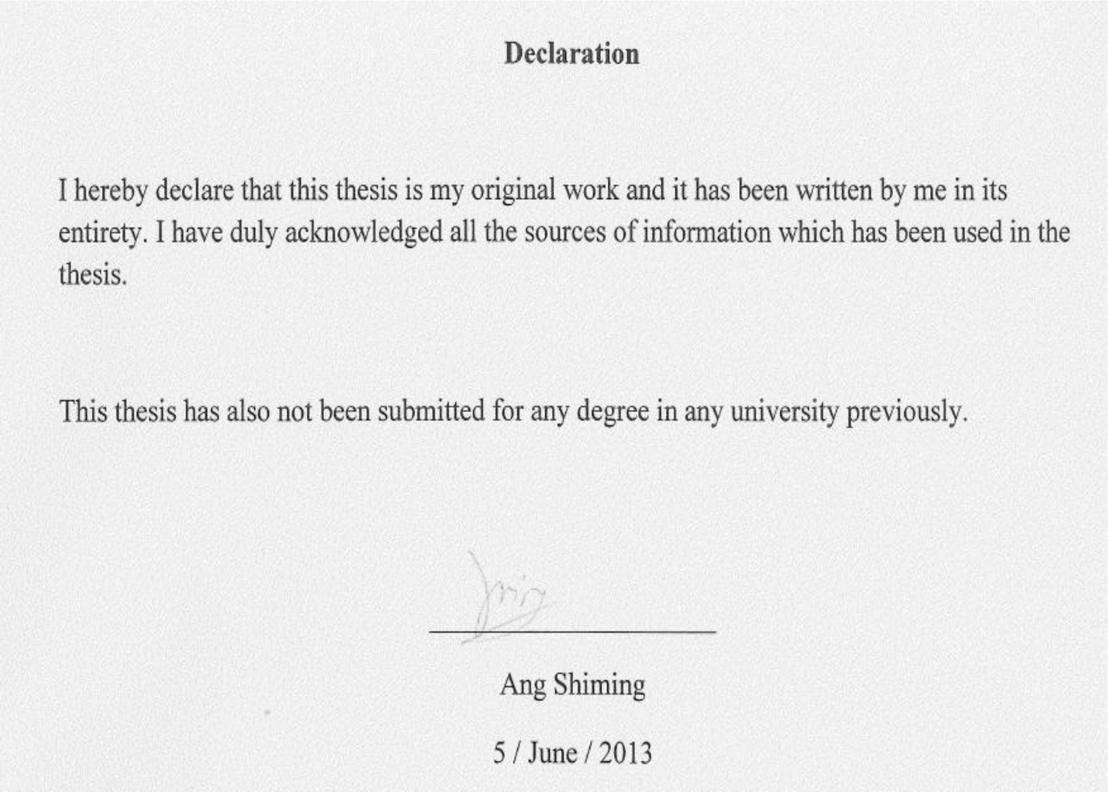

Declaration

I hereby declare that this thesis is my original work and it has been written by me in its entirety. I have duly acknowledged all the sources of information which has been used in the thesis.

This thesis has also not been submitted for any degree in any university previously.

Ang Shiming

5 / June / 2013

Acknowledgement

First and foremost, I would like to thank Dr. Yuan Zhimin for his kind guidance and helpful advice which he extended to me throughout the course of my work and my *M. Eng* studies. Without his patience mentorship and knowledge in the instrumentation and processing methods used in high density magnetic recording, the completion of this thesis would definitely not be possible.

I would also like to thank Dr Pang Chee Khiang for his generosity in providing me with his valuable insights and opportunities that have indeed benefitted me not only in the academic side but also in the work experience side.

Not forgetting my colleagues, Mr. Ong Chun Lian, Mr. Budi Santoso, Mr. Lim Joo Boon Marcus Travis, Dr. Leong Siang Huei that I have worked together with during my course of work in Data Storage Institute (*DSI*), they have greatly helped and supported me and provided much advice and guidance as well, which have made this thesis possible.

Table of Contents

Summary

Current conventional hard disks used for data storage are facing limitations in the push for higher areal density. The magnetic recording tri-lemma and the super-paramagnetic limit are some of the crucial factors limiting the size of the magnetic grains. Shingled writing is seen to be one of the possible cost effective ways to improve the areal density yet without many changes to the current conventional recording media and head structure. This thesis had looked at some of the factors affecting the performance of a conventional recording system before looking at the shingled writing system and the potential areal density gain against a conventional system using a commercial spin-stand.

An introduction of the trend of the hard disk drive technology and its continual areal density growth was first given. The key important issues affecting magnetic recording: the magnetic recording tri-lemma and the super paramagnetic limit were described. With the key issues as a background, key magnetic recording technologies like the longitudinal recording, perpendicular recording, heat-assisted magnetic recording (*HAMR*) and bit-patterned media recording (*BPMR*) were described.

With the knowledge of the key technologies, the thesis proceeded to discuss on read channels. Recording channels like the partial response maximum likelihood (*PRML*), noise predictive maximum likelihood (*NPML*) and pattern dependent noise predictive (*PDNP*) were described. For detection algorithms, maximum a posteriori (*MAP*) based Bahl-Cocke-Jelinek-Raviv (*BCJR*) algorithm, had been compared against the widely implemented maximum likelihood (*ML*) based Viterbi algorithm. Error correction code, linear density parity check (*LDPC*) was also described with brief mention of the Reed Solomon (*RS*) code. For the code based implementations, *LDPC* would be preferred against the *RS* code especially at higher recording densities.

The *PDNP* modification would help to reduce data correlated noise effects. As for the detector, depending on the computational and accuracy requirements, Viterbi or *BCJR* detectors are both possible contenders.

The thesis also looked at the writing process induced media noise which is one of the dominant noise sources in magnetic recording. Transition jitter which is one of the dominant media noise, was also investigated. The medium noise characteristics and jitter distributions across the track at different offset positions for different writing conditions were investigated by varying the write current. Descriptions were given for the different averaging and data processing methods that had been used to analyze the data. Comparisons between two write/read heads were made and the process of determining the better writer and better writing condition was also gone through.

The track edge noise and its impact to bit error rate (*BER*) and off-track read capability (*OTRC*) were subsequently looked into. The writing performance of the recording system was looked at both in the time domain and the spectral domain.

Finally, the implementation of shingled writing and some of the important parameters like the magnetic write width (*MWW*), magnetic read width (*MRW*), erase bands, overwrite and reverse overwrite ratios that characterize a recording system were looked into. Comparing the areal density gain of shingled write vs conventional write systems with a commercial *NPML* channel and spin-stand; for similar media and head configuration, the shingled system was able to achieve an areal density of 775 *Gbpsi* at linear density of 1450 *kBPI* which is much higher as compared to 475 *Gbpsi* at linear density of 1800 *kBPI.*

List of Tables

List of Figures / Illustrations

List of Abbreviations

3*D*	Three Dimensional
AC	Alternating Current
ad	Areal Density
AFC	Anti-Ferromagnetically Coupled
AWGN	Addictive White Gaussian Noise
BAR	Bit-Aspect Ratio
BCH	Bose-Chaudhuri-Hocquenghem
BCJR	Bahl-Cocke-Jelinek-Raviv
BER	Bit Error Rate
bl	Bit Length
BLER	Block Error Rate
BPMR	Bit-Pattern Media Recording
CGC	Coupled Granular/Continuous
DC	Direct Current
e.g.	For Example
*EPR*4	Extended Class-4 Partial Response
GMR	Giant Magneto-Resistance
GPR	Generalized Partial Response
HAMR	Heat-Assisted Magnetic Recording
HDD	Hard Disk Drive
IBM	International Business Machines Corporation
inf	Infinity
ISI	Inter-Symbol Interference
ITI	Inter-Track Interference

ld	Linear Density
LDPC	Low-Density Parity-Check
LMS	Least Mean Square
MAP	Maximum A Posteriori
MD	Middle Diameter
ML	Maximum Likelihood
MLSD	Maximum Likelihood Sequence Detection
MMSE	Minimum Mean Square Error
MR	Magneto-Resistance
MRW	Magnetic Read Width
MWW	Magnetic Write Width
NLTS	Non-Linear Transition Shifts
NO	Negative Offset
NP	Non-Deterministic Polynomial Time
NPML	Noise-Predictive Maximum-Likelihood
OTRC	Off-Track Read Capability
PDNP	Pattern Dependent Noise Predictive
PO	Positive Offset
PR	Partial Response
*PR*4	Class-4 Partial Response
PRML	Partial Response Maximum Likelihood
*PW*50	Pulse Width at 50 % Amplitude Point of Channel Step Response
RAM	Random-Access Memory
RS	Reed Solomon
SEM	Scanning Electron Microscope

SNR	Signal to Noise Ratio
SQTP	Squeeze Track Pitch
SUL	Soft Under-Layer
TAA	Track Average Amplitude
TC	Track Center
td	Track Density
TFC	Thermal Fly-Height Control
TGMR	Tunneling Giant Magneto-Resistance
tp	Track Pitch
VCM	Voice Coil Motor

List of Symbols

rpm	Rounds Per Minute
μm	Micro-Metre
E_B	Energy Barrier for Spontaneous Switching
V	Volume of Magnetic Grains
K_u	Anisotropy Constant
k_B	Boltzmann Constant
H_0	Magnetization Head Field
M_s	Saturation Magnetization
$FeCo$	Iron Cobalt
μ_0	Vacuum Permeability
T	Tesla
$\tau_{stability}$	Thermal Stability Factor
$Tbpsi$	Tera-Bits per Inch Square
D	Delay Operator
t_k	Sampling Time Instance, k
λ	Lagrange Multiplier
k-byte	Kilo-Byte
k-bit	Kilo-Bit
$GF(2)$	Modulo – 2 Operation
XOR	Exclusive OR Operation
AND	AND Operation
$I_{(n-k)\ by\ (n-k)}$	Identity Matrix
nm	Nano-Metre
$Gb/in2$	Giga-Bits Per Square Inch

v	Velocity
Mbits/*s*	Mega-Bits Per Second
mA	Milli-Ampere
GS/*s*	Giga-Samples Per Second
Gb/platter	Giga-Byte Per Platter
MFlux/*s*	Mega-Flux Per Second
MHz	Mega Hertz
mV	Milli-Volt
μA	Micro-Ampere
mm	Milli-Metre
rps	Rounds Per Second
dB	Decibel
ps	Pico-Second
mW	Milli-Watt
kFCI	Kilo-Flux Change Per Inch
kBPI	Kilo-Bits Per Inch
kbpsi	Kilo-Bits Per Square Inch
PI	Mathematical Constant: Ratio of Circle's Circumference to its Diameter, 3.14159
Gbpsi	Giga-Bits Per Square Inch
SI	Standard Unit
m/*s*	Metre Per Second
Δ	Change

Chapter 1: Introduction

1.1 Trend of hard disk drive (*HDD*) technology

Following the internet boom age in the 1990s and the current prevalent usages of mobile smart phones, more and more digital data are generated and thus there is a need to be able to store the massive digital data generated reliably and cost-effectively. Magnetic recording started to be prevalent in the late 1940s after the World War 2 to the 1980s [1]. That was the age of magnetic tape recording, where strips of magnetic tapes were used to record data and playback data for commercial and industrial purposes.

Magnetic disk drive technology started in the 1950s. The very first magnetic hard disk drive was introduced by International Business Machines Corporation (*IBM*) on September 13, 1956 [2, 3]. The drive system also known as *IBM* 350 was 60 inches long, 68 inches high and 29 inches deep. It was configured with 50 magnetic disks containing 50,000 sectors, each of which held 100 alphanumeric characters, for a capacity of 5 million characters. The disks rotated at 1,200 *rpm*, tracks (20 tracks per *inch*) were recorded at up to 100 bits per *inch*, and typical head-to-disk spacing was 800 micro-inches.

In June 2, 1961, *IBM* introduced the disk storage system, *IBM* 1301 [4, 5]. The key aspect of the breakthrough is the dynamic air-bearing technology, which allowed the read/write head to “float” over the surface of the high speed rotating disk to a head-disk spacing of merely 6 μm. It was the first drive to use heads that were aerodynamically designed to fly over the rotating disk surface on a thin layer of air.

IBM 2310 was the first drive to use the voice-coil motor (*VCM*) technology for accessing heads across the media [6]. *IBM* 3330 [7] was on the other hand the first drive to apply the *VCM* technology to do track-following with the servo system. This allowed the drive to respond to the servo and achieve better track density with high reliability than older drives.

In 1973, *IBM* introduced the *IBM* 3340 disk drive, together with the Winchester technology [8]. The key technology breakthrough was the usage of a smaller and lighter write/read head that has a ski-like head design, thus flying nearer to the media to only 0.4 μm above the surface of the disk [9] which doubled the storage density to nearly 1.7 million bits per square *inch*. The Winchester design which pioneered the use of low cost, low-mass, low-load, landing heads with lubricated disks [10], was one of the key technologies considered to be the father of modern hard disk.

In 1980s, Seagate technology introduced the first hard disk drive, *ST*506 for micro-computers [11]. The disk held 5 megabytes of data and was a full height 5.25 *inch* drive. Rodime made the first 3.5 *inch* rigid disk drive, *RO*352 in 1983 [12], which the 3.5 *inch* size quickly became one of the popular standard form factor for desktops and portable systems. PrairieTek was the first company to come up with the 2.5 *inch* disk drive [13], which the 2.5 *inch* size has become one of the popular standard form factors for portable systems.

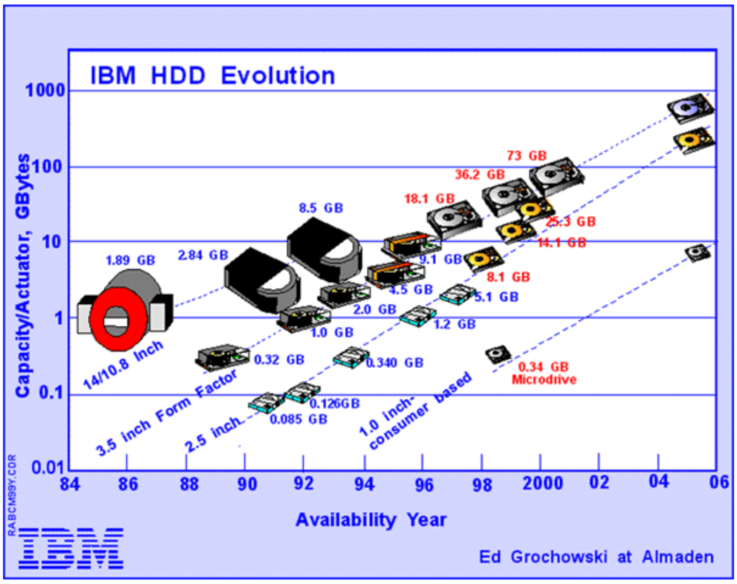

Figure 1 - 1: *IBM* hard disk drives (*HDD*) evolution chart [14]

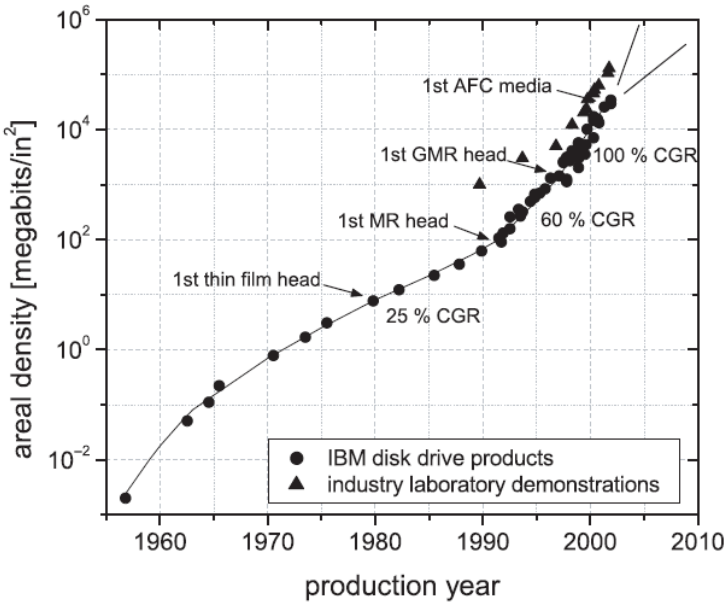

Figure 1 - 2: Areal density progress in magnetic recording and some of the key technology discoveries [15]

Since then, magnetic recording technology has evolved. Due to the high precisions and advancement of the recording head and media technology, the hard disks are able to have high areal density of up to 700 Gbits/$inch^2$ thus the capability to store gigabytes of data per platter. Figure 1-1 shows an informative chart that describes the timeline of the evolution of *IBM HDD*. It shows the different form factors (14/10.8, 3.5, 2.5, 1.0 *inch*) that has evolved since and the capacity of those drives. Figure 1-2 shows the areal density progress in magnetic recording and some of the key discoveries which include the thin film head, magneto-resistance (*MR*) head, giant magneto-resistance (*GMR*) head and the anti-ferromagnetically coupled (*AFC*) media technologies. Note that these above technology mentioned is not an exhaustive list of the key technologies that has affected the hard disk drive industry and that there are many others like the tunneling *GMR* (*TGMR*) head, coupled granular/continuous (*CGC*) media technology etc., which shall not be elaborated as it is not within the scope of this thesis.

1.2 Magnetic recording tri-lemma and super-paramagnetic limit

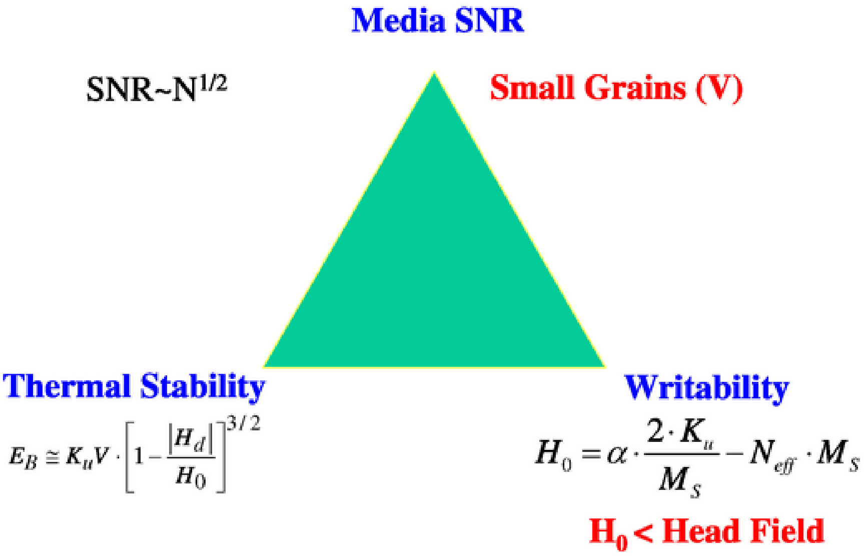

Figure 1 - 3: Magnetic recording tri-lemma issue

In magnetic recording, the tri-lemma issue affects the media and head design. This tri-lemma issue is illustrated in Figure 1-3 [16, 17]. In magnetic recording, small magnetic grains would help to reduce the media jitter noise and improve the signal to noise ratio (*SNR*) significantly (*SNR* is proportional to $N^{1/2}$, where N is the number of grains in a bit). However, the small volume of the small grains is thermally unstable, which will result in unreliable long term storage of data in these media (Energy barrier for spontaneous switching, E_B is proportional to the volume of grains, V). This issue could be resolved by introducing media material with high anisotropy constant, K_u. However, high K_u media would require a higher magnetization head field, H_0 to magnetize it. High H_0 field on the other hand is usually produced by using higher currents or more coils around a soft ferro-magnetic core element that has high saturation magnetization, M_s value. But the writing fields has been remained constant due to material constraints where the *FeCo* material used has a fixed known saturation magnetization, $\mu_0 M_s$ of 2.4*T* [17]. Due to these constraints, there is a need to find a compromise between writability, thermal stability and medium *SNR*.

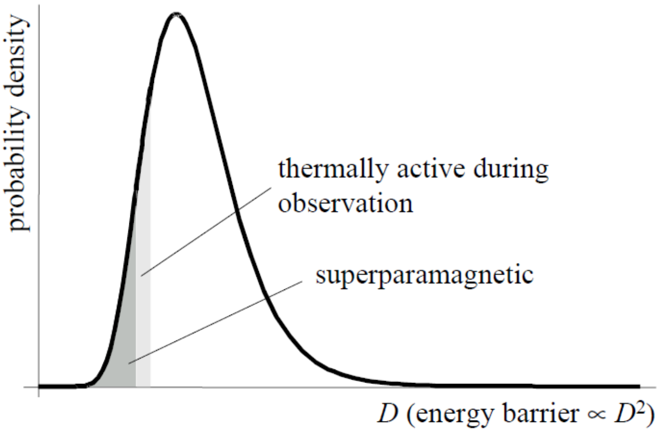

Figure 1 - 4: Illustration of the super-paramagnetic behavior in relation with the energy barrier of the magnetic grains in thin film material

$$\tau_{stability} = \frac{K_u V}{k_B T_1},$$

$$where\ \tau_{stability} \geq 60\ for\ good\ thermal\ stability$$

(1 - 1)

From Figure 1-4, the super-paramagnetic limit occurs when the energy barrier of the magnetic grains are below a certain energy barrier. The energy barrier of the grains is proportional to the terms $K_u V$. Meaning to say if the volume of the grains is made smaller, the probability density against the energy barrier curve of the grains will be shifted to the left and a higher probability of the grains would be in the super-paramagnetic region where the grains will exhibit higher thermal agitation and may not be able to store magnetic transitions reliably. For good thermal stability, depending on the operating temperature in the environment, the thermal stability factor, $\tau_{stability}$ is recommended to be above 60 [18].

With the tri-lemma and super-paramagnetic knowledge as the background, a brief description of the key recording technologies will be given.

1.3 Key recording technologies

1.3.1 Longitudinal recording

Figure 1 - 5: Longitudinal recording and its respective media bit orientation and detected transitions, where demagnetization fields are denoted by the smaller red arrows

For 50 years or so, longitudinal recording has been widely used by the hard disk industry. Figure 1-5 shows the longitudinal recording and its respective media bit orientation and detected transitions. In longitudinal recording, the bits are aligned parallel to the disk surface. Note that the demagnetization fields denoted by the smaller red arrows are also aligned parallel to the magnetization of the media. This implies that the magnetic force by the demagnetization field is also along the same direction. The magnetic head is able to detect the magnetic transitions as it flies along the disk surface. When it encounters a transition between the different bit orientations, the magnetic head will also register a similar jump in the read-back voltage using its sense current detection scheme. Minimal changes of the read-back voltage will be registered when no magnetic bit transitions are detected. With these known behaviors, one could design drives that register the jumps as the different transition region for different bit orientation and thus storing information using the detected signals and written magnetic bit orientation on the media.

There are however issues affecting longitudinal recording. One issue with longitudinal recording is that it faced high demagnetization field at higher recording densities, implying a limit in the recording density. This is due to the magnetic dipoles of opposite orientation being placed nearer and nearer to each other as densities increases, thus increasing the interaction forces in between. This is also one of the serious limitations of longitudinal recording that caused hard disk manufacturers to switch to perpendicular recording technology in the early 2005s [19].

1.3.2 Perpendicular recording

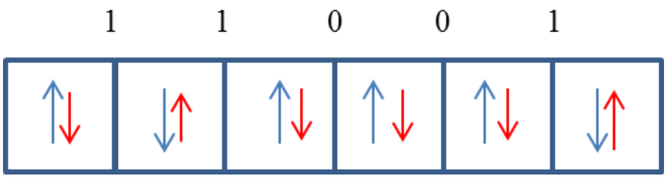

Figure 1 - 6: Perpendicular recording and its respective media bit orientation and detected transitions, where demagnetization fields are denoted by the smaller red arrows

Perpendicular recording [20] was first commercially implemented in 2005. Figure 1-6 shows a diagram of magnetic grains and its respective bit orientation and detected transitions. Note that the magnetic dipoles are arranged perpendicularly to the disk surface. It is this unique orientation that allows the media to have more compact grain structure yet be able to have minimal demagnetization field across the grain boundary. The perpendicular orientation actually allows intermediate grains to have good magnetic coupling as well. Furthermore, current media structure of the perpendicular media includes the soft under-layer (*SUL*). This *SUL* acts as a layer that strengthens the magnetic field produced by the magnetic head to the magnetic layer. What this does is that the magnetic head could be reduced in size thus increasing its resolution but at the same time be able to create enough magnetization field to magnetize the perpendicular media.

However, conventional perpendicular hard disks currently increase the areal density to the stage where they have reduced the grain size to the point that they are reaching the super-paramagnetic limit. In order to overcome the super-paramagnetic limit and continue the push for areal density gains, there is thus a need to consider future technology, which shall be briefly touched on in the following sections.

1.3.3 Heat-assisted magnetic recording (*HAMR*)

HAMR refers to heat-assisted magnetic recording. The working principle of *HAMR* technology is to increase the temperature during writing. By increasing the temperature, the high coercivity media will become writable by the write head. This method of implementation allows the potential usage of high K_u, small grains media that are thermally stable at room temperature yet still remain writable when high heat is applied before or during writing. This technology has in fact been proven to work with a recent 1*Tbpsi* demo by Seagate [21]. Current *HAMR* recording is limited by the switching field distribution and thermal spot size [22]. The *HAMR* technology is still under much research and the cost of developing and integrating the magnetic head with a high power efficient laser heating source, however is still considered high, which is one of the reasons why the perpendicular media recording has not transitioned over to the *HAMR*.

1.3.4 Bit-pattern media recording (*BPMR*)

BPMR is a technology that records data in a uniform array of magnetic grains, storing one bit per grain, as opposed to conventional hard-drive technology, where each bit is stored in a few hundred magnetic grains [15, 16]. The media consists of a periodic array of discrete magnetic elements either prepared artificially by different lithography techniques or self-organized spontaneously. Each element is a bit that is almost isolated from other elements but the magnetization inside the bit is much strongly exchange coupled as compared to the conventional recording media. Therefore, the corresponding energy barrier is larger and the thermal stability is improved. Another advantage of patterned media is that it eliminates the transition noise between bits since the bits are completely separated. However, the cost of making media using lithography remains still a high cost due to the need to use advanced lithography techniques for the high resolution of the bit wells required. In addition, writing/reading of the bits on the media requires much more precision and control techniques.

1.4 Research objective and thesis structure

Unlike the *HAMR* and *BPMR* technology that was described in the previous sections, shingled writing is seen to be one of the possible cost effective ways to improve the areal density yet without many changes to the current conventional recording media and head structure. This explains the rationale of conducting the research on shingled recording in this Master’s Thesis report. In this thesis, the focus will be to look at some of the factors affecting the performance of a conventional recording system before looking at the shingled system and the potential areal density gain against a conventional system using a commercial spin-stand.

This thesis is divided into 5 chapters.

Chapter 1 gives a brief introduction of the trend of the hard disk drive technology and the need to continue the areal density push. The key important issues affecting magnetic recording: the magnetic recording tri-lemma and the super-paramagnetic limit were described. With the key issues affecting the areal density push as a background, key magnetic recording technologies like the longitudinal recording, perpendicular recording, *HAMR* and *BPMR* was briefly described to the reader.

With these as a background, chapter 2 will then proceed to discuss about read channels. This will allow the readers to understand the different types of recording channels available to assist in the decoding of the read-back signal and some of the issues affecting their implementation in the hard disk industry.

Chapter 3 then proceeds to look at the writing process induced media noise which is one of the dominant noise sources in magnetic recording as linear densities increase. Transition jitter which is one of the dominant media noise will also be looked into where the probabilities of transition jitter at different off-track positions will be analyzed.

Chapter 4 will look at the track edge noise and its impact to bit error rates (*BER*) and off-track read capability (*OTRC*). The writing performance of the recording system will be looked at both in the time domain in terms of track average amplitude (*TAA*) and the spectral domain where data is captured using a spectrum analyzer.

Chapter 5 will touch on the implementation of shingle writing and some of the important parameters that characterize a recording system. The experimental result of the potential areal density gain of a shingled system against a conventional magnetic recording system will also be studied.

Chapter 6 will then conclude the findings and provide a brief summary of the work done in this thesis. Recommendations on the future research in this topic will also be touched on in the chapter.

Chapter 2: Read channels

2.1 Introduction

In a recording system, the system is prone to be influenced by different noise sources. The definition of noise implies that it is some undesirable signals that influence the data. Such effects can be random or repeatable and usually uncontrollable but steps could be taken to reduce the effects of noise for example via averaging to remove random noise. In general, there are 3 main types of noise influencing the magnetic recording system. Read noise is usually caused by the random magnetic head and electronics noise when current is passed through the resistant based body. Media noise is often repeatable and related to the magnetic media's grain distribution and magnetic field distribution of the head during the writing process. Pattern dependent noise usually occur due to the effects of similar or opposite neighboring magnetic grains thus causing non-linear pattern dependent transition shifts at the grain boundaries due to the influence of the neighboring demagnetization or magnetic fields . Such noises would corrupt the data during the writing and reading process and thus cause interpretation errors to the user if the user reads back the signal without doing any signal processing or corrections.

In current practical magnetic read-back channels, signal processing is used to process the read-back signal before the data is written and after the data is read-back at the user side. In this chapter, conventional read channels, partial response maximum likelihood (*PRML*) channel will be reviewed upon before looking at more advanced read channels like the low-density parity-check *(LDPC*) channel or pattern dependent noise predictive (*PDNP*) channels.

2.2 *PRML* channel

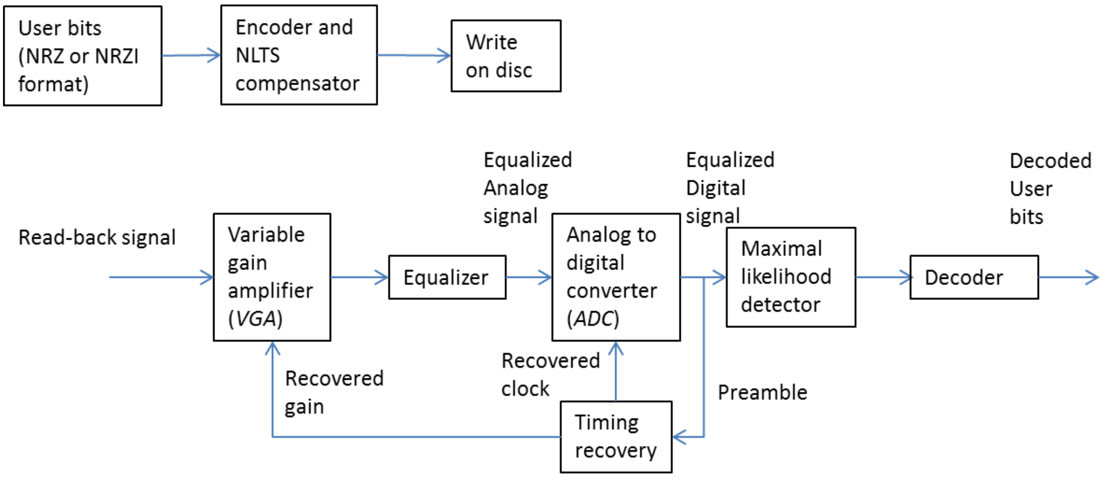

Figure 2 - 1: *PRML* channel configuration

A typical *PRML* channel configuration is shown in Figure 2-1 [23, 24, 25, 26]. *PR* in *PRML* means partial response, while *ML* means maximum likelihood. *PRML* is based on two major assumptions: a) The shape of the read-back signal from an isolated transition is exactly known and determined, b) The superposition of signals from adjacent transitions is linear.

Conversion of the read-back signal to the partial response (*PR*) signaling scheme is required before the signal is passed through the *PRML* channel. This conversion is usually done via an equalizer. Typical *PR* signals used are the *EPR*4, *PR*4. More details about these *PR* signals will be given in the following paragraphs. As for the maximum likelihood (*ML*) detection scheme used, a popular implementation is the Viterbi detector which shall be also further described in the following paragraphs.

2.2.1 *PR* signaling

When a signal is band limited in the time domain, it will have an infinite range in the frequency domain. On the other hand, if the signal is restricted to be band limited in the frequency domain, it will have an infinite span in the time domain. Either way, one has to decide between recovering the overall signal in the time or frequency domain by restricting the signal's band accordingly in its desired domain. It is well known that time domain mixed signals can be recovered via the frequency domain by doing Nyquist sampling. This explains a need to have band limited frequency input signal through a channel for the sampling process to occur effectively. This implies the inevitable need to allow certain amount of inter-symbol interferences (*ISI*s) in the time domain from the individual signals.

What *PR* signal scheme does is that it allows a certain known amount of interference from each signal, and then the equalizer and decoding scheme are designed based on the interferences introduced. For example, Figure 2-2 shows the *PR*4 scheme where the characteristic polynomial is 1-D^2. The *D* operator simply means to delay the signal for one sampling instant. For any equalized *PR*4 signal, it can accommodate 3 distinct values namely [-1, 0, 1] due to the *PR*4 filter configuration. These values could be derived by passing a di-pulse signal through the *PR*4 filter. The *PR*4 scheme is suitable for longitudinal recording and is able to reject away *DC* noise due to its characteristic differential polynomial.

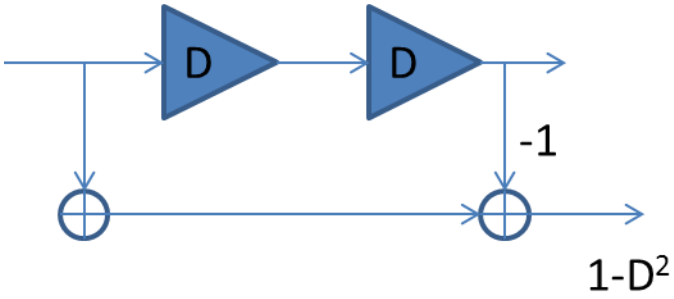

Figure 2 - 2: *PR*4 delay tap representation

Perpendicular recording channels on the other hand are more suited to use the *EPR*4 scheme due to a more matching frequency response plot with the perpendicular systems. The characteristic *EPR*4 polynomial is $1+D-D^2-D^3$. Similarly, the *EPR*4 filter should only produce 5 amplitudes namely [-1, -0.5, 0, 0.5, 1], which could be derived by passing a di-pulse signal through the *EPR*4 filter.

The performance of a *PR* filter could be analyzed via the eye diagram. A random data pattern would be written on the disk and the read-back signal would be passed through the *PR* equalizer. The output of the *PR* equalizer would be synchronized with equalizer sampling clock and repeatedly displayed on the same plot for every sampling period. Depending on the number of characteristic amplitudes, the signal would cut through those amplitude points and if the samples do not overlap each other, “eyes” would appear in the eye diagram plots. Figure 2-3 shows a typical eye diagram for the *PR*4 system [27].

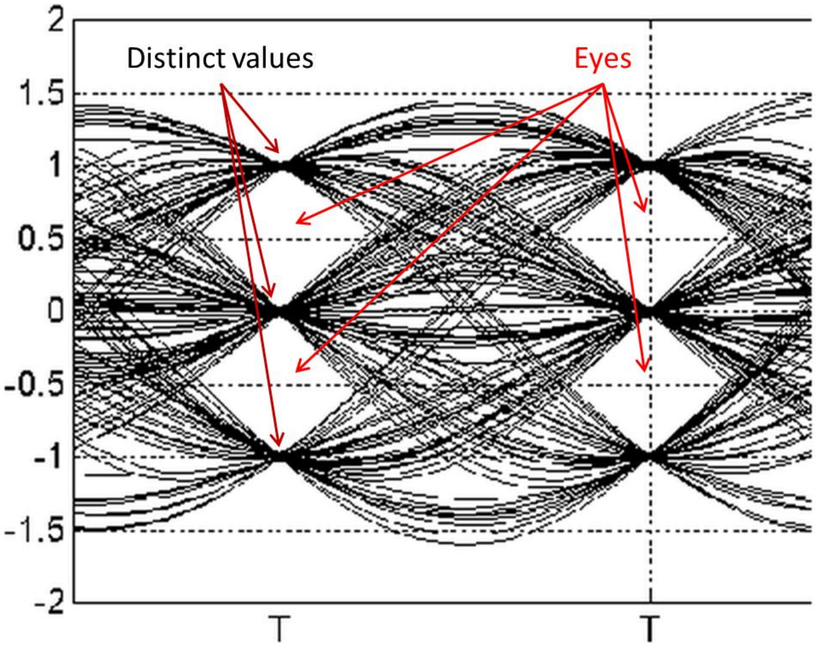

Figure 2 - 3: *PR*4 eye diagram

The performance of the *PR* system could also be evaluated by plotting out the histogram of the output signals. Figure 2-4 shows two separate histograms of the output signals from two different *PR*4 systems [27]. In comparison, plot (*a*) in Figure 2-4 has better performance in terms of the *PR*4 implementation due to its more distinct data histograms as compared to plot (*b*) in Figure 2-4, which has a more varied and spread out distribution.

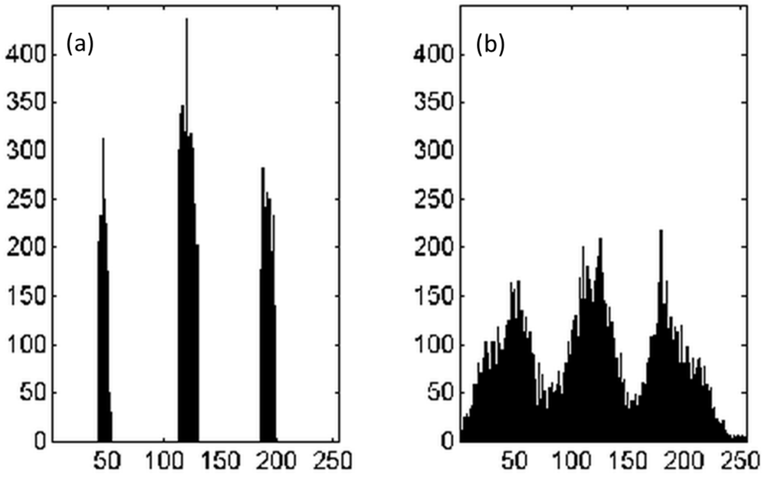

Figure 2 - 4: Two separate histograms for two different *PR*4 systems

Note that at the design stage of the *PR* polynomial, the frequency response of the system response without any *PR* filter implementation should be plotted first and compared with the ideal *PR* target frequency response. This allows analysis of the degree of fitting and allows user to estimate the amount of bandwidth and gain compensated when the *PR* filter is applied to the system [27].

2.2.2 Viterbi detector

After controlled interferences are introduced into the system, it is necessary to have a detection scheme to know what the received transmitted signals are at the detector side. Maximum likelihood sequence detection (*MLSD*) detectors [28] are often used to perform signal detection in *ISI* channels. Viterbi detection is one specialized scheme of maximum-likelihood detectors that is commonly used in hard disk industries. The Viterbi algorithm was proposed by Andrew Viterbi in 1967 as a decoding algorithm for convolutional codes over noisy digital communication links [29]. The Viterbi algorithm is a *ML* algorithm such that it minimizes the error probability between the transmitted and received code-words via probability branch metrics and cost values. It is commonly used for decoding convolutional codes. The algorithm works on states which is a sequence of bits. The detector itself, if based on Viterbi algorithm, has to have prior knowledge of the possible input states, possible transitions to next states and the output result of such transitions.

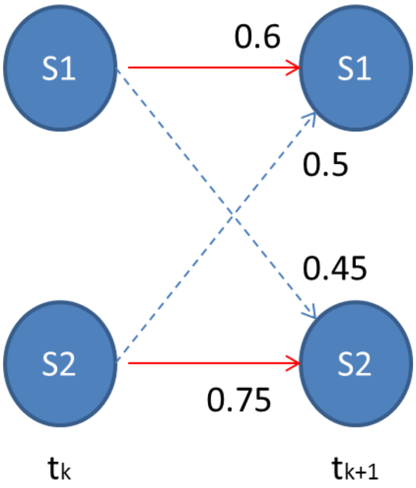

Figure 2 - 5: Illustration of the chosen branches versus ignored branches

The Viterbi algorithm will store a list of the probable paths and transition states. Whenever there are transitions of states, the Viterbi will calculate the metric for the possible branches and the highest probable branch which lead to the next state from a possible valid previous state will be recorded. For example using the illustration from Figure 2-5, the states, $S1$ and $S2$ at t_{k+1} have incoming transitions from $S1$ and $S2$. For

$S1$, there are branch cost values of 0.6 and 0.5 leading to the state. Being a maximum likelihood detector, due to the higher cost value, it will register the transition as $S1$ state at t_k entering the state $S1$ at t_{k+1}. For $S2$ state, it will register the transition as $S2$ entering $S2$. This process will continue until the case where both branches leading to next states come from only one input state. That is when that individual input state will be registered as the detected *ML* output state and all other states at that particular time instant could then be removed. After which, the Viterbi algorithm will continue the decoding process from that input state, if the data set is not fully decoded or if additional signals enter.

2.2.3 Design of equalizers and generalized partial response (*GPR*) targets

2.2.3.1 Equalizers

As described above, before read-back signals are fed back into the Viterbi detector for detection, the signals are required to be processed further to reduce the noise and also to shape the signaling scheme to the desired *PR* scheme. With the knowledge of the input signal, X and output signal, Y, where X and Y are matrices, a simple equalizer made up of delay filter taps with its coefficients equal to A could be derived. (Equation 2-1)

$$Y = A * X$$

$$A = Y * X^{-1}$$

(2 - 1)

However, sometimes multiple solutions might be possible for the system; therefore it is usually common that the minimal possible error be used as a factor to derive the filter taps. Minimization of the Jacobian matrix of the *PR* system with the input signal matrix, s [27] will result in the following equations (Equations 2-2, 2-3):

$$H = s_{Inverse} * s^T * Y^T$$

(2 - 2)

Where

$$s_{ToBInverse} = s^T * s$$

$$s_{Inverse} = matrix\_inv(s_{ToBInverse})$$

$$s_{m\,x\,n}$$

$$= \begin{bmatrix} s_t & s_{t+1} & s_{t+2} & \cdots & s_{t+m-4} & s_{t+m-3} & s_{t+m-2} & s_{t+m-1} \\ s_{t+1} & s_{t+2} & s_t & \cdots & s_{t+m-3} & s_{t+m-2} & s_{t+m-1} & 0 \\ s_{t+2} & s_{t+3} & s_{t+4} & \cdots & s_{t+m-2} & s_{t+m-1} & 0 & 0 \\ \vdots & \vdots & \vdots & \ldots & \vdots & 0 & 0 & 0 \\ s_{t+n-1} & s_{t+n} & s_{t+n+1} & \cdots & 0 & 0 & 0 & 0 \end{bmatrix}$$

where m is the length of the input signal, n is the number of filter taps used

(2 - 3)

These equations 2-2, 2-3 allow the equalizer tap matrix, H to be derived. By applying the matrix on the taps, the filter taps will then try to shape any input signal to the corresponding *PR* polynomial signal.

2.2.3.2 Generalized partial response (*GPR*)

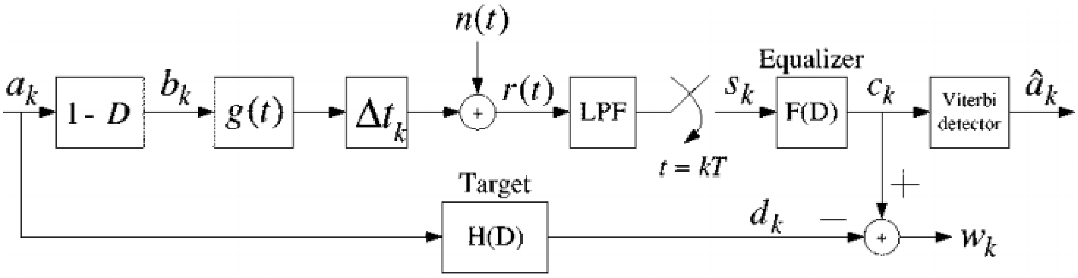

Figure 2 - 6: A generalized partial response channel representation

GPR is considered as a more generalized form of the *PR* target. In comparison, *GPR* has no restriction to holding non-integer values for its filter tap elements and as a result is allowed more versatile shaping of the input signals at the expense of more calculation involved. Figure 2-6 shows a generalized partial response channel representation [30]. In comparison with a partial response system, there is an addition of the feedback loop from the partial response output which is used to subtract against a generalized partial response target *H*(*D*). This additional feedback loop allows the system to retrieve the difference, w_k between *PR* system output, c_k and ideal *PR* output, d_k. By minimizing the expectation of w_k based on the minimum mean square error (*MMSE*) and with the monic constraint, $h_0 = 1$ approach, the corresponding filter tap values could then be retrieved with the following equations (Equation 2-4, 2-5, 2-6) [30]:

$$\lambda = \frac{1}{I^T(A - M^T R^{-1} M)^{-1} I}$$

(2 - 4)

$$H = \lambda(A - M^T R^{-1} M)^{-1} I$$

(2 - 5)

$$F = R^{-1} M H$$

(2 - 6)

In the equations 2-4, 2-5, 2-6, H is the ideal *GPR* target, having the elements $[h_o\ h_1\ ..\ h_{L-1}]^T$ while F is the *PR* equalizer target, having the elements $[f_{-K}\ \dots\ f_0\ \dots\ f_K]^T$. H is a L length filter while F is a $2K+1$ length filter. λ is the Lagrange multiplier. I is an L-element column vector whose first element is 1 and the rest are 0s. A is an L by L autocorrelation matrix of the binary input sequence, a_k. M is the N by L cross-correlation matrix of the received sampled sequence, s_k and binary input sequence, a_k where N is the number of equalizer coefficients (N=2K +1). R is the N by N autocorrelation matrix of the received sampled sequence s_k.

From the literature [30], using this setup and with K=10, the *GPR* channel has been tested to perform better in terms of *SNR* as compared to *PR* system.

2.3 Noise-predictive maximum-likelihood (*NPML*) channel

The noise-predictive maximum-likelihood (*NPML*) channel is a channel that is capable of operating better than a *PRML* channel at higher linear density. One of the reasons is that for the *PRML* channel, the assumption is that the noise affecting the channel is additive white Gaussian noise (*AWGN*) like. White noise is a random signal that has a flat power spectral density across the frequency domain. It means that for every noise signal frequency band of a certain span, the power is equivalent and there is no preference for any frequency. White Gaussian noise is noise that is white but having its values changing and occurring randomly along with time like the Gaussian probability distribution. *AWGN* could thus be described as a linear addition of white Gaussian noise to the sent and received signal. The implication of the assumption of *AWGN* affecting the *PRML* implementation means that as the noise does not have any preference for any frequency and no noise correlation at different linear recording densities and that it is linearly added, the noise could be decoupled easily and signal recovered using the Viterbi detection scheme, which uses the probability branch metrics and maximum likelihood scheme.

However, this assumption of *AWGN* may not hold at higher linear recording densities. There might be circumstances where the noise might be correlated and enhancement of certain noise frequencies might occur. In addition, as the noise and signal is usually filtered by an equalizer before entering the *MLSD* detector, the equalized signal can become corrupted by correlated noise [28]. This is the rationale why research was carried out to investigate the effects of the addition of noise prediction algorithm into the detector to improve the performance of the detector. This work has in fact been recognized in 2005 by the European Eduard Rhein Foundation [31] and has been widely implemented in the hard disk industry.

NPML detectors are reduced state sequence estimation detectors offering a range of possible state complexity which is equal to 2^k, where $0 \leq k \leq L$, where L reflects the number of controlled *ISI* terms introduced by the combination of *PR* equalizer and noise predictor of length N. The additional noise prediction or whitening process is typically introduced into the branch metric calculation of the Viterbi algorithm [32, 33, 34]. Reliable operation of the prediction/whitening process is achieved by using decision from the path memory of the Viterbi detector [35, 36, 37] and can be easily implemented in which the decision feedback path can be realized by simple table look-up operations *e,g*. by means of a random-access memory (*RAM*). The contents of the table can be updated as a function of the actual channel operating point ($PW50/T_t$: where $PW50$ is the pulse width at 50% amplitude point of the channel's step response, T_t is the duration of the written bit) to maintain optimal performance within the given parameter space [34].

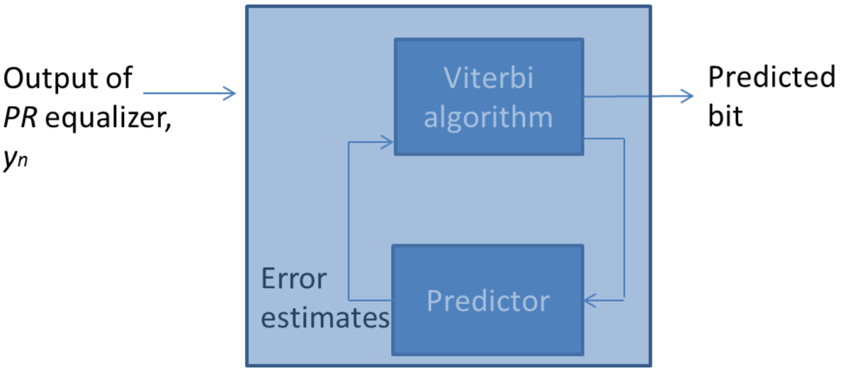

Figure 2 - 7: General *NPML* configuration

$$y_n = yPR_n + w_n$$

(2 - 7)

Figure 2-7 shows the general *NPML* configuration [34]. In equation 2-7, y_n is the output of the *PR* equalizer, yPR_n is the ideal *PR* signal, w_n is the noise that is embedded in the signal output from the equalizer, *n* refers to the particular time instant when the output is sent.

$$\widehat{w_n} = p(D) = (p_1 D^1 + \dots + p_N D^N)$$

(2 - 8)

$$e_n = w_n - \widehat{w_n} = w_n - \sum_{i=1}^{N} w_{n-1} p_i = (y_n - yPR_n) - \sum_{i=1}^{N} (y_{n-i} - yPR_{n-i})\, p_i$$

(2 - 9)

The predictor block that helps to derive the predicted noise, $\widehat{w_n}$ with a finite number of predictor taps, *N*, is added to the Viterbi branch metric calculation block. The predicted noise signal equation is as shown in equation 2-8 and the estimated error equation is also derived in equation 2-9.

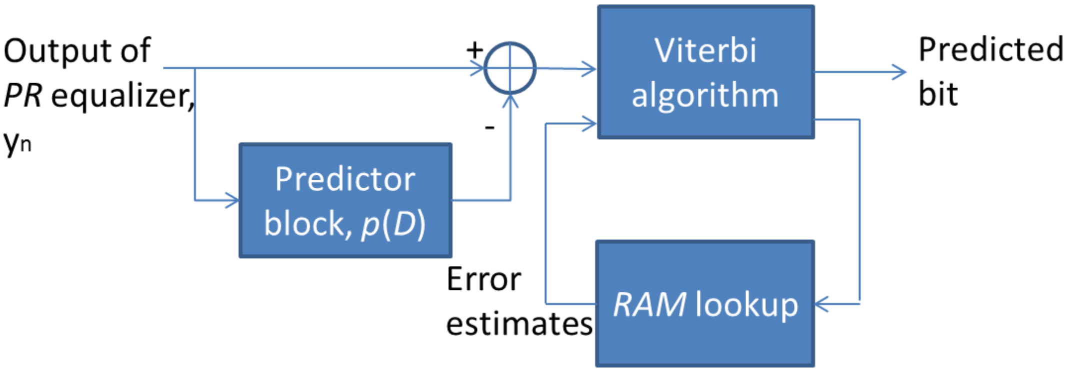

Figure 2 - 8: A typical *RAM*-based *NPML* configuration

$$\lambda_n(s_j, s_k) = \left[y_n - \sum_{i=1}^{N} p_i\big(y_{n-i} - yPR_{n-i}(s_j)\big) - yPR_n \right]^2$$

(2 - 10)

From the literature [34], the branch metric is derived to be as shown in equation 2-10. s_j refers to the *j*-th state while s_k refers to *k*-th state. This expression allows the Viterbi branch metric to include the effects from predicted errors. However, this calculation is not suitable for implementation as it requires multiplication in the embedded predictor as opposed to just additions or *RAM* lookup setup, which is illustrated in Figure 2-8 [34]. Due to the complexity of the expression described in the literature and the need to keep the topic generic instead of just investigating specific *PR* target implementations, the discussion of the *NPML* block shall end here. Interested readers could read-up further on these literatures which conducts a more thorough and specific discussion on particularly the *PR*4 target [34] as well as a generic transfer function discussion of the *NPML* scheme [38].

2.4 Pattern dependent noise predictive (*PDNP*) channel

In the previous section, the *NPML* channel was discussed. The *NPML* scheme is easily integratable to existing *PRML* scheme and is able to predict and reduce the effects from additional correlated noise that existed when the signals passed through the *PR* equalizer filtering stage. As the hard disk industries improve in recording densities, media noise became one of the prominent noise sources. Media noise arises due to the differences in the magnetic grain distribution which results in a switching field distribution in the media. This switching field distribution when coupled with the writer head field gradient will cause transition noises especially at those regions where the field is not strong enough to overcome the coercivity of the media. As linear densities increase, the control of transition noise becomes more important due to a need to write high data frequencies, meaning sharper and more accurate transitions are required. Usually such transition noises are data dependent. This is the rationale why *PDNP* channels are investigated upon due to a need to correct pattern dependent noise [39, 40]. *PDNP* has also been described to be the generalization of the *NPML* technique where pattern-dependent whitening is achieved by making use of the pattern-dependence of the first and second order noise statistics [28]. If the noise is additive Gaussian and does not depend on the input bit pattern, *PDNP* has been shown to reduce to *NPML* technique [40].

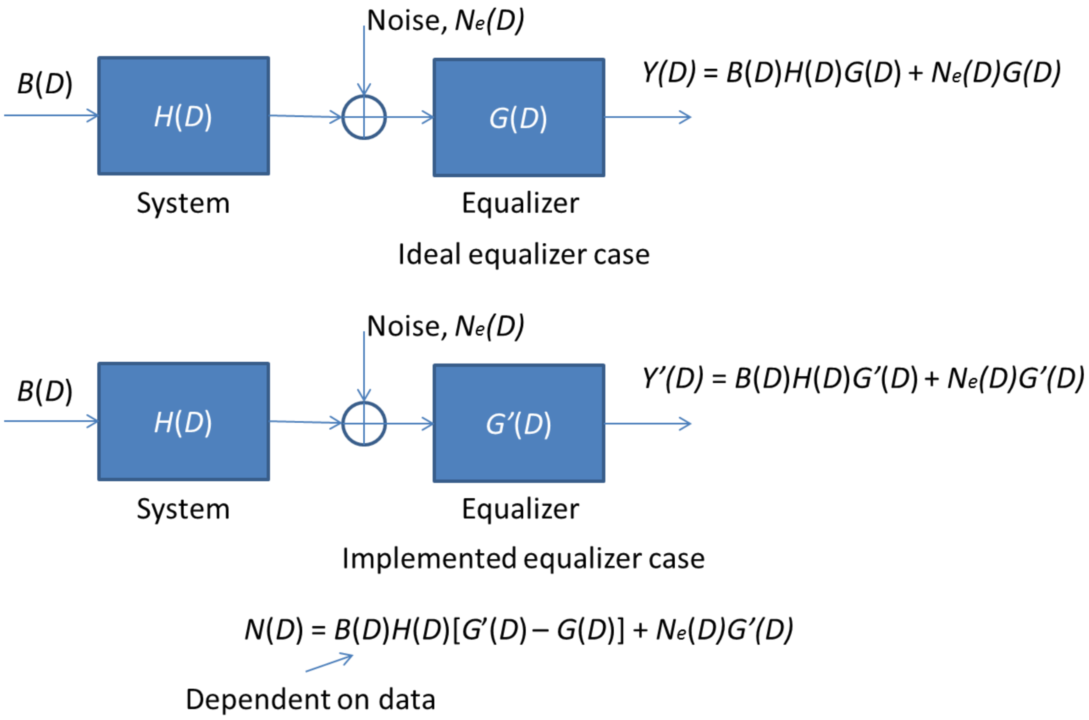

Figure 2 - 9: Illustration of the correlated-ness of the noise derived from the difference between the implemented and the ideal equalizer case

Figure 2-9 is used to illustrate more clearly the correlated-ness of the noise signal with the data signal. Let's assume a input signal polynomial, $B(D)$ and the system response, h_k are given. The system response represented by h_k, where $k = 0, 1 \ldots n$ and n equals the number of detected impulse response signals of the system. $H(D)$, which is the transfer function of the system will be represented by the following equation: $H(D) = \sum_{k=0}^{n} h_k D^k$, where D is the delay time operator. The ideal zero forcing equalizer transfer function will be given by $G(D)$ while the actual implemented equalizer transfer function is $G'(D)$. After manipulating the equations and arranging them to find the noise transfer function, *N*(*D*), it is shown that the noise is actually dependent on the data polynomial, *B*(*D*) [28].

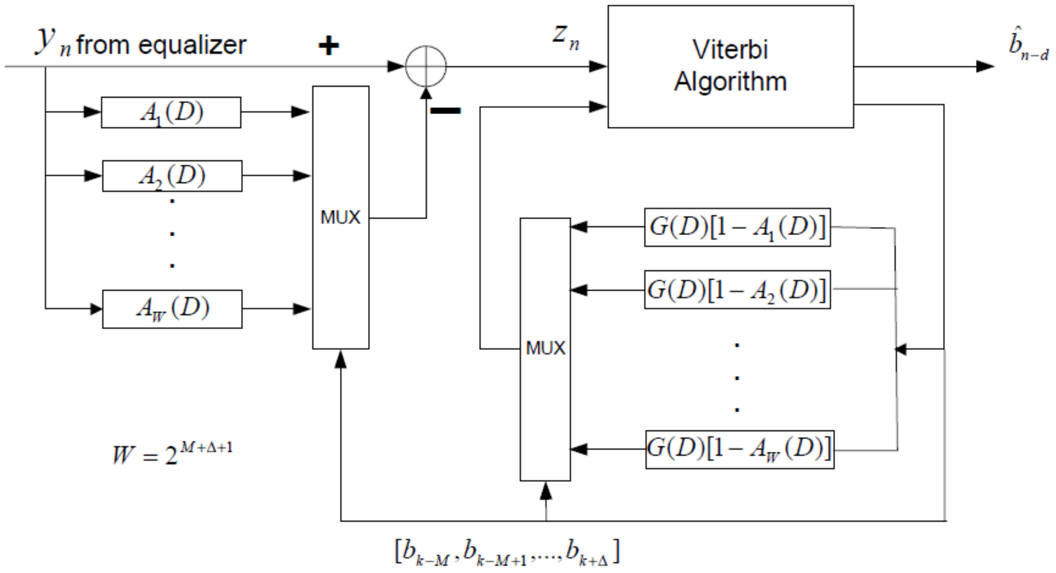

Figure 2 - 10: *PDNP* maximum likelihood detection scheme

Figure 2-10 shows a possible *PDNP* maximum likelihood scheme such that the targeted *PR* signal is $G(D)(1\text{-}A_g(D))$. Notice the similarity of the configuration between Figure 2-10 and Figure 2-8, which is the *RAM*-based implementation for *NPML* scheme. Quoted from the literature, the steps to implementing the above *PDNP* method is as follows:

1) Compute the coefficients of the noise predictors and pattern-dependent variances used that are based on the auto-regressive Gaussian process. The predictors should be computed either adaptively or at least in the least mean square (*LMS*) method or computed in the training phase
2) The Viterbi trellis has to be setup such that one is able to determine the signal as well as the predicted noise sample from the transition information

3) For each transition or branch, the branch metric is computed with the predicted noise effect and each possible transition probabilities inside.
4) Proceed as normal Viterbi detection

Due to the complexity of the *PDNP* scheme, it will take quite some time to be able to cover this topic well. Therefore, the scope of this section here is to provide readers a brief understanding of why the need to use *PDNP* and a general idea of how to implement the *PDNP*. Further information could be acquired here [28].

2.5 *BCJR* algorithm

In the following paragraphs, the *BCJR* algorithm is compared against the Viterbi algorithm that is commonly used in the conventional detector. The Viterbi algorithm is a *ML* algorithm such that it minimizes the error probability between the transmitted and received code-words via probability branch metrics and cost values. It is commonly used for decoding convolutional codes. The algorithm works on states which is a sequence of bits and the detector itself if based on Viterbi algorithm has to have prior knowledge of the possible input states, possible transitions to next states and the output result of such transitions. In short, it is an algorithm that reduces the word error rate. Therefore, if the algorithm is applied to systems that do not have equivalent occurrence probabilities for different possible input bits, it might not be able to perform well due to its lack of decoding and correcting bit errors.

BCJR is a short acronym that represents Bahl-Cocke-Jelinek-Raviv, the four inventors that came up with this decoding scheme. *BCJR* algorithm is a maximum a posteriori (*MAP*) algorithm [41]. The difference between *MAP* and *ML* algorithms is that *ML* assumes the uniform prior, while *MAP* does not always assume so. Instead, *MAP* algorithms make use of the prior probability distribution to calculate a result that has the highest possibility of occurrence [42, 43, 44]. *BCJR* works by looking at the individual message bits and reduces the bit error rates via multiple recursions and storage of temporarily processed data as it traverse across the possible trellis paths of the input bits. There are four basic steps involved in the algorithm:

a) Calculation of the forward probabilities of reaching current state of bits with previous received bits,

b) Calculation of the backward probabilities from the next state of received bits to the possible current state of bits,

c) Calculation of the probability of receiving next state of output bits given next state is known,

d) Calculation of the a posteriori *L*-values using the collated probabilities which would determine the decoder output based on the polarity or confidence magnitude of the *L* values.

The number of computation steps as observed in the *BCJR* algorithm is high. At the expense of having the capability to correct bit errors, the decoding of the data bits received via *BCJR* tends to be more exhaustive and computational and time intensive.

In the case of magnetic recording system which is a binary system, *BCJR* is therefore preferred when the probabilities of the occurrence of the input bits is skewed, that there is a particular preference for the occurrence of maybe 1s or 0s due to the nature of the system or channel. Also in situations where reliability is of importance and time of computation is not a priority, *BCJR* would be a fantastic algorithm to use.

Otherwise, in situations where the binary input bits (+1, -1) are more or less of equivalent occurrence (0.5, 0.5), the Viterbi algorithm has been shown to perform as well or if not even better in terms of the overall performance in terms of computation and accuracy required by the channel [45].

2.6 *LDPC* (low density parity check) code

LDPC is a short form that means low density parity check. It was invented by Robert Gallager [46] in his 1963 MIT Ph. D dissertation but was not commonly used then due to its complex computation and the existence of Reed Solomon (*RS*) code [47] which was well suited for its error correction capabilities with minimum complexity.

RS code is a type of *BCH* (Bose – Chaudhuri - Hocquenghem) code, which means it is a polynomial code that has cyclic error correction capability and could be decoded via syndrome decoding [48, 49]. *RS* codes can be represented by (n, k), where n is the encoded bits with the parity bits added and k is the message bits. The *RS* decoder can correct up to t error bits. t is related by the equation 2-11. Due to the scope of this thesis, *RS* code shall not be elaborated further but interested readers could still use the reference links provided above to have better understanding of the nature and error correction capabilities of the *RS* code.

$$2t = (n\text{-}k) \tag{2 - 11}$$

A *LDPC* magnetic recording channel is a channel that uses *LDPC* codes for error correction as compared to conventional magnetic recording channels that uses *RS* codes. In many literatures, *LDPC* has been known to perform better than *RS* codes in terms of the decoding performance at high bit error rates. [50, 51]. This is the rationale of doing a review of the *LDPC* code based channel, which more shall be elaborated about its properties and characteristics. One thing to note, data storage industry has moved towards 4 *k*-byte (32 *k*-bit) sectors instead of the conventional 512 byte (4 *k*-bit) sectors [52]. One of the reasons is to take advantage of the powerful and longer error correcting codes like the *LDPC* code as well as to take advantage of the more powerful processors available for their speed of calculations.

2.6.1 Representation of code

In many literatures, these *LDPC* codes, c are usually represented by variables n and k, in the format (n, k), where n represent the number of nodes or the number of bits in the transmitted code-word, k represent the number of message bits and (n-k) represent the number of constraint nodes [53]. In Figure 2-11, the *LDPC* code configuration is represented by a bipartite graph, also known as Tanner graph. n has the value 4 while k has the value 1. Each of the 4 nodes represented by n(1-4), is linked accordingly to the constraint nodes, cn(1-3) represented by the adder with modulo-2 constraint. The modulo-2 operation is also known as *GF*(2), where addition and subtraction are both *XOR*, and multiplication is *AND* operation. The modulo-2 constraint is such that there can only be even number of inputs having the value of 1. There are in total (n-k) constraint nodes which is equivalent to 3 as illustrated in Figure 2-11 where k=1. Possible code-word combinations, c for this n = 4 bit setup can be of the following: {0000, 1001}. Only these two code-word combinations will fit the modulo-2 constraint connecting between the nodes.

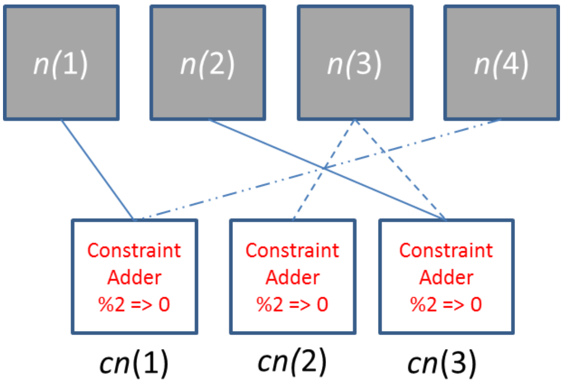

Figure 2 - 11: *LDPC* code representation (*n*, *k*) where *n*=4 and *k*=1

In a typical operation, these nodes, *n*(1-4) will receive a 4 bit code-word that should satisfy the *LDPC* code representation illustrated in Figure 2-11. In order to test whether the above representation holds, the parity check matrix, H as defined in equation 2-12 is required. For each element in the H matrix, the element $(cn(i), n(j))$ will have a value of 1 if there is a connection, else 0 if no connection. This parity matrix could then be used to verify if the received code-word satisfy the constraints using the relationship described in equation 2-13. As described earlier, the matrix multiplication is an *AND* operation while the addition is *XOR* operation.

$$H = \begin{bmatrix} (cn(1), n(1)) & \cdots & (cn(1), n(j)) \\ \vdots & \ddots & \vdots \\ (cn(i), n(1)) & \cdots & (cn(i), n(j)) \end{bmatrix} = \begin{bmatrix} 1001 \\ 0010 \\ 0110 \end{bmatrix}$$

, where in this case, *i*=3, *j*=4

(2 - 12)

$$H * c^T = 0$$

(2 - 13)

2.6.2 Properties of the *LDPC* code

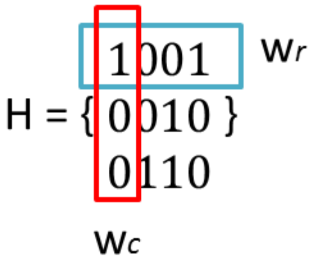

Figure 2 - 12: Illustration of two property variables, w_c and w_r, of parity matrix

There are two types of *LDPC* codes. *LDPC* codes can be regular or irregular [54]. For the code to be regular, it has to satisfy three conditions.

Condition 1:

The number of 1s, $\mathbf{w_c}$, in each column is the same

Condition 2:

The number of 1s, $\mathbf{w_r}$, in each row is the same

Condition 3:

$w_c = w_r$.

H, in this case, is an irregular *LDPC* parity check matrix as $w_{c=1} \neq w_{c=3}$, and $w_{r=1} \neq w_{r=2}$ and $w_c \neq w_r$. The two property variables, w_c and w_r are illustrated in Figure 2-12

Also, for the code to be considered as low density, 2 conditions: $w_c <<$ (no of nodes, *n*) and $w_r <<$ (no of constraint nodes, *cn*); must be met.

2.6.3 Construction of the code-word from the message bit(s)

As described above, the example given has k=1 and n=4. This means that this *LDPC* message is actually a 1 bit message encoded as a 4 bits one. This additional redundancy bits introduced helps the error correcting capability at the decoding process. In this section, a brief description will be given on how to produce the transmitted code-words from the message bits and the parity matrix. Equation 2-14 describes relationship between the message bits, m and a generator matrix, G.

$$c = m * G$$

(2 - 14)

The derivation process of the generator matrix is more complicated and requires row reduction operations also known as the Gaussian elimination process. Basically, the parity matrix, H has to be reduced to the form ***(a)*** described in Figure 2-13. The identity matrix $I_{(n-k)\ by\ (n-k)}$ in this example will be of the size 3 by 3. The derived Q is then $(0\ 0\ 1)^T$. As the parity matrix is made up of binary bits, the matrix P which is required to derive G is simply the transpose of Q. $P = (0\ 0\ 1)$. As $k = 1$, the final derived generator matrix, $G = (1\ 0\ 0\ 1)$. Using this derived G, equation 2-14 and message bits {0, 1}, the same two code-words {(0 0 0 0), (1 0 0 1)} which satisfies the parity matrix, H and the required *LDPC* configuration in Figure 2-11 can be derived.

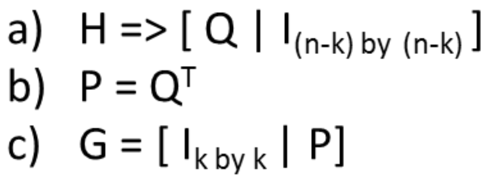

a) $H \Rightarrow [\ Q\ |\ I_{(n\text{-}k)\ by\ (n\text{-}k)}\ ]$

b) $P = Q^T$

c) $G = [\ I_{k\ by\ k}\ |\ P]$

Figure 2 - 13: Derivation steps for the generator matrix, *G* from the parity matrix, *H*

2.6.4 Decoding scheme

Decoding of the *LDPC* channel is a *NP*-complete problem. The abbreviation *NP* [55] here means nondeterministic polynomial time, which essentially means the solution is easy to verify but there is no known efficient short way to quickly locate the solution.

NP-complete problems are often addressed by using approximation algorithms. Iterative belief propagation is one of the common methods that are used here on this binary channel [53]. Basically, multiple iterations, i are required to ensure the received code-word is the correct one, and a maximum iterative constant, $i_{terminate}$ is required to decide an erroneous un-correctable code-word received.

The decoding scheme [54] in brief is as follows:

a) All message nodes send their message bit, together with the attached probabilities for it being 1s or 0s, to their corresponding connected constraint nodes.

b) For each message node message bit that the constraint node received, the constraint node then calculates the probability that there is an even number of 1s among the other message nodes. The constraint node then sends this probability back to the message node that sends the bit.

c) The message nodes receive the probabilities from their corresponding constraint nodes, and then update their response message back to the constraint node and also update their current holding message bit value.

d) Verify with the parity matrix. If the verification is successful, the loop terminates and the code-word is recorded down as a received code-word. If the verification is not successful, the next iteration starts and the message nodes will be updated with the value that matches the accumulated probability cost. This method of decoding is in fact very similar to the *BCJR* algorithm.

Note that due to the scope of this section which is to introduce *LDPC* and provide a basic understanding, the discussion of the decoding section shall end here. The study of the different methods of decoding *LDPC* and implementing of the *LDPC* in the hardware stage could be further touched on in another study as the area can be quite extensive and intensive. There are in fact many literatures available that provide a more comprehensive and in depth discussion [56, 57].

2.6.5 Block error rates (*BLER*)

In *LDPC* channels, because of the format of the codes, the bit error rates do not contain enough intuitive info to classify them. Instead, block error rates, *BLER* are usually used. *BLER* is defined as the event such that there is at least 1 bit error in the *k* bits message code block.

2.7 Conclusions

The purpose of covering so many generic channels and algorithms essentially is to have a sense of the possible available channels that could be applied for shingled writing.

Up till now, standard *PRML* channel, which is a *ML* based channel based on *PR* signaling with the assumption of *AWGN* affecting the system, has been covered. *NPML* channels further improves the *PRML* channels such that they account for the observation that noise entering the detector might not be *AWGN* and could even be correlated, thus the need to whiten the noise and to do noise prediction by integrating the noise prediction scheme directly into the Viterbi metric during the branch metric calculation stage. As the demands of channels increases with increasing pressure to work at high linear densities, with the observation that media dominant transition noise entering the detector could also be data-dependent, *PDNP* channels which serve to reduce the data dependent noise, then come into action and could be shown to be a generalization of the *NPML* technique.

The *BCJR MAP*-based algorithm was then covered next as the assumption of uniform prior in the *ML* might not be true in all cases of the emission or transmission of the data. This is especially so when due to environment and inherent setup or configuration issues, there is a preference for certain orientation of data bits or sequence of data bits to be present. In such cases, *ML* sequence detectors will not be able to perform as well as *MAP* detectors like the *BCJR*. However, it was also mentioned that *BCJR* detectors are time and computational intensive due to the need to traverse across the trellis matrix both forward and backward multiple iterations before the bit sequences could be outputted. Depending on the circumstances and usage, Viterbi detectors are still viable detectors in terms of the accuracy and detection time required.

LDPC codes was the last topic to be covered in this chapter but it is one of the most significant and important ones to be covered. A brief background on its competitor, *RS* code, was touched on before more was elaborated on the *LDPC* codes, the structure, properties and its construction and it been able to perform better than conventional *RS* codes at high recording densities. A brief description of the decoding scheme was given where the generator matrix and parity matrix as well as the node and constraint probabilities play a role in determining the code-word.

After looking at the possible channel implementations and modifications, some conclusions could be derived. For code based implementations, the *LDPC* would be much preferred against the *RS* code especially at higher recording densities. The *PDNP* modification would help to reduce data correlated noise effects. As for the detector, depending on the computational and accuracy requirements, Viterbi or *BCJR* detectors are both possible contenders.

With this background knowledge of the read channels, we will proceed to the subsequent chapters where the possible sources of media noise and the corresponding root causes are studied in detail. Then, the shingled magnetic recording system and its areal density gain against the conventional magnetic recording system are investigated upon.

Chapter 3: Writing process induced media noise measurement and transition jitter probability measurement

3.1 Introduction

This chapter is a description of the experiments and analysis done from the combination of two published papers: 1) writing process induced media noise measurement using 3*D* footprint and corresponding noise profile [58] and 2) probabilities of transition jitter at different off-track positions [59].

Reducing grain number per bit is still the current major way to push up the areal density of conventional perpendicular recording before the industry shifts to the more advanced recording technologies, such as energy assisted magnetic recording or bit patterned media [60]. Current typical commercial perpendicular media has grain size of around 8 *nm*, and this size has remained more or less the same since its introduction [61]. Assuming current granular media of 540 Gb/in^2 areal density and a bit-aspect ratio (*BAR*) of 6, typical bit lengths for the media can go as low as 15-20 *nm* [62].

Some of the critical factors affecting the performance of the writing process are the gradient of writing field and the switching field distribution of the recording medium. The written transition curvature of a given head onto the media induces increased transition jitter noise and degraded *SNR* or *BER* performance [63, 64, 65]. Writing processes can thus cause extra medium noise. As medium transition noise is the dominant noise in the perpendicular recording system, measuring and understanding the head writer footprint and its corresponding noise profiles in recording medium is thus important and useful to determine the optimized writing condition for a given head-media combination.

In the 1st part of this chapter, this work will describe about the methodology of using averaging methods to measure the writer footprints and its noise profiles, which are recorded at different writing currents on a Spin-stand. It can show the transition curvature and noise profiles characteristics of the given head-media combination clearly at different writing conditions.

In recording systems, noises like media, head and electronics noise are usually present. Transition jitter, which is one type of media noise, tends to occur at regions where magnetic transitions could be found. Such noise could affect the storage and readability of the data, especially as more accuracy is demanded when hard disk industries push for higher and higher densities. It is therefore important to be able to measure and have an innate understanding of the transition jitter affecting a particular head-media recording system so as to design better heads or media or even better encoder/decoder schemes to address such issues. In some publications, the transition jitter has been measured [66] and correlated to magnetic cluster size distributions based on Karhunen-Loeve expansion [67, 68].

In the 2nd part of this chapter, this work will focus also on describing the methodology of using averaging methods to measure the writer footprints [69] and the transition jitter profiles, which are recorded at different writing currents on a Spin-stand. It shows the transition jitter profiles characteristics of the given head-media combination at different writing conditions.

3.2 Experimental setup

A static read/write tester [70, 71] or a Spin-stand [72] can be used to measure writer pole footprint in the recording medium. In the experiments, the writer footprints were retrieved from a Spin-stand and the testing procedure in ref [72] was followed. The experiments were carried out on Guzik Spin-stand DTR 3000 system.

Two different commercial heads have been used for the evaluation. The *SEM* images of the two writer poles are as shown in Figures 3-1 and 3-2, which shall be labeled as writer A and B respectively. Writer A's trapezoid pole has the widths of 135 *nm* at trailing edge and 31 *nm* at leading edge. The magnetic write width (*MWW*) of this writer A is 100 *nm*. Writer B's pole has the widths of 70 *nm* at trailing edge and 35 *nm* at leading edge. The *MWW* of this writer B is 60 *nm*. The test was performed on a 2.5 *inch* commercial disc at the middle diameter (*MD*) location, rotating at 5400 *rpm* spindle speed, and at 0 skew angle.

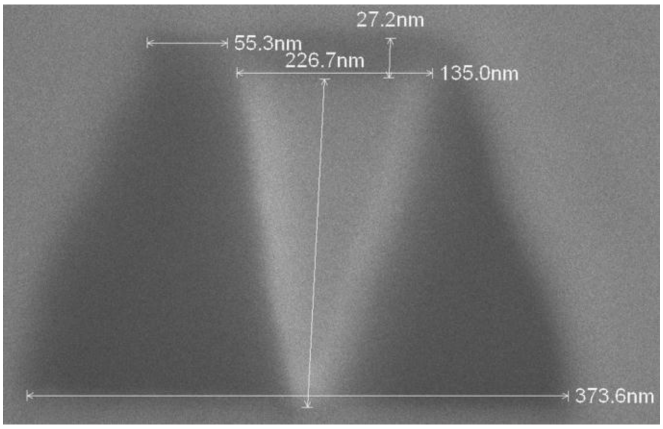

Figure 3 - 1: This *SEM* image of writer A's pole area shows the writer geometry at air-bearing surface

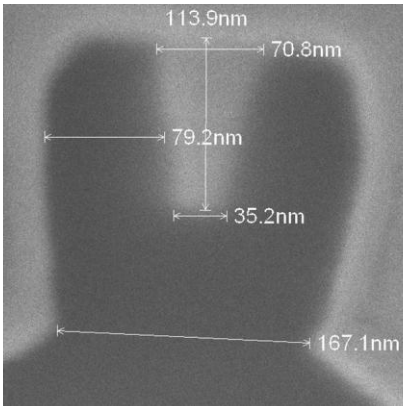

Figure 3 - 2: This *SEM* image of writer B’s pole area shows the writer geometry at air-bearing surface

The center track is initially *DC* erased over the band *AC* erasure background as illustrated in Figure 3-3. Using write gate control, a low frequency pattern used for alignment purposes is recorded at the front of the data sector. Without overwriting this alignment pattern, the data pattern which consists of a low frequency section and a high frequency section is then chosen and written repetitively using a magnetic head onto a magnetic medium [73]. With adjustment of the amplitude and rise time of the overshoot current and the written frequency, the magnetic head footprint is imprinted at a relatively good resolution during the low frequency data sequence with minimal or zero transitions recorded during the high frequency data sequence onto the media.

The data pattern used to generate the footprint is 120 bits long. The generic data pattern written using Guzik pattern designer is as follows:

```
patdef MyPattern
pattern = (“1”+ “0”*x+“1”*(120-(x+1)))*inf
patend
```

The variable *x* used in the pattern is changeable but in the experiment, *x*=7 has been used to do the analysis. What this pattern represents is what was described about at the experimental setup section, where each "1" represents a transition and each "0" represents no transition. If *x*=7, the Guzik spin-stand will interpret the writing to be an initial transition and then to hold the magnetization for 7 bits count. This section is the low frequency data. Then it will start to write the remaining 120-8=112 continuous bit transition sequence. This section is the high frequency data. This low and high frequency data pattern is then repeated infinitely which the symbol *inf* represents. As the written frequency is at 3000 *Mbits*/s, one can derive the estimated physical length of the low frequency region written on the disc, which is of the range 33 *nm*. The experiment is repeated for 9, 11, 13 bits of "0" case, which corresponds to a low frequency range of 41, 50, 58 *nm* case. As the number of bits written repetitively is 120 bits, each set of footprint data has a span of 500 *nm*.

In order to construct the footprint image, the reader is scanned at 5 *nm* fine step size along the cross track direction. Cross-correlation of the alignment pattern allows the final footprint data to be aligned correctly to reproduce the writer footprint profile. Guzik spin-stand's control software has a 3*D* pulse profile module that is able to facilitate this process and thus allows easier retrieval of well-aligned 3*D* footprint data.

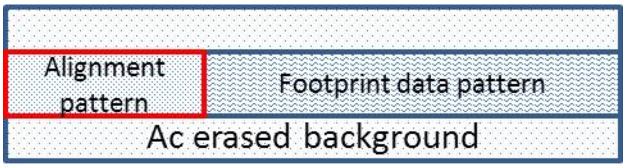

Figure 3 - 3: The footprint data pattern and alignment pattern is recorded onto a *DC* erased track with a band *AC* erased background

In order to remove the random electronic and reader noises, multiple revolutions averaging of read-back signals are conducted for the footprint capturing. Each writer footprint in recording medium reflects the characteristics of writing field profile and medium magnetics of grains.

3.3 Writing process induced media noise measurement using 3*D* footprint and corresponding noise profile

Before averaging can be done, each individual footprint data have to be extracted out from the read-back signals. To do so, a set of conditions are used to determine whether or not to retrieve the footprint data from the read-back signals.

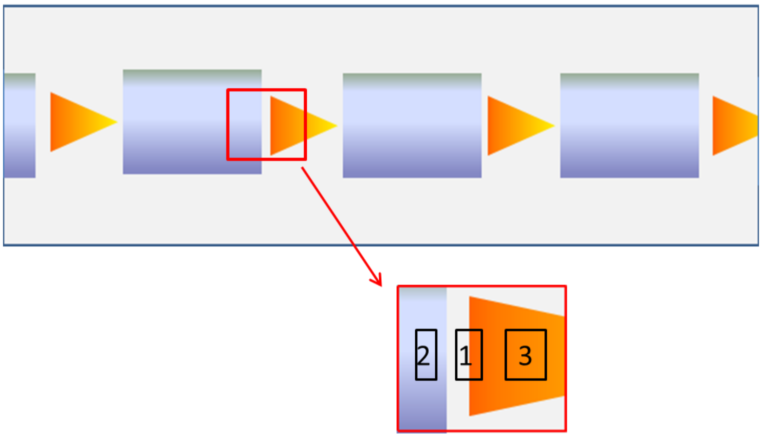

Figure 3 - 4: Illustration of the 3 conditions to determine the retrieval of the footprint from the read-back signals

Depending on the writing and media conditions, sometimes the writer footprint might not be written well on the media. If these kinds of poorly written footprints are used for the averaging, it will greatly skew the results of the analysis. Therefore, it is essential to ensure that footprints of significant quality are retrieved. This is done by looking at 3 basic conditions. Footprint data is essentially intensity valued read-back signal data. With that in mind, the following conditions are used:

1st condition: To look at the regions where the values transit from negative to positive. Due to the existence of noise, in order to achieve more accurate results and to prevent false detection, area averaging is used first on the data near the track center region as illustrated in Figure 3-4. When this condition is met, the 2nd and 3rd condition will be looked into.

2nd condition: To look at region 2 and apply area averaging in this region. This region has to be of a negative cost value. This is to ensure that this is not a false footprint due to the influences of noise.

3rd condition: To look at region 3 and apply area averaging in this region. This is where the footprint is located, therefore high positive values should be expected.

Using these 3 conditions and by repeating the detection process at a controlled multiple of the written data pattern length along the down track, the detection would be able to retrieve back the required number of footprint data for averaging.

By enough averaging of the footprints along down track direction, both the medium noise and writing field fluctuation can be removed as well. This averaged footprint represents the noise free writing profile in recording medium. The statistical characteristics of noise can be derived from the individual noise footprint which shows the media noise characteristics induced by writing process. Figure 3-5 shows footprint of this averaged writer profile of writer A which is written at 55 *mA*. The difference between individual footprint and the averaged footprint is the noise of that written footprint. In the later pages, Figures 3-12 (a) and 3-12 (b) show 2 different view orientations of the noise profile for the footprint which is written at 55 *mA*.

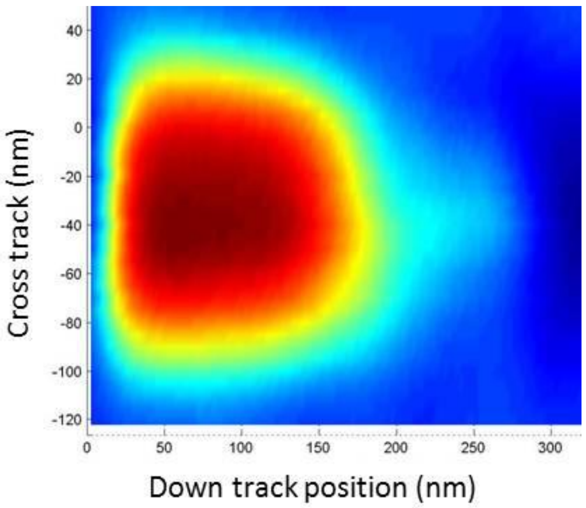

Figure 3 - 5: Averaged writer profile of writer A at 55 *mA* after revolution and down track footprint averaging

The below comparisons in Figures 3- 6 and 3-7 show the differences in the footprints retrieved for different lengths of low frequency data at the 50 *mA* case. The trailing edge which is around the down track position of 0 *nm* is the area of focus for this analysis part. There should not be much differences expected as this region is fixed to have only 1 transition. As the region of low frequency data increases, the trailing edge will be able to erase more of the magnetization effects from the leading edge thus resulting in a more blockish and thicker imprint on the media.

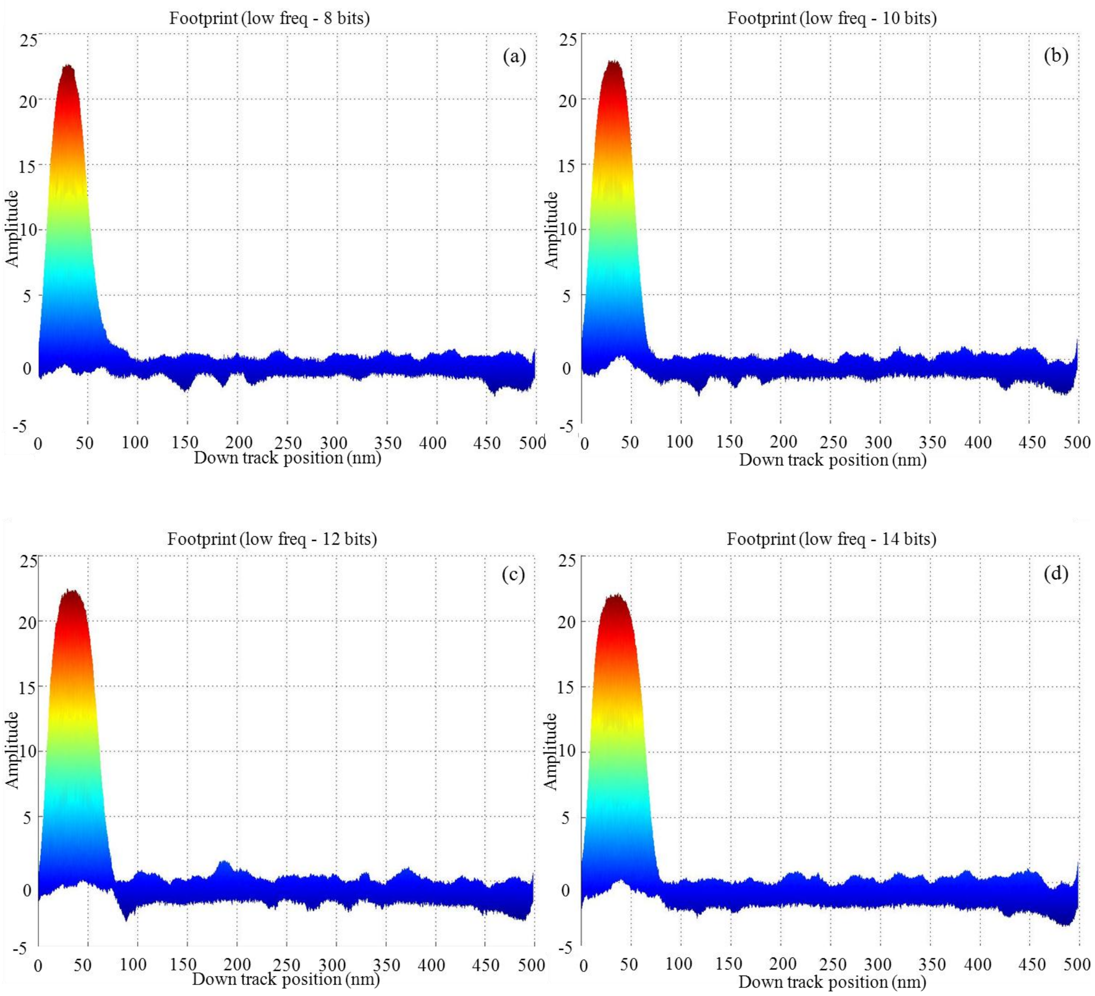

Figure 3 - 6 (a): Down - track view of 50 *mA* footprint with 8 bits low frequency region

Figure 3 - 6 (b): Down - track view of 50 *mA* footprint with 10 bits low frequency region

Figure 3 - 6 (c): Down - track view of 50 *mA* footprint with 12 bits low frequency region

Figure 3 - 6 (d): Down - track view of 50 *mA* footprint with 14 bits low frequency region

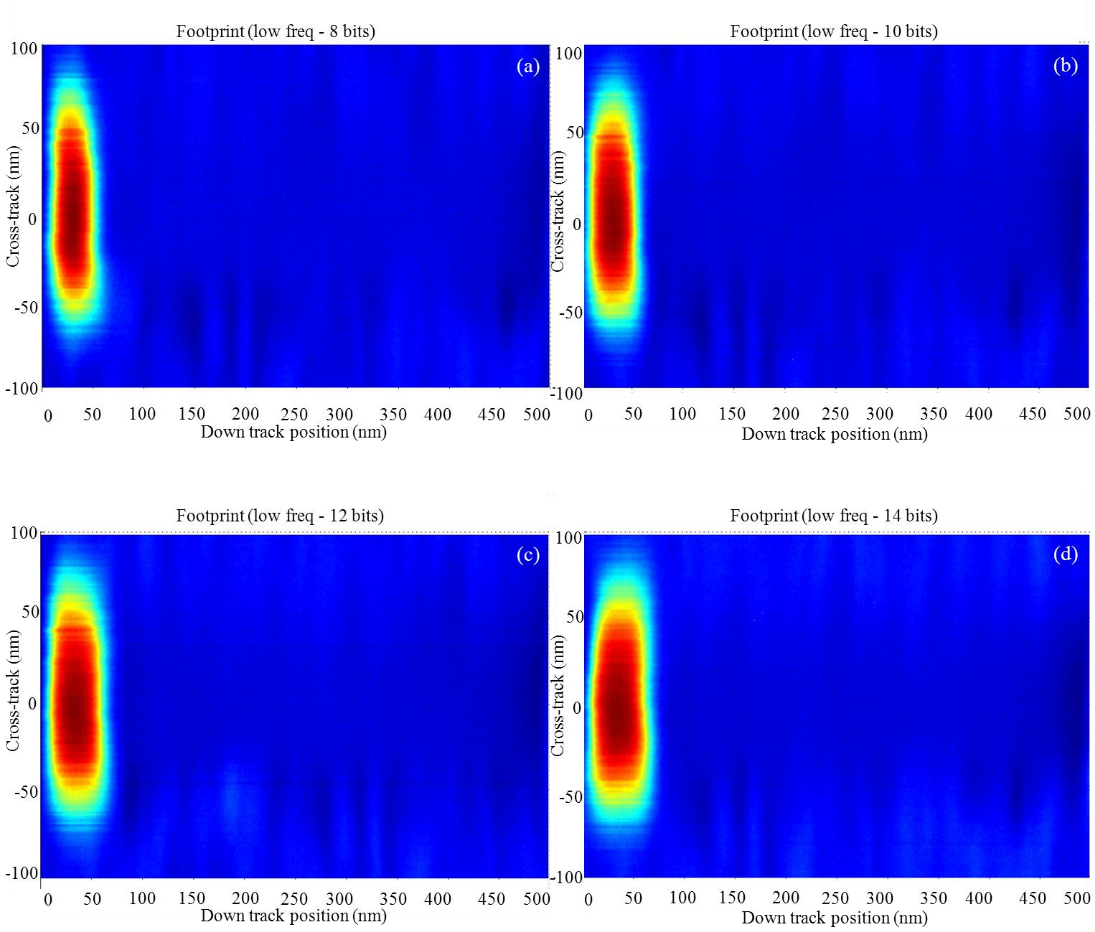

Figure 3 - 7 (a): Top surface view of 50 *mA* footprint with 8 bits low frequency region
Figure 3 - 7 (b): Top surface view of 50 *mA* footprint with 10 bits low frequency region
Figure 3 - 7 (c): Top surface view of 50 *mA* footprint with 12 bits low frequency region
Figure 3 - 7 (d): Top surface view of 50 *mA* footprint with 14 bits low frequency region

Using the same set of data, the gradient along the down track direction is plotted as shown in Figure 3-8. In these plots, the differences in the resulting gradient plot at the trailing edge are the regions of focus. The high intensity regions represented by the orange to red colors represent the higher gradient values. Taking into the effects of random errors under similar experimental conditions, except for the 14 bits case, the other cases appear to have similar profiles. For the 14 bits case, it is observed that from the footprint retrieved above and the gradient profile below, it has a more curved transition curvature, which would mean more transition errors across the cross track if data is written using that head profile.

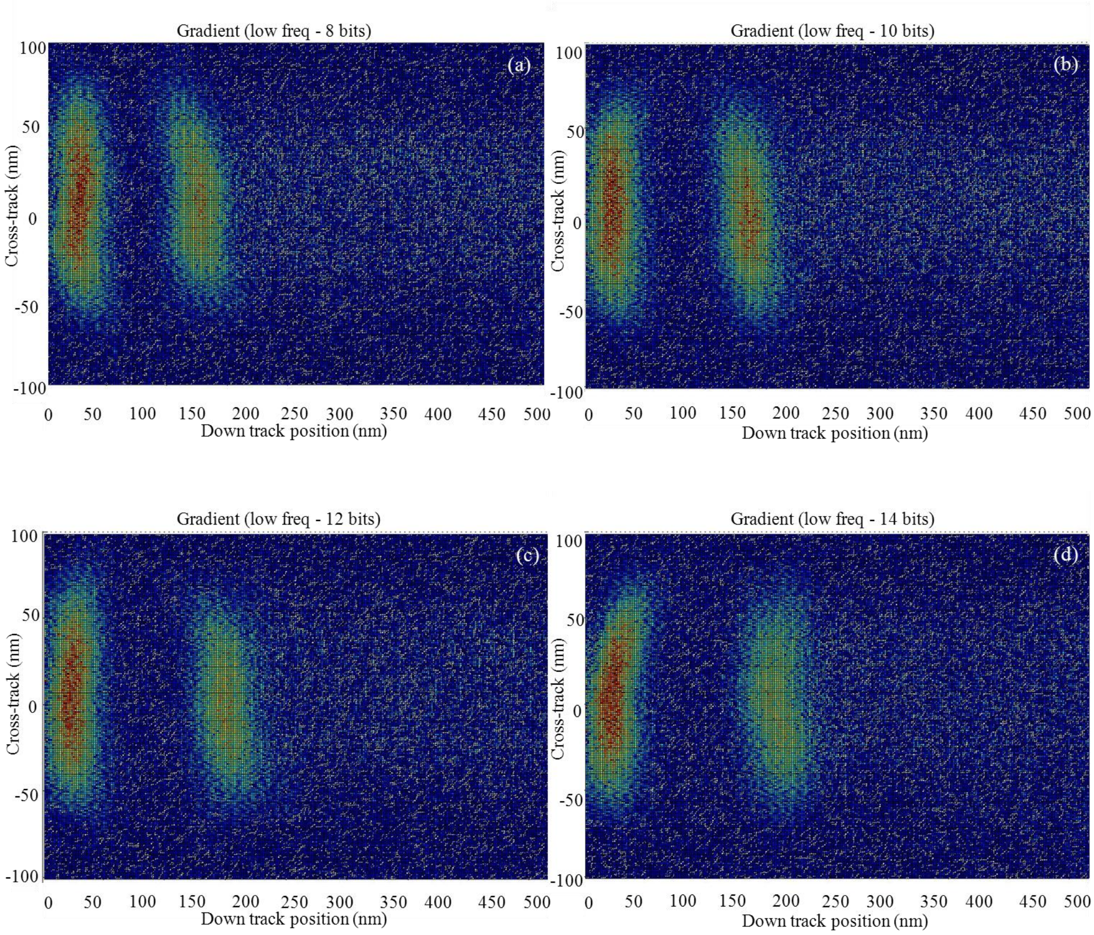

Figure 3 - 8 (a): Top surface view of 50 *mA* footprint gradient with 8 bits low frequency region

Figure 3 - 8 (b): Top surface view of 50 *mA* footprint gradient with 10 bits low frequency region

Figure 3 - 8 (c): Top surface view of 50 *mA* footprint gradient with 12 bits low frequency region

Figure 3 - 8 (d): Top surface view of 50 *mA* footprint gradient with 14 bits low frequency region

For the next analysis, the 8 bits case for different write currents shall be looked into. Figures 3-9, 3-10, 3-11 show the different plots for different writing conditions from 20 to 60 *mA*. At the trailing edge region, the transition curvature appears to decrease until it reaches a relatively optimal blockish shape at the 50 - 55 *mA* case. As for the 60 *mA* case, even though the curvature is not seen, the footprint profile appears to look tilted at an angle especially at the positive offset side. The rationale as to why this occurs could probably be contributed by both the high writing current and the experimental errors. At high writing current, the head is able to easier magnetize the media and cause unnecessary transitions and jitters when there is a minute change of the writing condition in the media or environment.

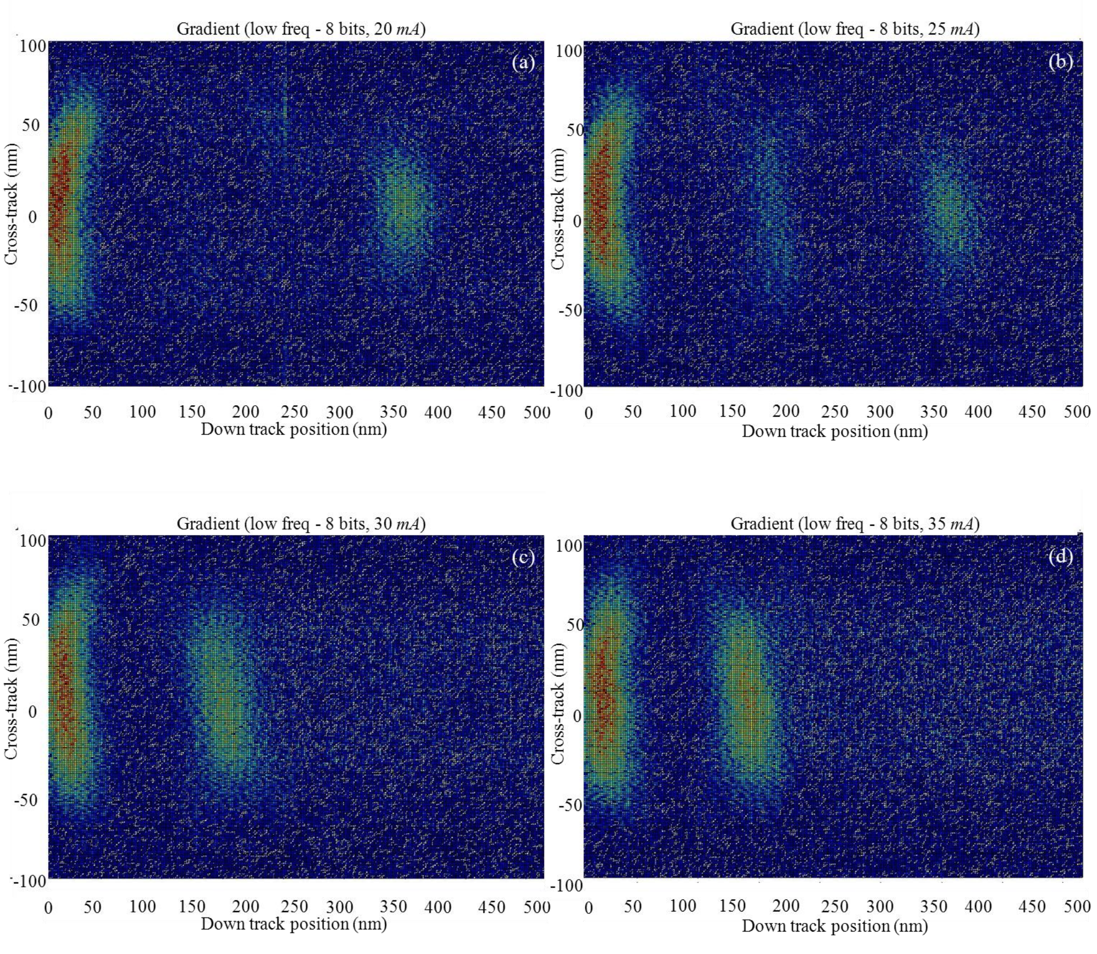

Figure 3 - 9 (a): Top surface view of 20 *mA* footprint gradient with 8 bits low frequency region

Figure 3 - 9 (b): Top surface view of 25 *mA* footprint gradient with 8 bits low frequency region

Figure 3 - 9 (c): Top surface view of 30 *mA* footprint gradient with 8 bits low frequency region

Figure 3 - 9 (d): Top surface view of 35 *mA* footprint gradient with 8 bits low frequency region

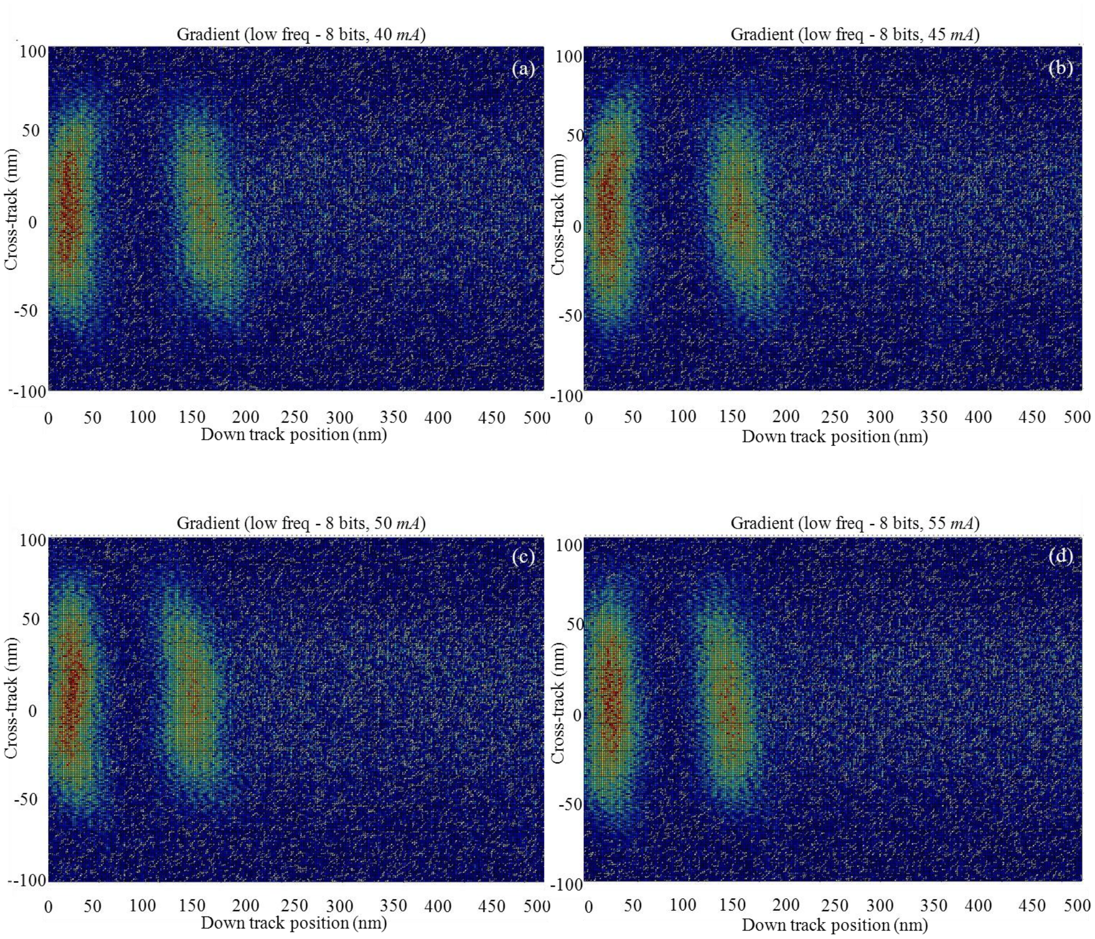

Figure 3 - 10 (a): Top surface view of 40 *mA* footprint gradient with 8 bits low frequency region

Figure 3 - 10 (b): Top surface view of 45 *mA* footprint gradient with 8 bits low frequency region

Figure 3 - 10 (c): Top surface view of 50 *mA* footprint gradient with 8 bits low frequency region

Figure 3 - 10 (d): Top surface view of 55 *mA* footprint gradient with 8 bits low frequency region

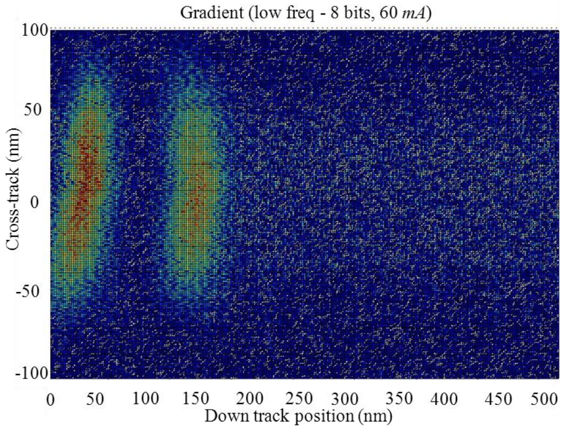

Figure 3 - 11: Top surface view of 60 *mA* footprint gradient with 8 bits low frequency region

Further analysis shall be looked into in the following section where the noise profiles together with the writer footprint would be used to determine the optimal writing condition.

3.3.1 Analysis of writer footprint and noise profiles

Writer A’s footprint and noise profiles shall be analyzed first. In particular, the 55 *mA* and the 45 *mA* case have been chosen for the analysis.

For the setup, using 55 *mA* writing current, a consistent peaking of noise was observed around the -80 *nm* region, *a*, from the trailing edge of the writer A transition in Figures 3-12 (a) and (b) From the noise profile, it can be inferred that this noise contribution comes mainly from the negative offset (*NO*) footprint regions from the footprint track center. It could thus be inferred that the noise is introduced due to the observed fluctuation of the writer transition curvature and track edge effects there (Figure 3-5).

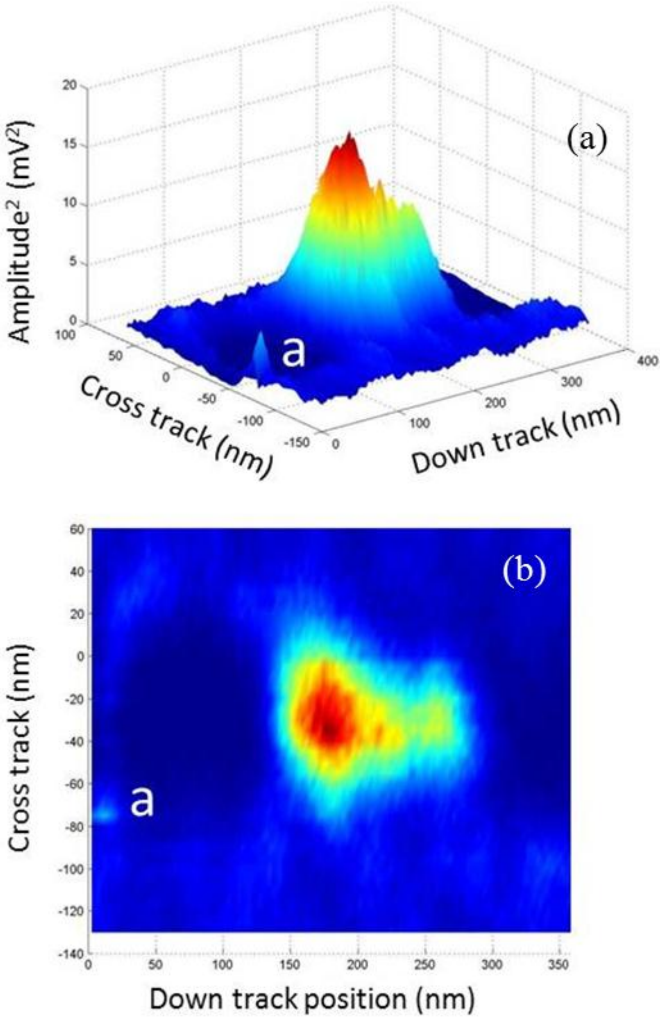

Figure 3 - 12 (a): 3*D* view of writer A's cross track against down track noise profile at 55 *mA*

Figure 3 - 12 (b): Top view of writer A's cross track against down track noise profile at 55 *mA*

At different writing currents, there were observed differences in the behavior of the footprint and noise profiles in the cross track and down track location, brought about by the changes in the strength of magnetic field at different axes induced by the head due to the change in the writing currents.

In the 55 *mA* case, the *NO* regions, *a*, was observed to contribute more noise as compared to the positive offset (*PO*) footprint regions. In the 45 *mA* case, however, the *PO* regions, *b* contributed more noise compared to the *NO* regions, *c*. From

Figures 3-13 (a) and (b), more noise is observed to be distributed nearer to the footprint track center. This centering of the noise profile nearer the footprint track center has the potential to generate more jitter noise at track center.

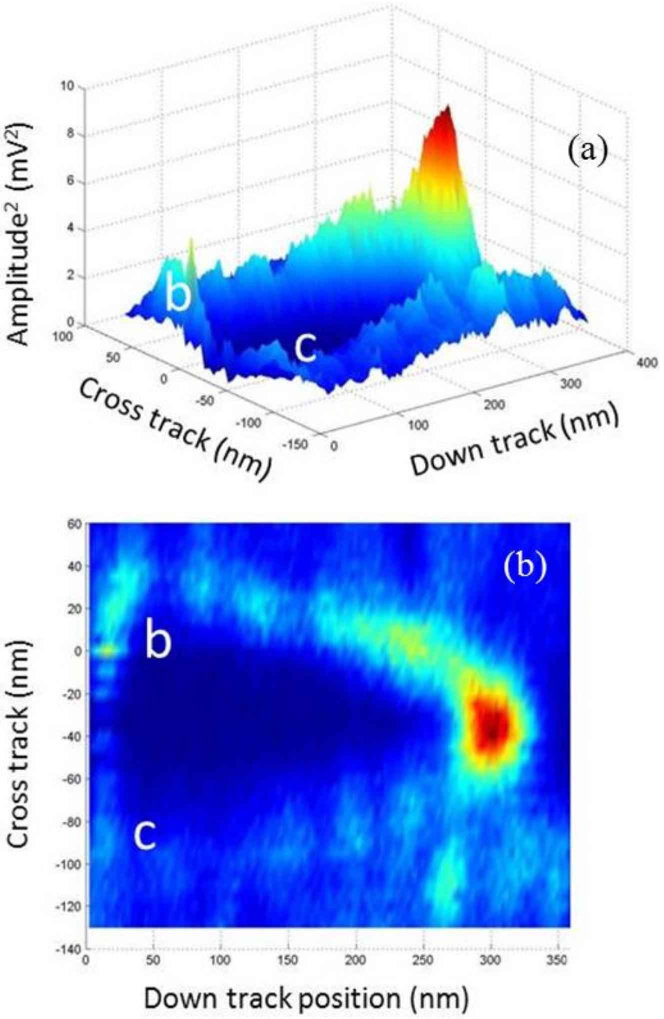

Figure 3 - 13 (a): 3*D* view of writer A’s cross track against down track noise profile at 45 *mA*

Figure 3 - 13 (b): Top view of writer A’s cross track against down track noise profile at 45 *mA*

Next, writer B’s footprint and noise profiles will be analyzed. In particular, the 25 *mA* and the 55 *mA* case have been chosen. (Figure 3-14)

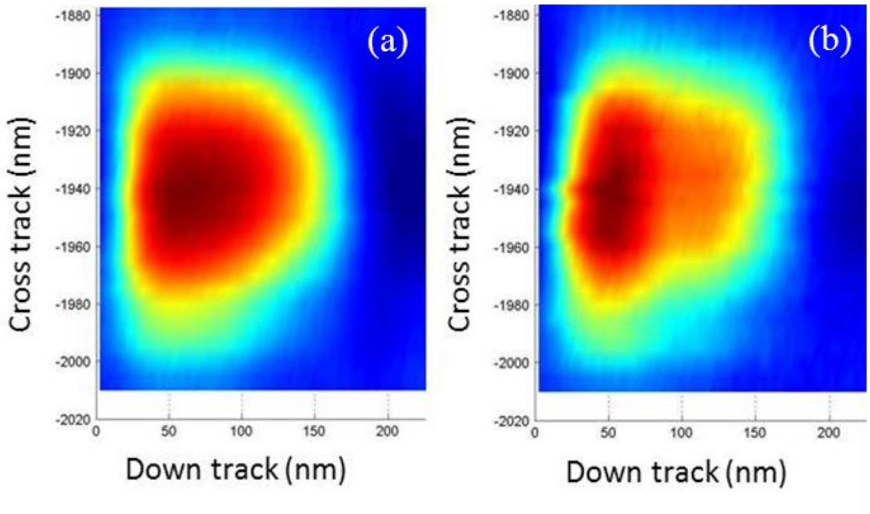

Figure 3 - 14 (a): Averaged writer profile of writer B at 25 *mA* after revolution and down track footprint averaging

Figure 3 - 14 (b): Averaged writer profile of writer B at 55 *mA* after revolution and down track footprint averaging

For writer B, the *PO* locations, *d*, *f* were observed to be more noisy as compared to the *NO* locations, *e*, *g*. (Figure 3-15, 3-16). This could be due to the footprints having more curvature in *PO* locations as observed from the Figures 3-14 (a) and (b) and thus less sharp transitions in these regions. Also due to the less uniformly shaped footprint of writer B as compared to writer A, the error locations tend to creep more from the trailing edge towards the footprint center due to its fringing fields from the trailing edge.

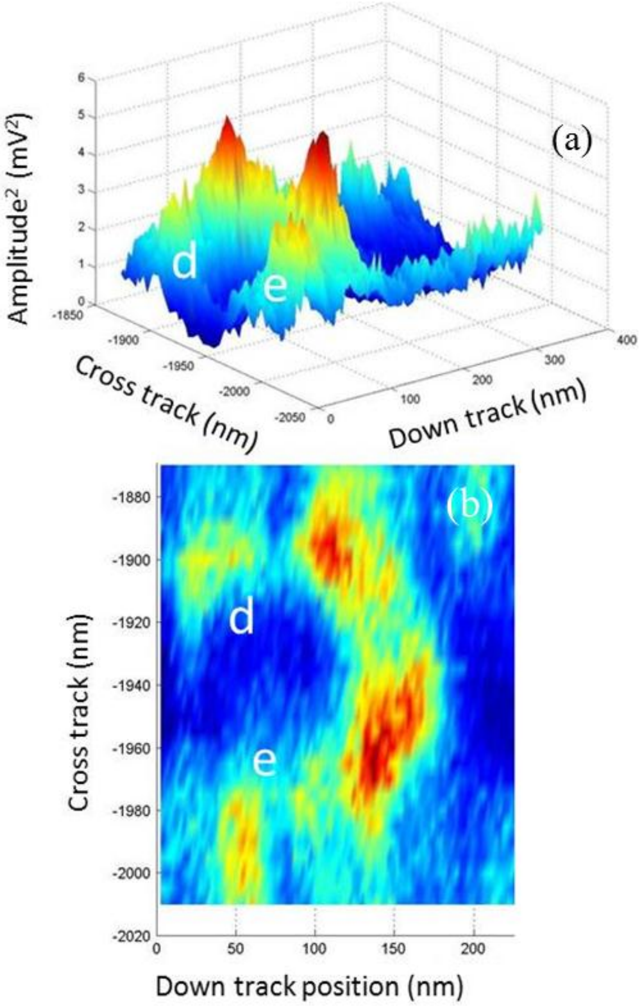

Figure 3 - 15 (a): 3*D* view of writer B's cross track against down track noise profile at 25 *mA*

Figure 3 - 15 (b): Top view of writer B's cross track against down track noise profile at 25 *mA*

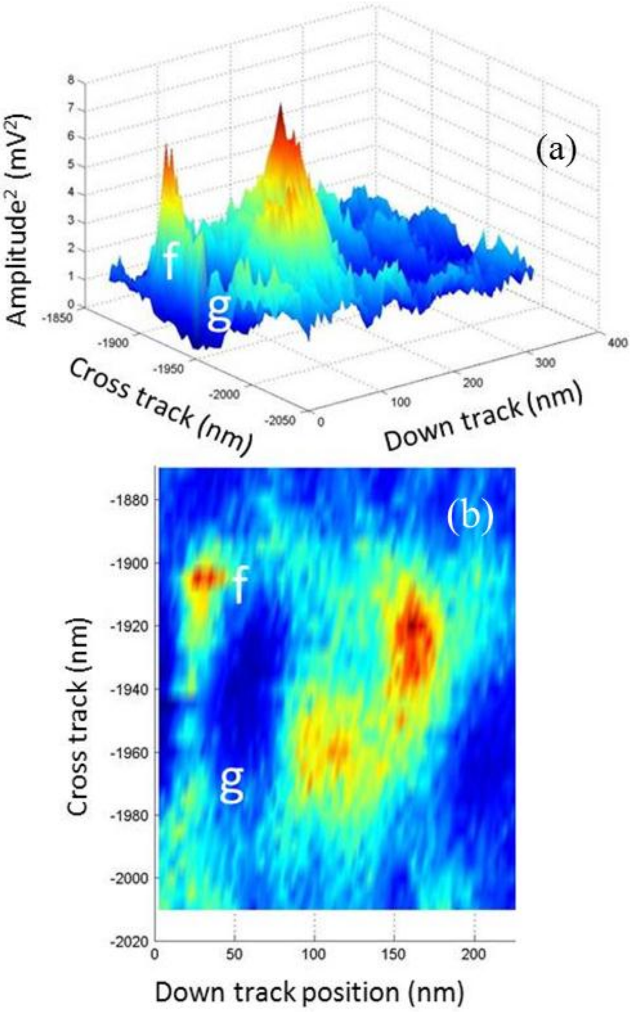

Figure 3 - 16 (a): 3*D* view of writer B's cross track against down track noise profile at 55 *mA*

Figure 3 - 16 (b): Top view of writer B's cross track against down track noise profile at 55 *mA*

3.3.2 *SNR* Analysis

SNR analysis is next conducted using the footprint and noise profile data. Since the region of interest is only the trailing edge of the writer profile, footprint and noise profile data near those regions are first isolated and then calculation of the *SNR*s are carried out for the different writing conditions.

Three different regions are isolated, namely the footprint track center (*TC*) locations, locations that are of *NO* regions from footprint track center and locations that are of *PO* regions from footprint track center. Each *SNR* value could be used accordingly depending on the purpose. *TC* locations are of more importance as it is the region where the data will be written on the track.

Figures 3-17 and 3-18 show the graphs of three different *SNR*s calculated for writer A and B respectively. The downward triangle data marker represents the accumulated *SNR* for the *TC* region; the upward triangle type data marker represents the *SNR* for the *PO* locations, while the circle type data marker represents the *SNR* for the *NO* locations namely the negative offset regions of the footprint data.

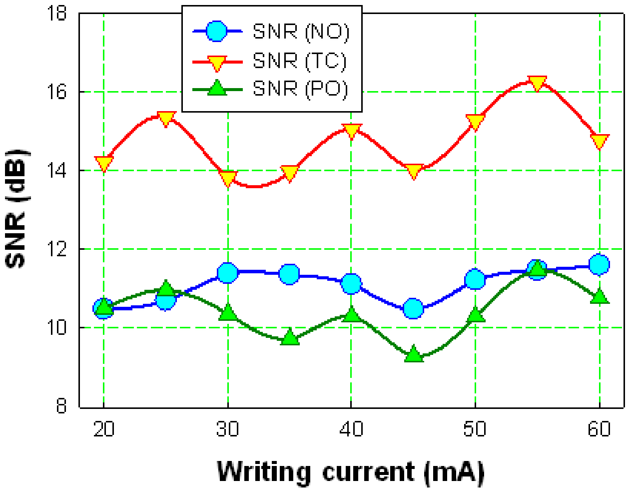

Figure 3 - 17: A plot showing the *SNR* of writer A's trailing edge region against the different writing currents, 55 *mA* is the optimal writing condition here

Writer A has a more consistent *SNR* profile in which the *SNR* increases to a maximum at 55 *mA* and drops when below 55 *mA*. The general trend is that by increasing the writing current for writer A, the *SNR* is improved. The decrease in the *SNR* when above the 55 *mA* could be explained by stronger fringing field particularly at the *PO* locations as seen by the *SNR* drop in the *SNR_PO* graph for Figure 3-17.

These fringing fields can increase the write bubble size rather randomly, thus producing issues of random switching at those regions.

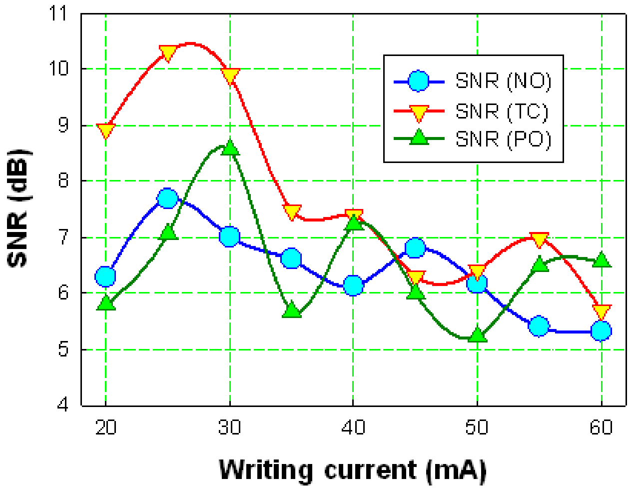

Figure 3 - 18: A plot showing the *SNR* of writer B's trailing edge region against the different writing currents, 25 *mA* is the optimal writing condition here

As for writer B, besides having poorer *SNR*, the general trend is that the writer displays poorer *SNR* when current increases above 25 *mA* (Figure 3-18). It suggests that the fringing field for writer B becomes stronger at the trailing edges especially for this head-media combination when current increases.

3.3.3 Conclusion for the 1st part of chapter

The experiments and analysis suggest that depending on the writing process, extra medium noise which is the dominant noise in the perpendicular recording system, could be introduced to the media, thus it is important to determine optimal writing conditions for the head-media combination. With these useful noise profiles and footprint data at different writing conditions for different head-media combinations, a better understanding of the optimal writing conditions could then be obtained. For the head-media combination used in the experiment, based on the overall *SNR* measured, writer A has optimal writing conditions at 55 *mA* while writer B at 25 *mA*. Writer A also exhibits a more consistent and predictable *SNR* performance compared to writer B and thus is a more suitable writer to be used on the media. It is to note however that these methods to determine the writing condition here has to be complemented with standard 747 and *BER* tests to further verify the performance and recording density of the selected head-media combination.

In this section, the medium noise profiles have been derived by doing averaging using the read-back footprint data. In the following section, this methodology to derive the footprint data together with a different processing method will be used to look at the jitter distributions across the track at different offset positions.

3.4 Probabilities of transition jitter at different off-track positions

Unlike the case in section 3.3, where the individual footprints have to be extracted based on the fulfillment of the 3 conditions, there is no need to do so in this section of work. The rationale of fulfilling the 3 conditions in section 3.3 is so that no false positive footprints are retrieved to affect the analysis of the experiments, and to reduce the effects of jitter noise affecting the analysis of write process induced media noise.

In this section, the characteristics of jitter noise are of importance, therefore the individual footprints and their footprint dimensions are simply extracted out at regular intervals from the retrieved signal data set based on the sampling rate, media spinning speed and the written frequency. The statistical characteristics of noise can be derived from the individual noise footprint which shows the media noise characteristics induced by writing process. Each individual set of footprint data will thus contain the jitter information that is embedded around the transition edge of the footprint.

The gradient along the down track direction is initially calculated for the whole footprint. The maximum gradient point across the cross track is then defined as the transition point. With this process, each individual footprint's transition location at the trailing edge across the whole cross track is thus collected. Jitter could occur when the writer writes at an offset to the ideal desired location due to multiple reasons: *NLTS*, physical issues. So, a control, which is an averaged footprint waveform, is required so that the statistics of the jitter profile for the individual footprints can be determined based on this averaged waveform's transition points across the cross track. This explains the need to know the transition points.

To retrieve the noise free writing profile of the footprint to be used as a control, each extracted footprint is averaged. By enough averaging of the footprints along down track direction, both the medium noise and writing field fluctuation can be removed as well. At each off-track position, the individual waveform from writer footprint is fitted with averaged noise free waveform by down track scan. The shifting amount with the least square fitting is measured as the transition jitter of this particular waveform. Each individual set of jitter transition data is then used for the statistical analysis to determine the jitter profile of the footprint at different off-track positions. This process is carried out and repeated with different writing currents and head.

200 footprints have been used in the experiments. It is to note that due to the sampling rate at 10 *GS/s*, the jitter sensitivity detected is limited to approximately 1.25 *nm*. Jitter that is less than 15 *nm* occurring near the track center shall be the focus of the analysis as analysis of any jitter larger than that or at other regions will not be

meaningful. Those jitters will most likely be due to media defects or erroneous detection of transition edge.

3.4.1 Analysis of writer footprint and jitter profiles

A typical captured footprint and its corresponding 200 cycle's averaged footprint written at 50 *mA* using both writer A and writer B is as shown in Figure 3-19.

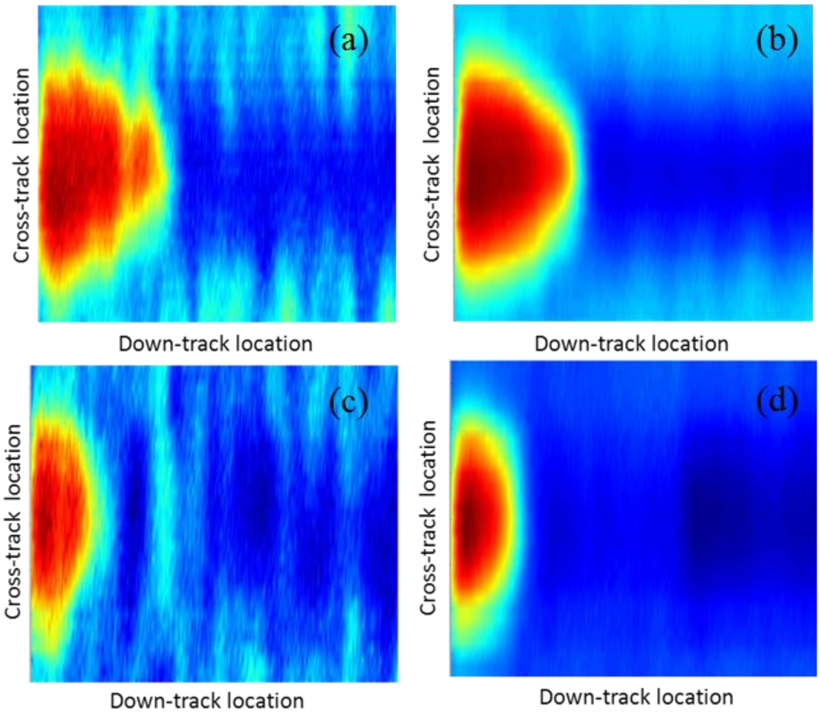

Figure 3 - 19 (a), (b): Writer A's single footprint and averaged footprint at 50 *mA* respectively

Figure 3 - 19 (c), (d): Writer B's single footprint and averaged footprint at 50 *mA* respectively

As could be seen from the figures above, the averaged footprint has a more uniform and consistent appearance as compared to the single footprint. The transition points are next determined by looking at the maximum gradient region of the footprint. The gradient plots of the averaged footprint of writer A and B are shown in Figure 3-20. The red area, which is the trailing edge of the footprint, is of interest to us as it is the area where data is written on the media. It is the region where the largest gradients are retrieved cross-track and determined as transition points and where the transition curvature could be seen.

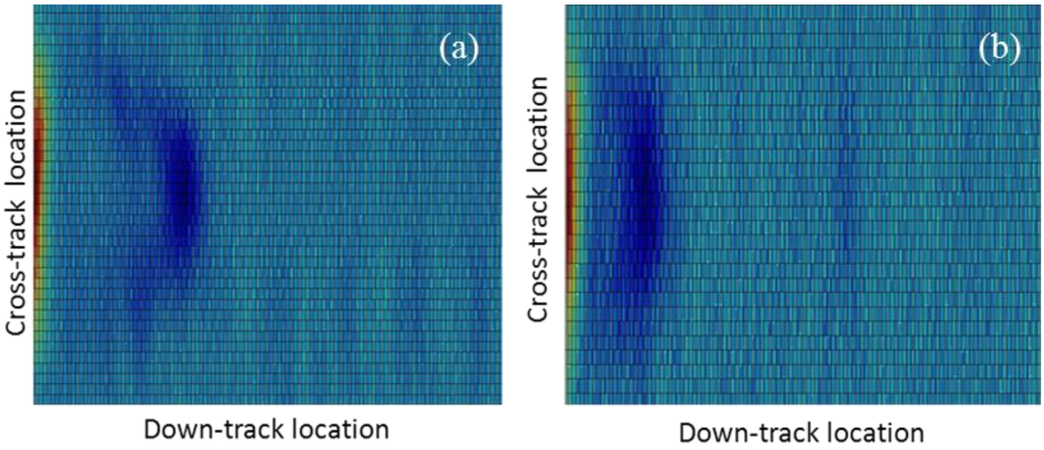

Figure 3 - 20 (a): Gradient plot of writer A's average footprint at 50 *mA*
Figure 3 - 20 (b): Gradient plot of writer B's average footprint at 50 *mA*

With the transition points and thus the calculated jitter profiles of the 200 footprints, the cross-track statistical transition jitter mean and standard deviation of the writer A and B at different writing currents are as plotted below in Figures 3-21 and 3-22 respectively

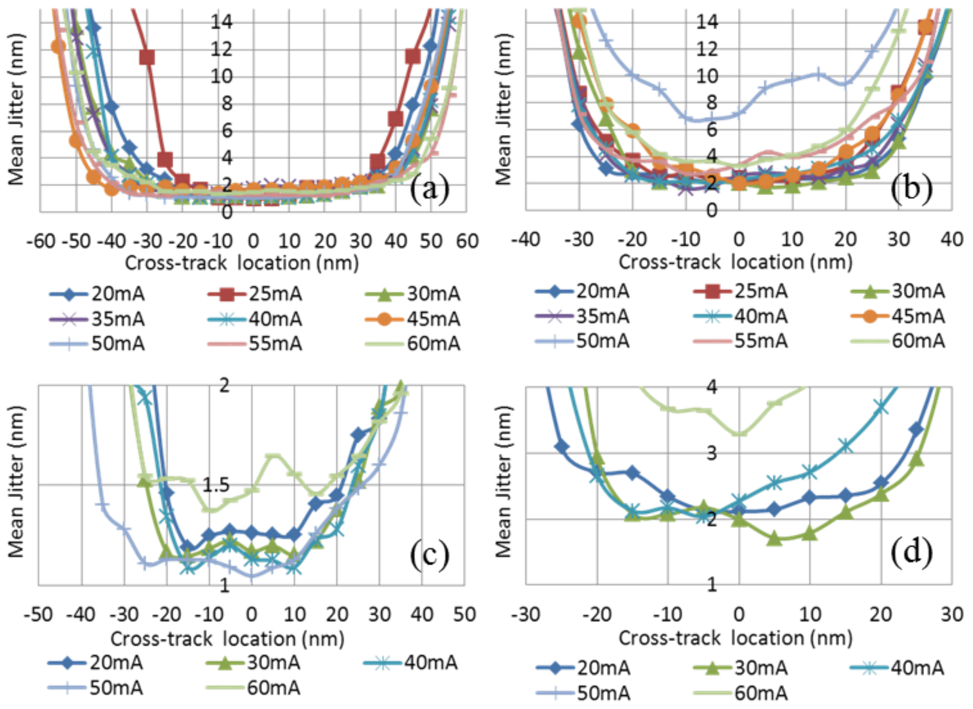

Figure 3 - 21 (a), (c): Writer A's mean profile of 200 footprint jitter data (un-zoomed and zoomed version)

Figure 3 - 21 (b), (d): Writer B's mean profile of 200 footprint jitter data (un-zoomed and zoomed version)

From the mean jitter and standard deviation plots, writer A is observed to have lower jitter mean and lower deviation across the tested writing conditions. Writer A also has a relatively wider 100 *nm* cross track region of low jitter mean (<8nm) as compared to the 60 *nm* cross track region of writer B. Also, it could be observed from Figures 3-21 (c) and 3-22 (c) that 50 *mA* could be an optimal writing condition to have the least jitter for writer A, as it has the lowest jitter mean and 60 *nm* of minimal jitter deviation about the center track. From Figures 3-21 (d) and 3-22 (d), it could also be observed that 30 *mA* is the optimal current instead of higher writing current for writer B. Especially for writer B; writing current higher than the optimal current has the effect of causing more jitter deviations fluctuating around larger jitters.

The info in Figures 3-21, 3-22 can be consolidated and by defining different regions to look into, a new insight and information to the writer/reader profile could be attained as well. From Figure 3-23, 2 different mean jitter plots for writer A and B have been plotted for 3 different regions namely the *TC*: track center region, *PO*: positive offset region, *NO*: negative offset region. The trend is consistent that for both writers, the *NO* region has a higher mean jitter profile as compared to *PO* and *TC* region. One possible implication is that if the heads are to be used for shingled writing purposes, it should be shingled using the *PO* region instead of the *NO*. It is to note that there is an unusual peak at the 50 *mA* case for writer B, which could be due to experimental errors. As expected, the *TC* region has the best mean jitter profiles.

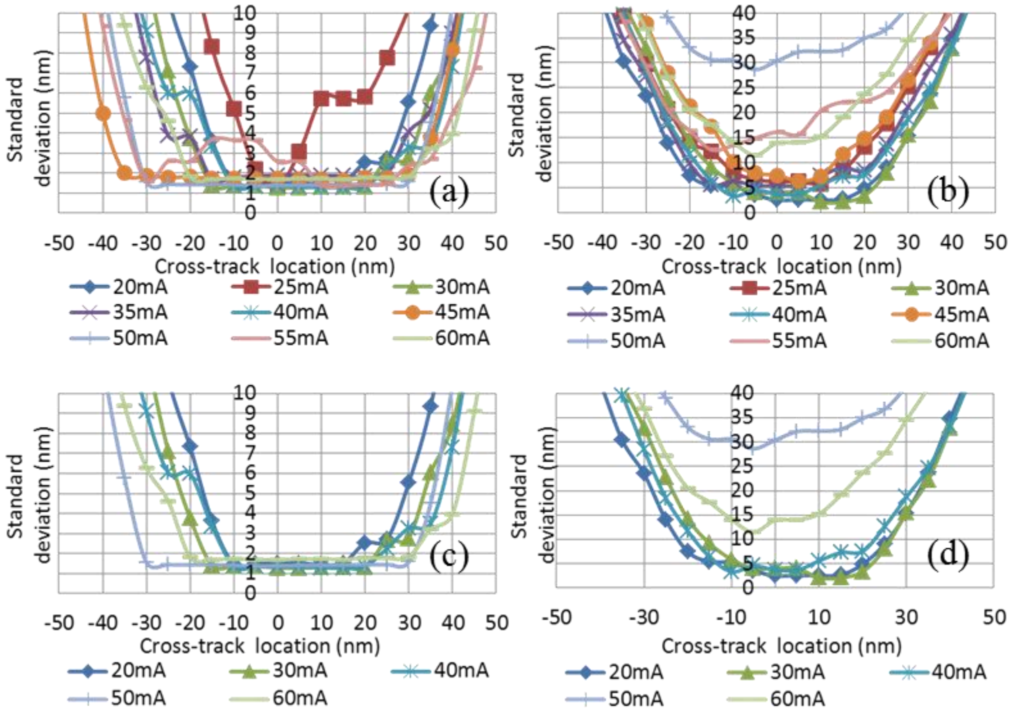

Figure 3 - 22 (a), (c): Writer A's standard deviation profile of 200 footprint jitter data (un-zoomed and zoomed version)

Figure 3 - 22 (b), (d): Writer B's standard deviation profile of 200 footprint jitter data (un-zoomed and zoomed version)

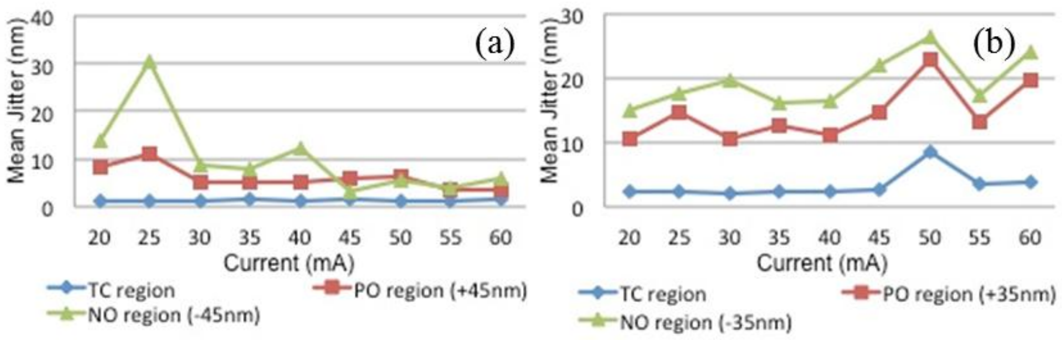

Figure 3 - 23 (a): Writer A's mean jitter profile vs writing current at 3 different regions (*TC*: track centre, *PO*: positive offset, *NO*: negative offset)

Figure 3 - 23 (b): Writer B's mean jitter profile vs writing current at 3 different regions (*TC, PO, NO*)

Next, let's look at the down-track probability distribution of jitter and its magnitude across the cross track. This will allow the users to have an innate understanding and view of the jitter profiles of different head-media combinations. The 50 *mA* case written using writer A has been chosen for the analysis.

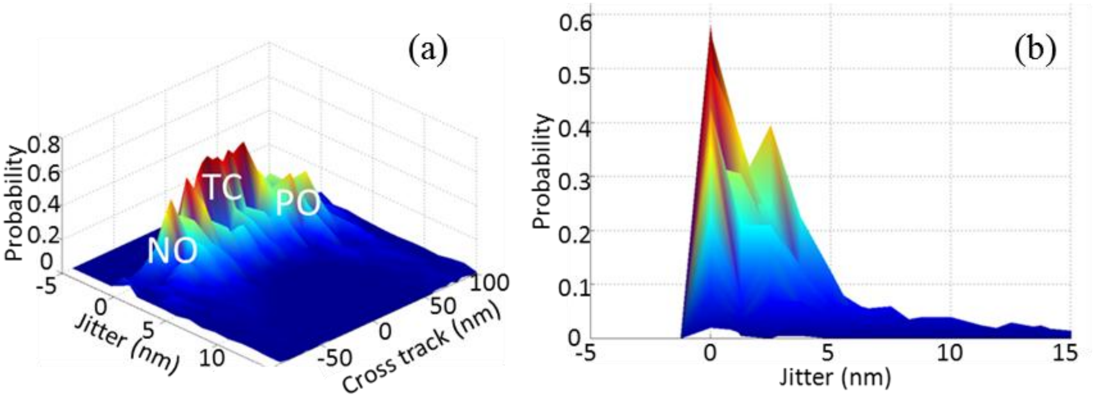

Figure 3 - 24 (a): Jitter profile (3*D* view)

Figure 3 - 24 (b): Jitter profile (Side View)

The 3*D* mapping of the transition jitter probability is plotted in Figure 3-24. From Figure 3-25 (b), at *TC*, there are around 60% of transitions having zero jitters. 35% of transitions have the jitter within 2-4 *nm*. At both track edges, the zero jitter transitions reduce to around 40%. From Figure 3-25 (c), at the *PO* regions from *TC*, up to 60% of transitions have the jitter within 2-4 *nm*. From Figure 3-25 (d), at the *NO* regions from *TC*, a wider spread of jitter of up to 15 *nm* was observed. By looking at the averaged footprint shown at Figure 3-25 (a), the reason why the transition jitter at the *NO* regions has higher variation is because the transition curvature is observed to be more at that region.

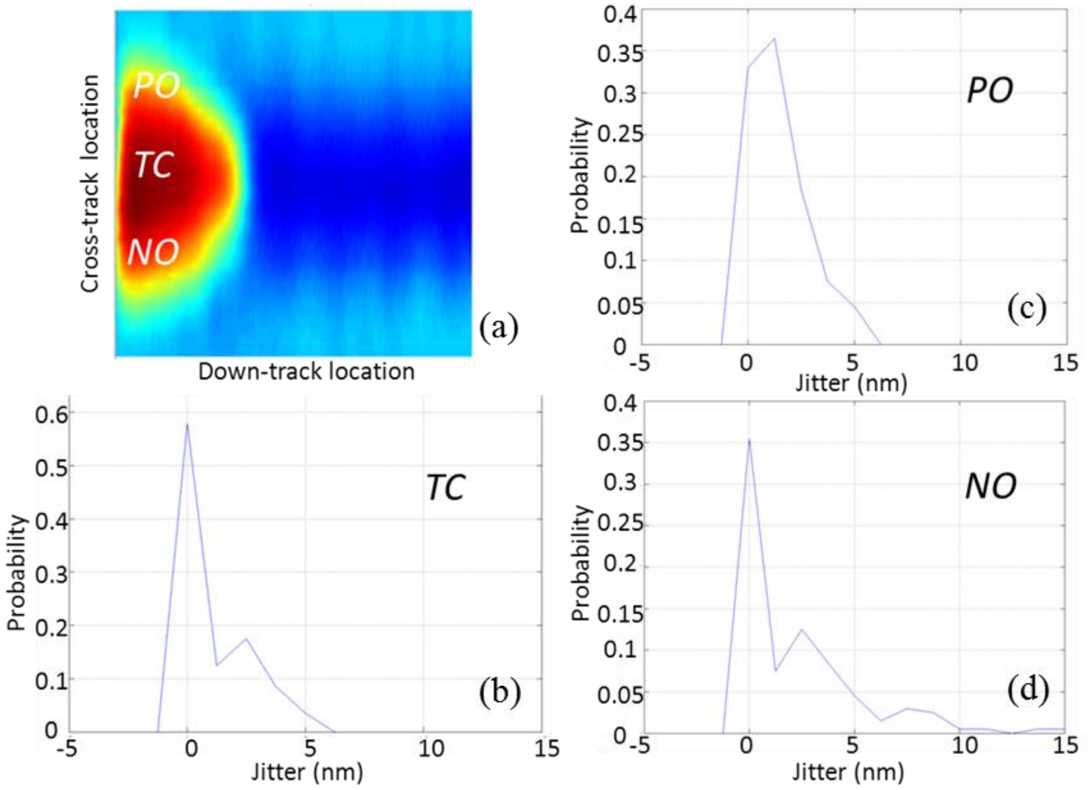

Figure 3 - 25 (a): Averaged footprint
Figure 3 - 25 (b): Jitter profile (*TC*)
Figure 3 - 25 (c): Jitter profile (*PO*)
Figure 3 - 25 (d): Jitter profile (*NO*)

3.4.2 Conclusion for the 2nd part of chapter

In this section, the setup and experimental methods used to retrieve the required multiple footprint and average footprint data for the purpose of calculating the jitter profile has been described. From the various cross- track and regionalized jitter distribution and probability plots, it is quite conclusive to determine that writer A at 50 *mA* especially at the *TC* has the minimal and thus best jitter profile amongst the other writing conditions and heads used. Having said so, it is to note that such test to determine the performance of demo head-media systems should also be accompanied with *BER* and 747 tests to further verify the density gain or loss. It is also to note that different read heads will result in differences in the jitter observed. However, the focus of this section is to compare between two different write/read heads and to look at the possible differences and conclusions that may result using the method that have been used to derive the jitter. In future works, the effects of jitter with different permutations of write/read heads could be investigated into using this method.

3.5 Conclusions

The different methods of applying averaging on the retrieved footprint data captured using the Guzik spin-stand have been discussed. The medium noise characteristics and jitter distributions across the track at different offset positions for different writing conditions by varying the write current have also been studied. Comparisons between two write/read heads have been made and the process of determining the better writer and better writing condition was also gone through. In the following chapters, transitions shall slowly be made to elaborate more about track edge noise and how the track edge noise affects the performance of the recording system, before chapter 5 concludes with a comparison of the areal density achievable with a shingled and a conventional recording system.

Chapter 4: Track edge noise measurement and its impact to bit error rates (*BER*) and off-track read capability (*OTRC*)

4.1 Introduction

In this section, the track edge noise measurement and its impact to *BER* and *OTRC* are studied.

In conventional perpendicular magnetic recording as illustrated in Figure 4-1, tracks are written in the down-track direction, adjacent to at least one or two nearby tracks in the cross-track direction. The effect of track edge erasures thus greatly affects the readability and integrity of the adjacently-located recorded tracks. It is thus important that hard disk manufacturers take this effect into account and design the maximum track capacity to write so as to maintain the reliability of the hard disk and also to squeeze the maximum areal density out of the designated head-media combination.

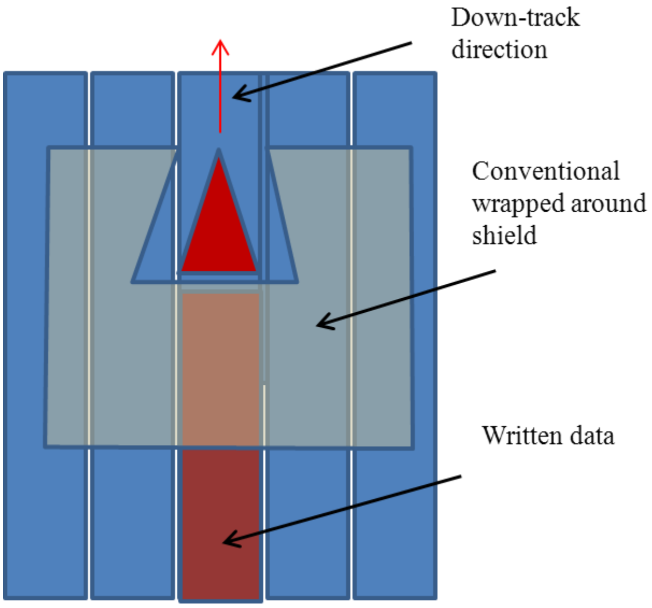

Figure 4 - 1: Conventional magnetic recording with its wrapped around shield

In shingled writing as illustrated in Figure 4-2, even though the recording is done with a well-enclosed side shield, there will still be track edge erasure effects at the region where the writer and its surrounding writer shield overwrites the pre-existing tracks. Similar for both cases of conventional and shingled recording, these track erasures affect data both at the cross track and the down track direction.

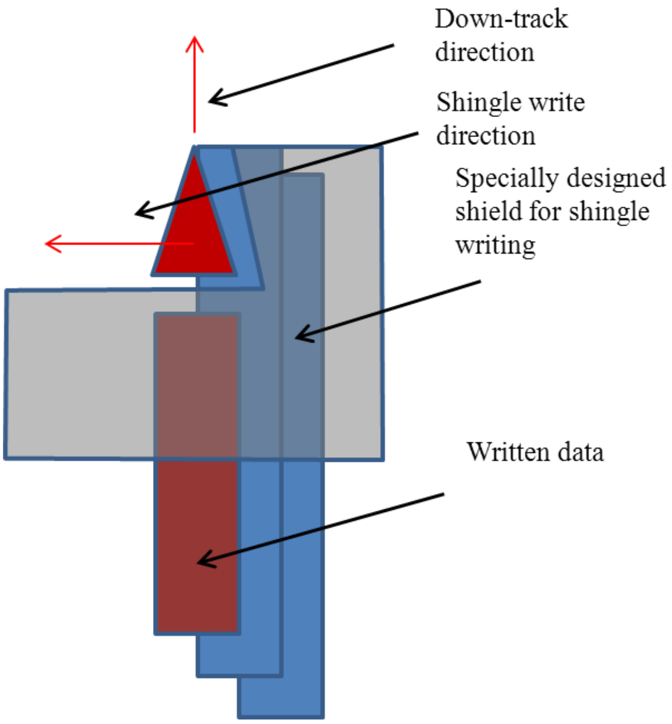

Figure 4 - 2: Shingled magnetic recording with its specially designed shield

The *BER* bathtub curve and 747 tests are the two important tests used in industries and academia to determine the performance and potential areal density of the head-media combination. In the setup, a *NPML* channel chip that is integrated with the Guzik spin-stand and controlled using the Anaconda software was used. This M7 error analyzer add-on board is shown in Figure 4-3. The integrated setup allows both tests to be conducted rather efficiently and results to be collected quickly with minimal hassles.

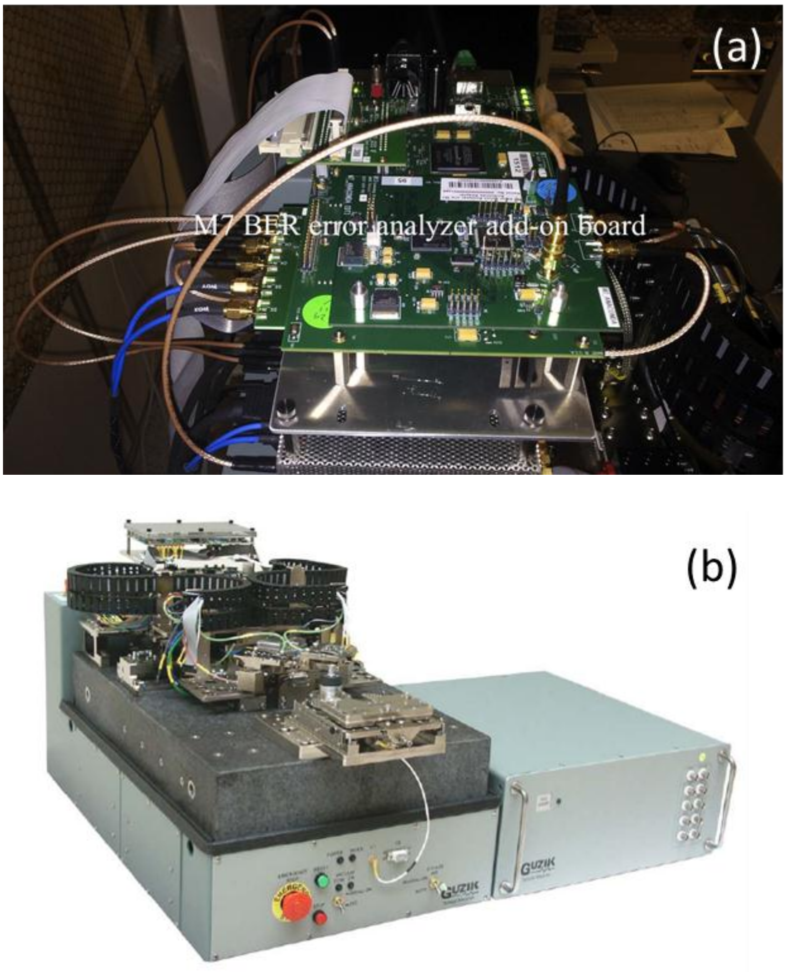

Figure 4 - 3 (a): M7 error analyzer add-on board for the Guzik spin-stand
Figure 4 - 3 (b): Guzik spin-stand DTR3004 setup

In a typical *BER* test, it simply measures the number of detected bit errors / total number of bits read. A good *BER* would range from 10^{-3} and below, which implies 1 bit error detected for every 1000 bits or more. In order to produce the *BER* bathtub curves for a targeted track of recorded data, data has to be written on the disk media first, and then the system will have to scan along the cross-track direction to detect the *BER*. Figure 4-4 illustrates the typical movement of the reader during the *BER* data retrieval process. Once a particular location has completed registering its *BER*, another cross-track position will be chosen until the full *BER* track or bathtub curve profile is retrieved.

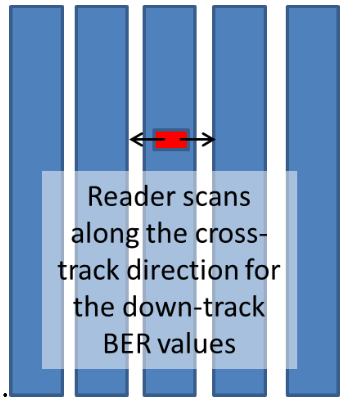

Figure 4 - 4: Typical movement of the reader when it scans cross-track along the down-track direction for the *BER* values.

Figure 4-5 shows a typical *BER* profile when a data track is squeezed from the negative offset by an approaching *AC* track. It is observed that when the reader scans at an offset from the data track, it registers more and more *BER* and the curve registers an increase in the magnitude. When it reaches the optimally written region which is usually the center of the data track, the *BER* is the lowest, in this case is near 10^-5. The *BER* bathtub curve allows the users to grasp the *BER* profile of the data track(s) across the cross track. However, it is not enough to determine the areal density achievable from the head-media combination, which is one of the reasons why 747 tests are used instead to determine the achievable areal density.

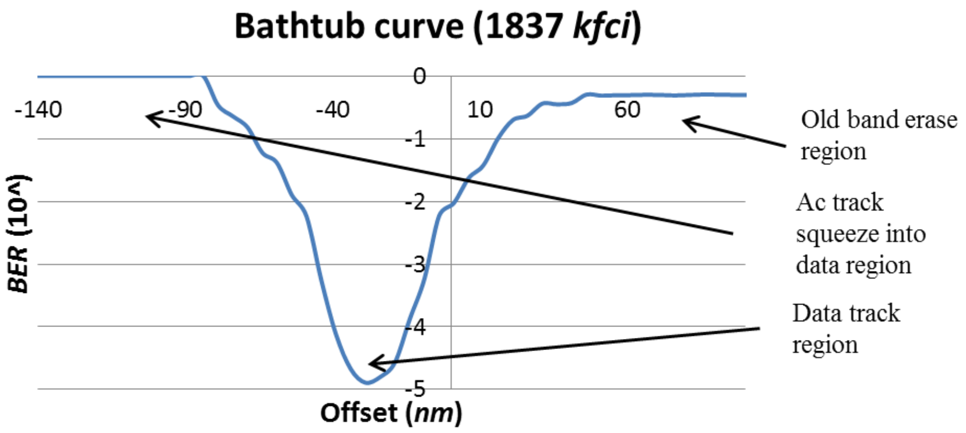

Figure 4 - 5: Typical *BER* curve with a single side *AC* erasure track squeeze from the negative offset

A typical 747 test [74], as illustrated in Figure 4-6, requires *BER* bathtub curve profiles to be conducted. The additional experimental step taken is such that different degrees of the squeezing of the tracks are introduced to the system before the *BER* bathtub curve profiles are derived. Another difference is that while doing the *BER* bathtub curve experiments, the value registered and plotted is not the *BER* value, but is more of the distance from the center of track such that the *BER* still satisfy the *BER* criterion defined by the users. This distance allows the users to know the *OTRC* of the system at different degrees of track squeezing.

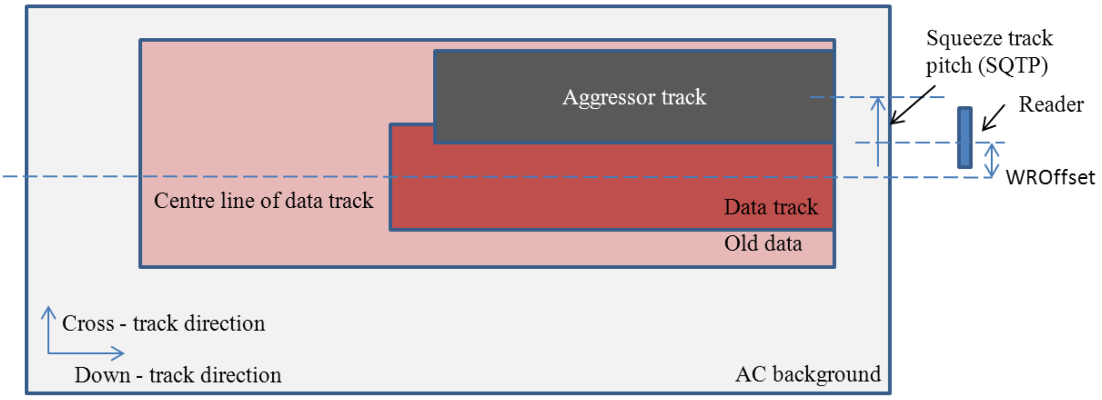

Figure 4 - 6: Illustration of a typical 747 test scheme

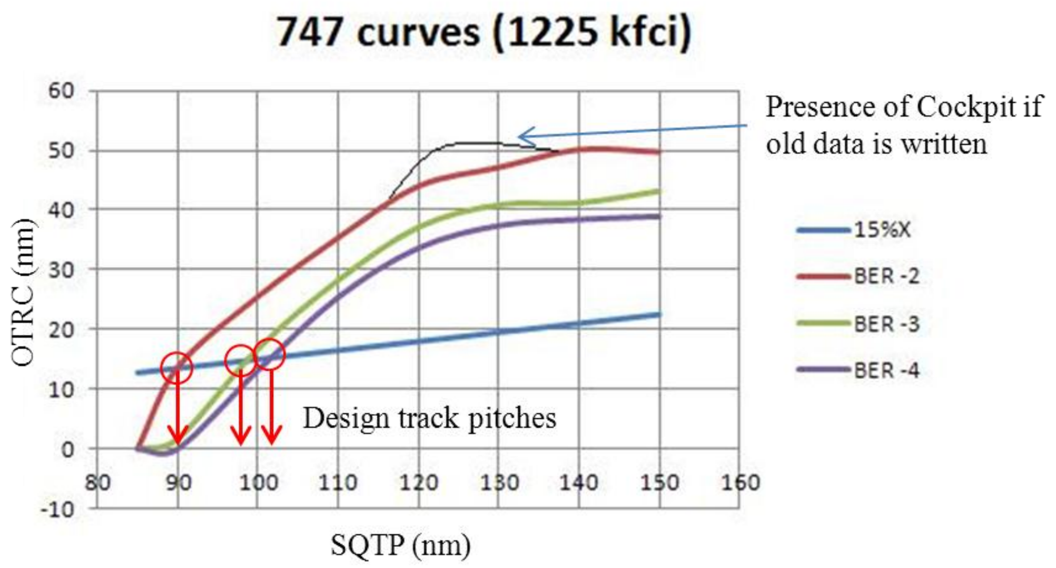

Figure 4 - 7: Design track pitches for the 747 curves

With this Figure 4-7 of *OTRC* against different degrees of track squeezing and the interception point between the plot of the *OTRC* having 15% squeeze track-pitch (*SQTP*), design track pitches could be derived for the system at different *BER* which in turn could be used to determine the achievable areal density of the system. One thing to note is the deliberate addition of cockpit illustrated in the Figure 4-7. This cockpit would typically be present at good writing and detection conditions and when the squeeze is conducted at small intervals with old data pre-written before the data track. The presence of the cockpit is due to the fact that the adjacent track erase band overwrites the old information between tracks. The erase band noise degrades the *SNR* to a lesser extent than the overwritten old information, and *OTRC* is thereby enhanced. However, when the threshold SNR is raised sufficiently, the reader is unable to fully cross the erase band of the data track. In that case, the reader fails before it can get to old information, whether it has been overwritten or not. Therefore, when the *BER* threshold is high, there can be no cockpit. Similar arguments explain the vanishing 747 cockpit with increasing linear density (the on-track *BER* decreases), and when the erase band width is increased [75]. The 747 tests and determined areal density values shall be conducted and determined in the chapter 5 where both the conventional and shingled writing scheme will be compared.

4.2 Experimental setup and results

In the experiments, a spectrum analyzer is used to capture the read-back data after the media is overwritten with different types of writing frequencies (single tone). The purpose of doing so is to investigate the nature of the writing effect and its corresponding noise floor and track edge noise at different writing conditions. A commercial disc platter, 375 *Gb*/platter is used for the experiments.

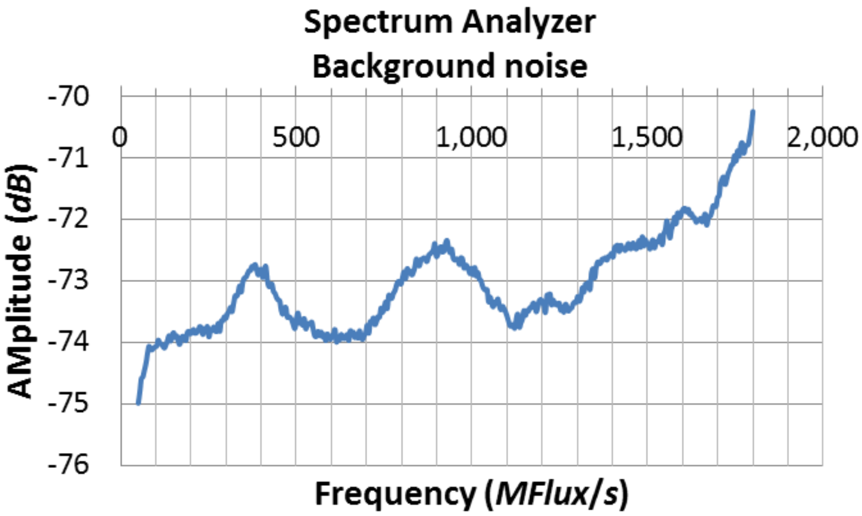

Figure 4 - 8: When no data is input, spectrum analyzer displays a higher decibel of background noise at the higher frequencies

In the setup, the spectrum analyzer used has higher background electronics noise at the higher frequencies as shown in Figure 4-8. This background noise will be subtracted from the read-backs to retrieve the actual frequency spectrums at different writing conditions.

4.2.1 Track center spectrum measurements

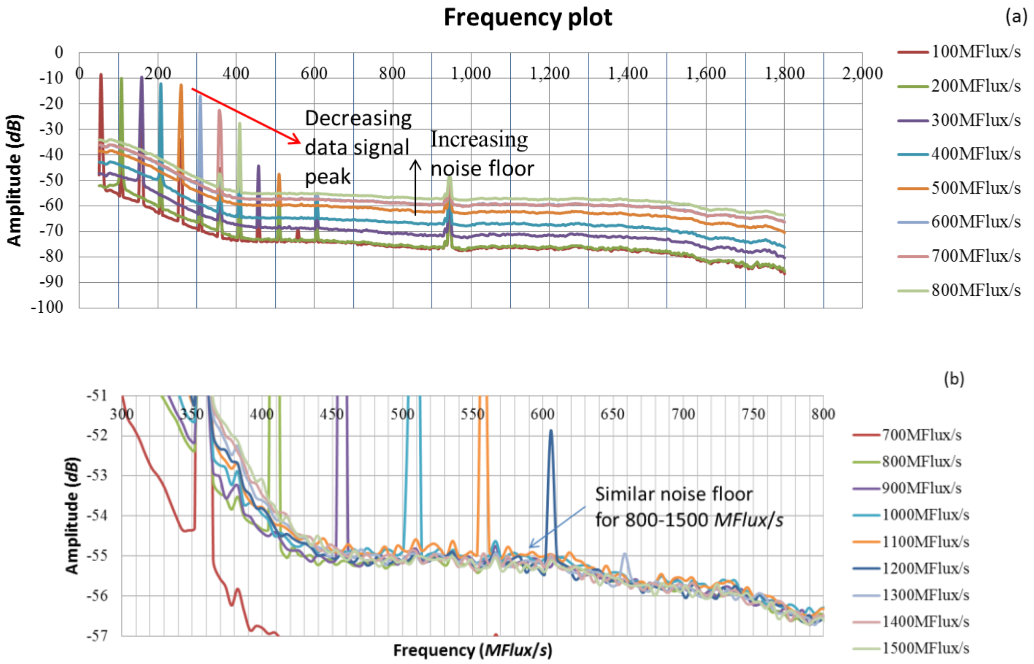

Figure 4 - 9 (a): Frequency plots of the read-back at different frequency writing
Figure 4 - 9 (b): Zoomed in plot at the noise floor for 800-1500 *MFlux/s* frequency data

Figure 4-9 shows the plot of the different spectrums for different frequency writing. All these measurements are done at the track center and from the plots, a few observations could be seen:

1) noise floor increases as data frequency written increases from 100-800 *MFlux/s*, suggesting that there's a higher probability of poorer switching of grains at higher frequency writing
2) noise floor stays around the same from 700-1500 *MFlux/s* but signal of data peak decreases, *SNR* drops

3) After 1300 *MFlux*/*s*, data signal is no longer readable by the read head, which is a combination of the limited resolution of the read head and the writability and thermal stability of the media at higher frequency writing

4) It is to note that consistent peaks are detected at 357, 934, 944 *MHz* and this 944 *MHz* peak is always present at different writing conditions, independent of the spinning speed of the disc. These frequencies are characteristics of the servo and mechanical system and are not really influenced by the change in the writing conditions so will not be of focus in the studies.

4.2.2 Time-domain view of the signals written

After looking at the frequency domain signals, a more innate and intuitive way of understanding the characteristics of magnetic recording would be to look at the time domain signals.

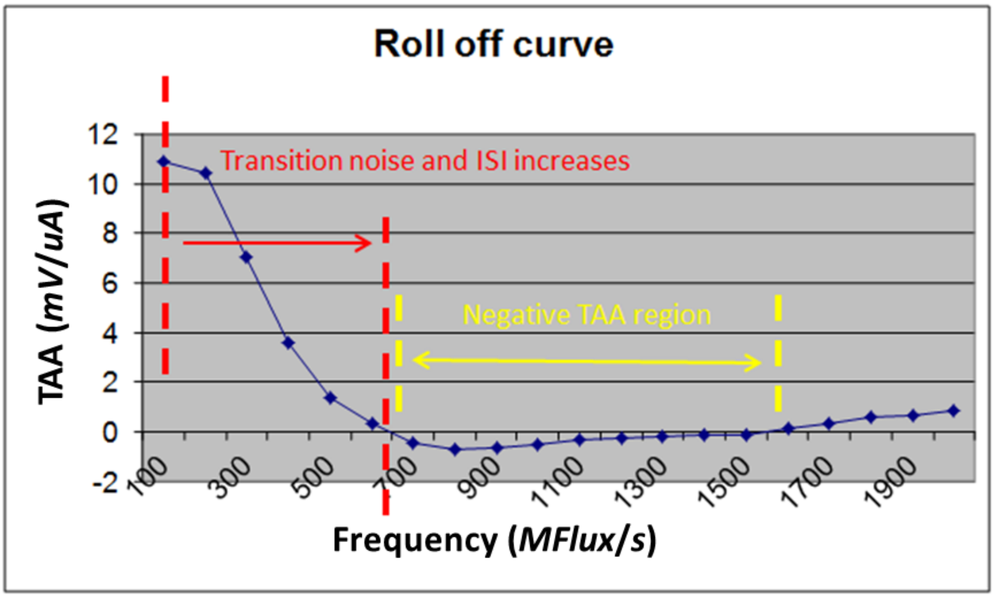

Figure 4 - 10: Experimental data of the frequency roll-off curve done using Guzik spin-stand

Figure 4-10 shows the frequency roll-off curve of the system, which is conducted also at the track center. This curve has been fitted with consideration of the background *AC*-erased signal. It is observed that as higher frequencies are written, the *TAA* of the read-back signal decreases. The reason is because at higher frequency recording, the transitions are located nearer to each oriented magnetization. Due to the more closely packed magnetizations, it is expected for each of the neighboring magnetized dipoles to influence each other. Depending on the orientation of each magnetic dipole which is either magnetization or demagnetization fields, this will influence the written jitter performance of the writer head as well as the read-back signal detected by the reader. In general, these interactions from the media layer influencing the read-back signal are known as *ISI*s. In this situation, these *ISI*s cause the read-back signal to decrease in the detected magnitude.

In the Figure 4-10, it is observed that a negative *TAA* region exists at the frequencies of around 600-1600 *MFlux*/*s*. The negative *TAA* effect shall be investigated on in the subsequent experiments. Before that, the individual cross track profiles at different writing frequencies to look at the *TAA* trend across the tracks; shall be investigated.

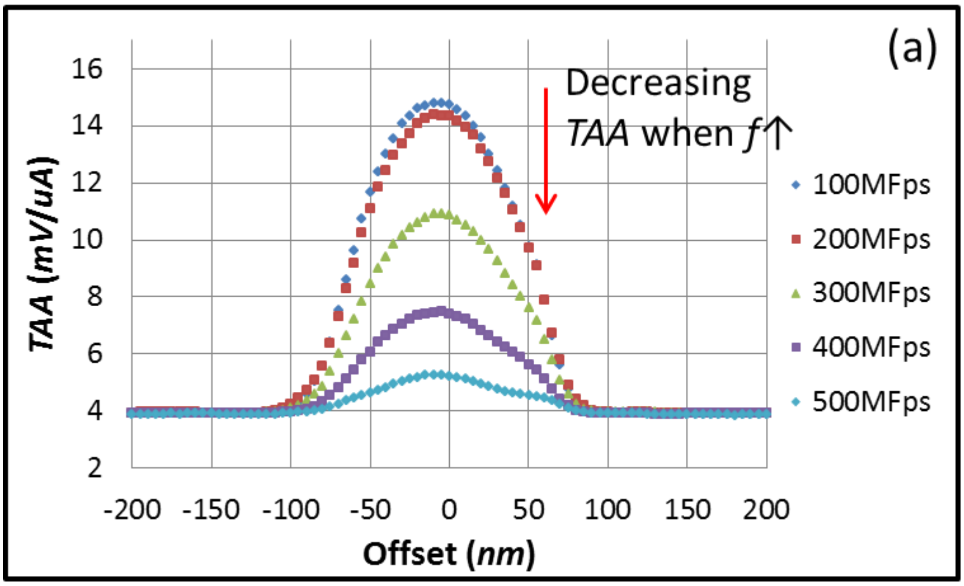
(a)
Decreasing
TAA when *f*↑
16
14
12
10
8
6
4
2
TAA (mV/uA)
-200 -150 -100 -50 0 50 100 150 200
Offset (*nm*)
100MFps
200MFps
300MFps
400MFps
500MFps

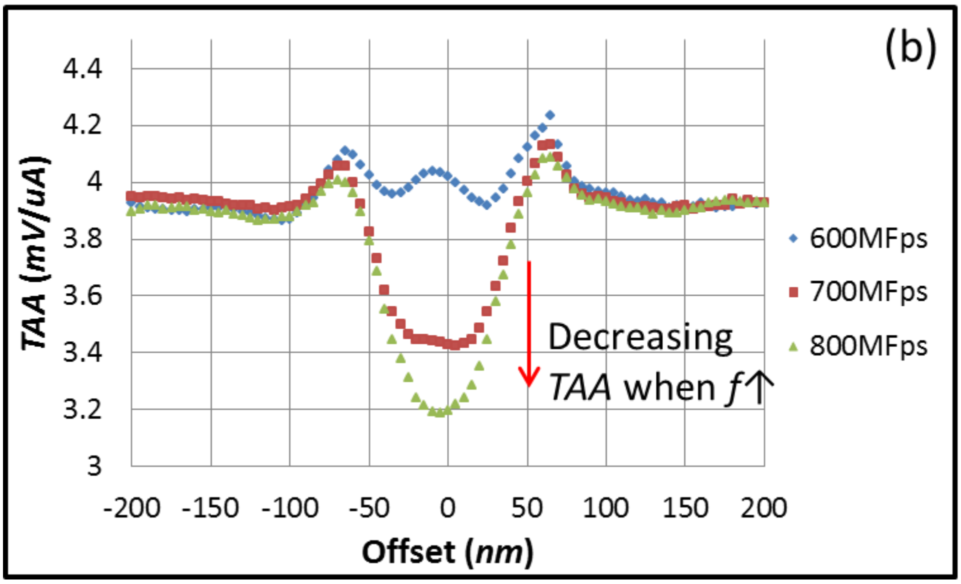
(b)
4.4
4.2
4
3.8
3.6
3.4
3.2
3
TAA (mV/uA)
-200 -150 -100 -50 0 50 100 150 200
Offset (*nm*)
Decreasing
TAA when *f*↑
600MFps
700MFps
800MFps

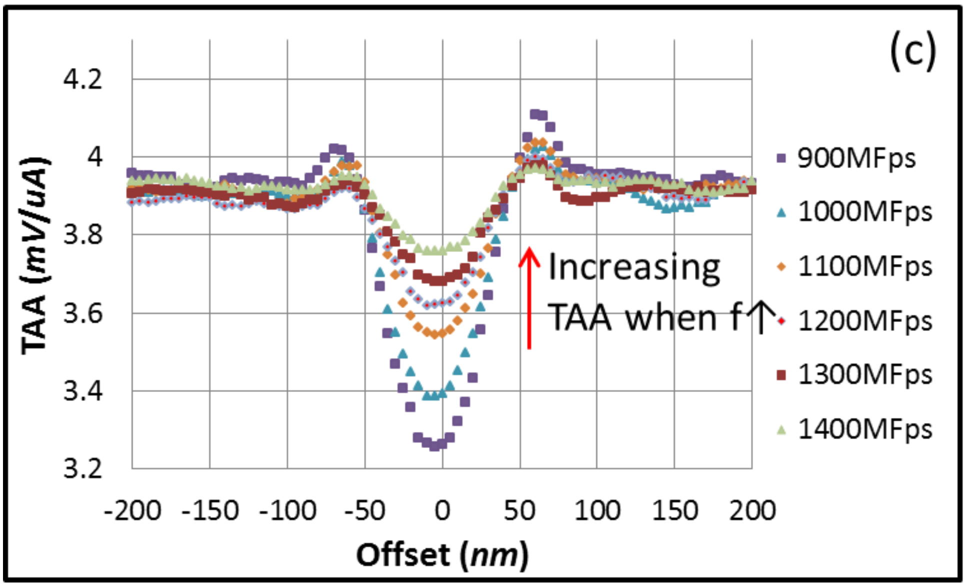
(c)
4.2
4
3.8
3.6
3.4
3.2
TAA (mV/uA)
-200 -150 -100 -50 0 50 100 150 200
Offset (*nm*)
Increasing
TAA when f↑
900MFps
1000MFps
1100MFps
1200MFps
1300MFps
1400MFps

Figure 4 - 11 (a): *TAA* of written frequency 100-500 *MFlux/s* at 22 *mm* location with media rotating at 5400 *rpm*

Figure 4 - 11 (b): *TAA* of written frequency 600-800 *M Flux/s* at 22 *mm* location with media rotating at 5400 *rpm*

Figure 4 - 11 (c): *TAA* of written frequency 900-1400 *MFlux/s* at 22 *mm* location with media rotating at 5400 *rpm*

In the Figures 4-11 (a, b), it was observed that as the frequency of the writing increases, due to the ISIs, the *TAA* of the written track decreases. As shown in Figure 4-11 (a), it decreases to a point at which when it reaches 600 *MFlux/s*, the track center region appears to be of the same magnitude as the background cross-track profile of around 3.9 *mV/µA*.

After 600 *MFlux/s*, a negative *TAA* effect was observed in Figures 4-11 (b, c) such that the signal drops below the background signal level. This effect suggests that during the single track writing at the track center, the energy causes the magnetization at the track center region to interfere with each other more as compared to the AC erased background. As the background *AC* erasure is done by scanning the write head across the cross track at certain fixed intervals, these overlapping writing effects caused by the write bubble is able to cause certain alignment of the magnetic dipoles. These alignments results in the higher *TAA* read-back magnitude of 3.9 *mV/uA*. In comparisons to the single track write when frequencies such as 600-1400 *MFlux/s* are used by looking at the frequency plot that was plotted in Figure 4-9 (a), it is observed that as the frequency written increases, the detected signal peak at the written frequency decreases substantially, whereas the background noise level also increases. This effect causes the detected *TAA* to continually decrease to the background *AC* level. This drop continues until 900 *MFlux/s* case.

From Figure 4-9 (b), it was noticed that the background noise level of 800-1500 *MFlux/s* is almost of similar level whereas the detected data frequency will drop substantially. Together with the single track write in comparison with the band erase *AC* background, this effect apparently has the effect of causing the negative *TAA* effect at the track center as shown in Figure 4-11 (b, c).

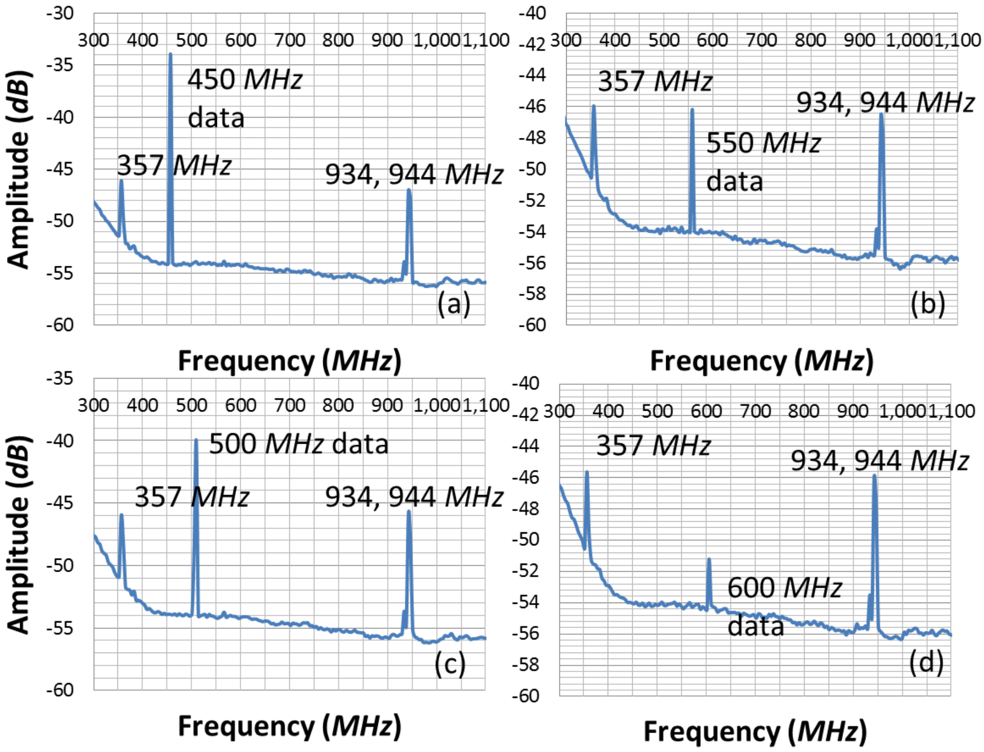

Figure 4 - 12 (a): 900 *MFlux/s* writing at 22 *mm* location with media rotating at 5400 *rpm*

Figure 4 - 12 (b): 1100*MFlux/s* writing at 22 *mm* location with media rotating at 5400 *rpm*

Figure 4 - 12 (c): 1000 *MFlux/s* writing at 22 *mm* location with media rotating at 5400 *rpm*

Figure 4 - 12 (d): 1200 *MFlux/s* writing at 22 *mm* location with media rotating at 5400 *rpm*

For the 900-1200 *MFlux/s* writing, there is a observed drop in magnitude of the data frequency peak from the spectrum analyzer whereas the other detected prominent peaks remain relatively similar in magnitude as shown in Figure 4-12 (a, b, c and d). As described earlier, instead of decreasing in the *TAA*, it is observed that the *TAA* starts to increase when the frequency is increased from 1000 *MFlux/s* onwards. It is observed from the spectrum data that that is when the data peak is at a higher frequency than the 357 *MHz* peak, and when the data peak's power detected is lower than the 357 *MHz*. We hypothesized that it is a combination of the always present systemic frequency peaks, the decrease in the data peak, and the increase in frequency of the data peak above the lowest detected systemic frequency of 357 *MHz* that causes this effect of increasing *TAA*. However, due to scope of this section, which is to look especially at the track edge region noise, the analysis of this set of data shall terminate here. Further in-depth investigations could be carried out in future works.

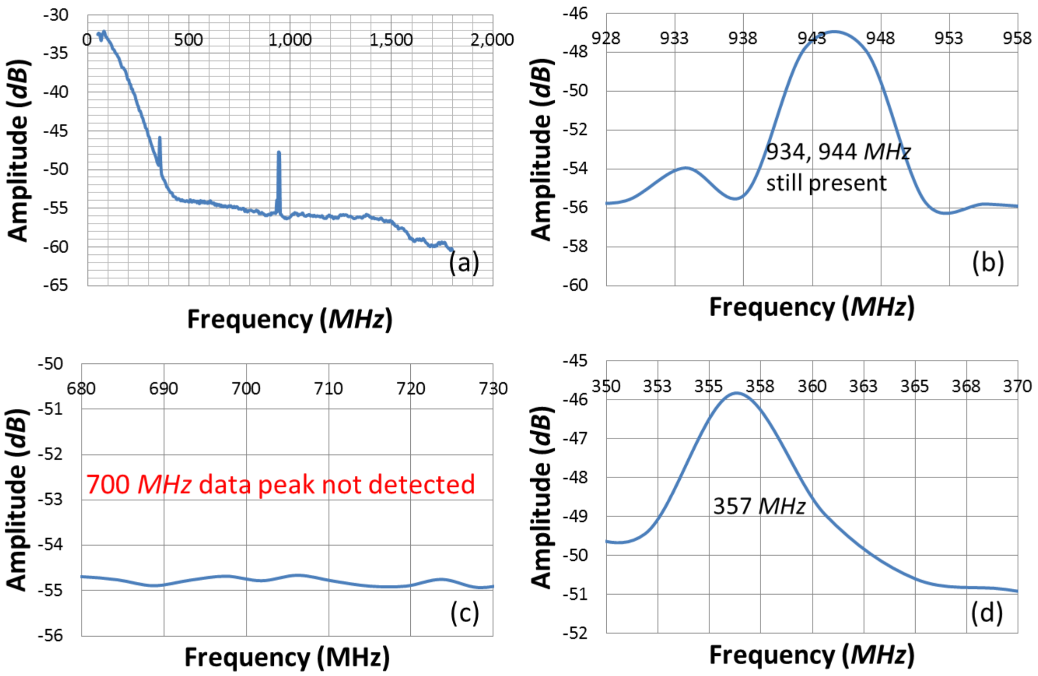

Figure 4 - 13 (a): 1400 *MFlux/s* writing
Figure 4 - 13 (b): 934, 944 *MHz* system peak still present in 1400 *MFlux/s* writing
Figure 4 - 13 (c): 1400 *MFlux/s* data peak not detected
Figure 4 - 13 (d): 357 *MHz* system peak still present in 1400 *MFlux/s* writing

From Figure 4-13, which the writing is also done at 22 *mm* location with media rotating at 5400 *rpm*, it is noticed that even though the other systemic frequency peaks are still present, the data peak is no longer present in the 1400 *MFlux/s* recording.

This explains the rationale why the analysis for Figure 4-11 is restricted to 1400 *MFlux*/*s* and below.

4.2.3 Selected case study

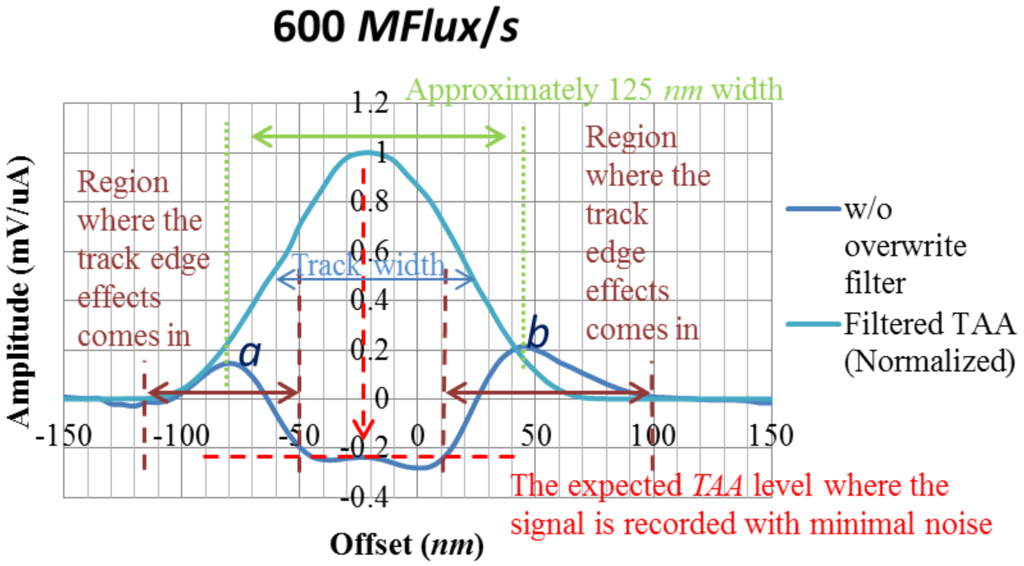

Figure 4 - 14: Track average amplitude (*TAA*) of the cross-track profile of the 600 *MFlux*/*s* writing read-back with and without the overwrite filter

For the next analysis, the 600 *MFlux*/*s* writing case is chosen as the primary focus. It has comparable noise floor to the 700 *MFlux*/s case, which is one of the higher noise floor case amongst the 100-800 *MFlux*/*s* testing conditions. This will allow readers to understand the characteristics of the noise present in relatively higher frequency writing conditions. From the Figure 4-14, one can see how the track edge regions affect the *TAA* and the filtered read-back signal. A red line is drawn to highlight the expected *TAA* level at the track center region where there are minimal noise interferences. The region where the *TAA* plot deviates from the ideal red line will signify the start of the region where the influences from track edge effects come in. From the normalized filtered signal, it is observed that these track edge effects occur when the signal is about 60-70 % of the maximum detected signal. These values also suggest that if the read head is at that position it will be reading 30-40 % of the track edge noise. From the plot, it is observed that as the read head proceeds further into the track edge noise region, the *TAA* increases and experience rather characteristic protruding peaks, ***a***, ***b***, before it drops down to the background *TAA* level, This peak occurs when the read head is still able to pick up 20 % of track signal despite already in the track edge region. If the individual peaks, ***a*** and ***b*** are normalized with the background *TAA* as the base, then the width of the erasure bands can be determined from the 50 % width. By drawing the green line to connect the two *TAA* peaks, it can be observed that the writer width is approximately 125 *nm* which is actually comparable to the *SEM* profile of the writer used.

Next, let’s look at the 3*D* profiles of the frequency spectrum of the 600 *MFlux*/s case where the track is scanned through in the cross-track direction and the data averaged 100 times per location before retrieving the data. The data is then plotted in Figure 4-15.

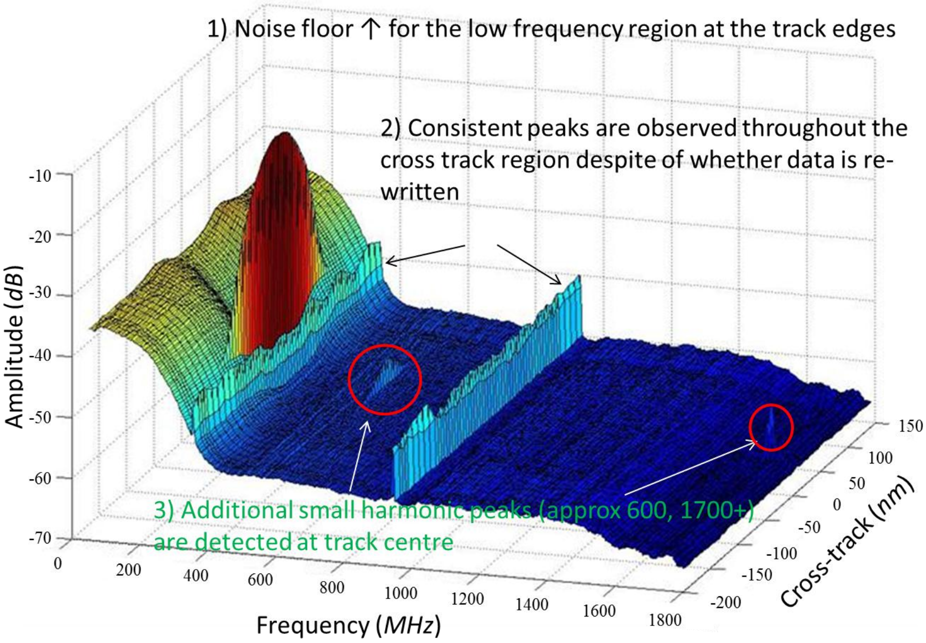

Figure 4 - 15: 100 revolution averaged spectrum data across the cross-track

What was noticed is that at the low frequency region the noise floor is noticeably higher as compared to the other regions; this could be due to the background *DC* grounding noise, the thermal noise and also related to the 90 *rps* spinning speed of the media disc. At track edges, the noise floor is also noticeably higher especially at the low frequency regions, which suggests that the energy of the writing is affecting the grains especially at the track edges such that they will exhibit low frequency vibrations and flux reversals.

Harmonics of the written frequency could be detected only at the track center region which is as expected of. What is interesting is that consistent peaks are observed across the cross track of the written track which its amplitude appears to be independent of the written frequency. These peaks as shown in previous figures are also observable at other written frequencies, which couldn’t be explained by the rotation speed of the spindle, nor the written frequency. One possible explanation is that it is a media characteristic or due to the system setup characteristic as it is independent of the written frequency and the spindle speed.

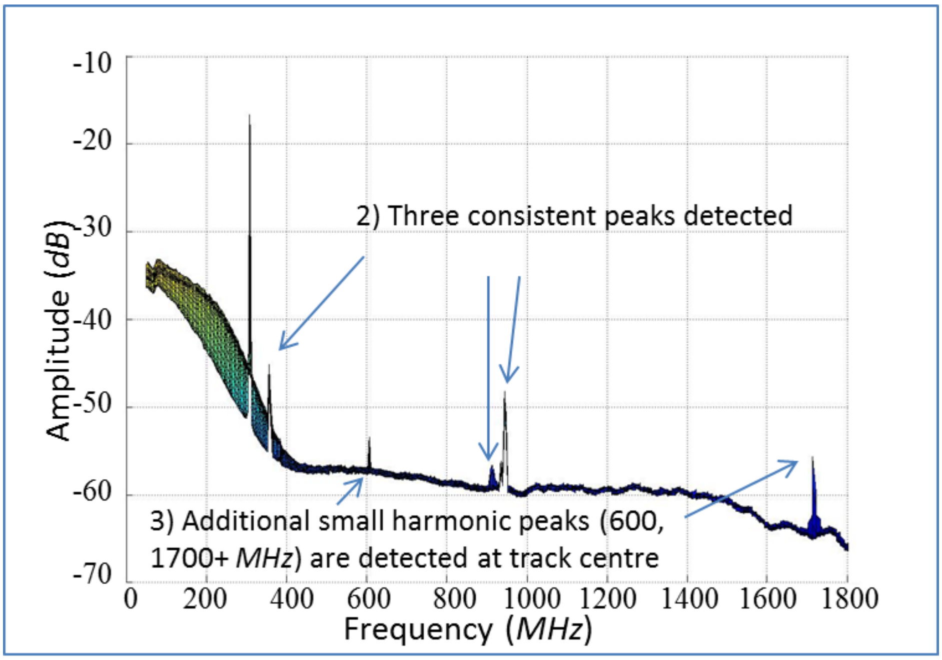

Figure 4 - 16: Amplitude against frequency view of the cross-track spectrum profile

Figure 4-16 illustrates the characteristic of the consolidated cross-track spectrum of the 600 *MFlux/s* recording. In Figure 4-17, the cross track profile can show the amplitude of the written frequency and also the regions at which the track edge effect overshadows the written frequency. In Figure 4-18, the top profile also paints a similar picture.

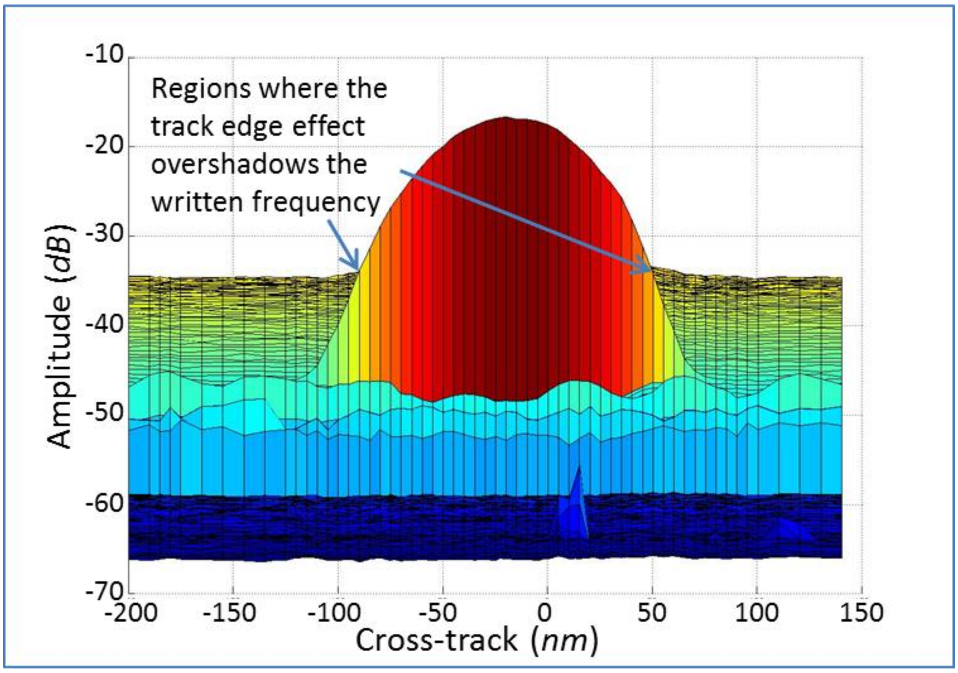

Figure 4 - 17: Cross-track profile view of the spectrum data

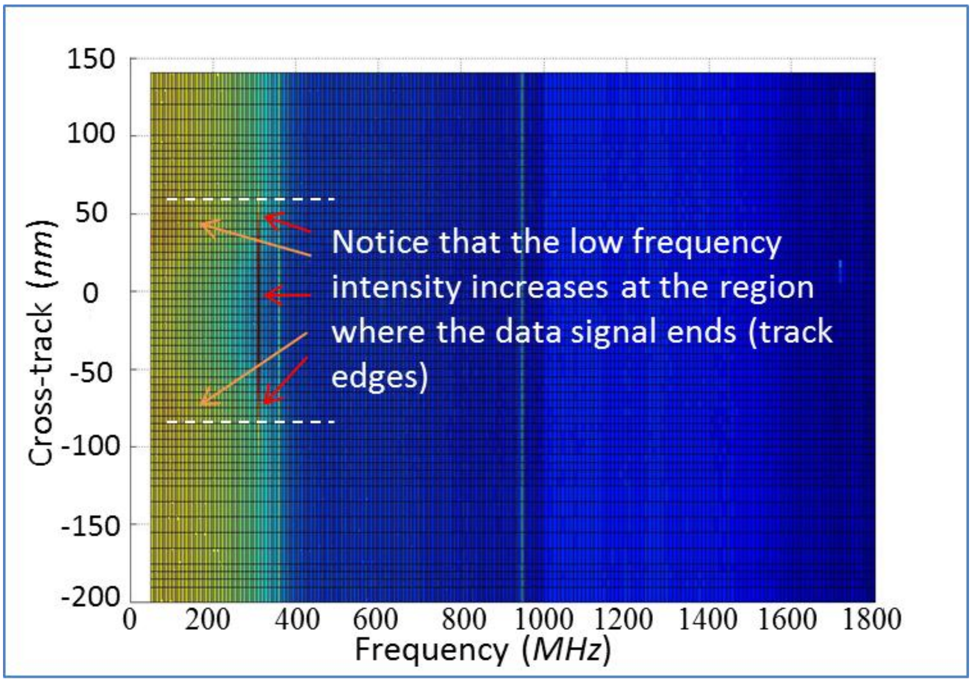

Figure 4 - 18: Top down profile view of the spectrum data

From the 3*D* views in Figures 4-19 and 4-20, it is noticed that the detected read-back frequency is not as what was desired. Instead of detecting 300 *MHz* peak, the detected peak is located 5-10 *MHz* away from the written frequency. A few explanations are that there could be a consistent discrepancy in the written setup and in the spindle speed.

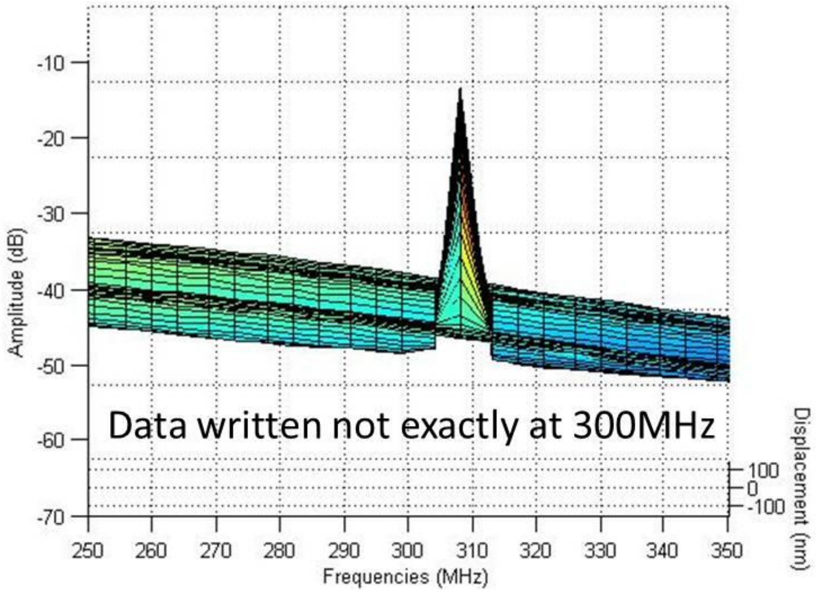

Figure 4 - 19: 3*D* view 1 of data frequency peak

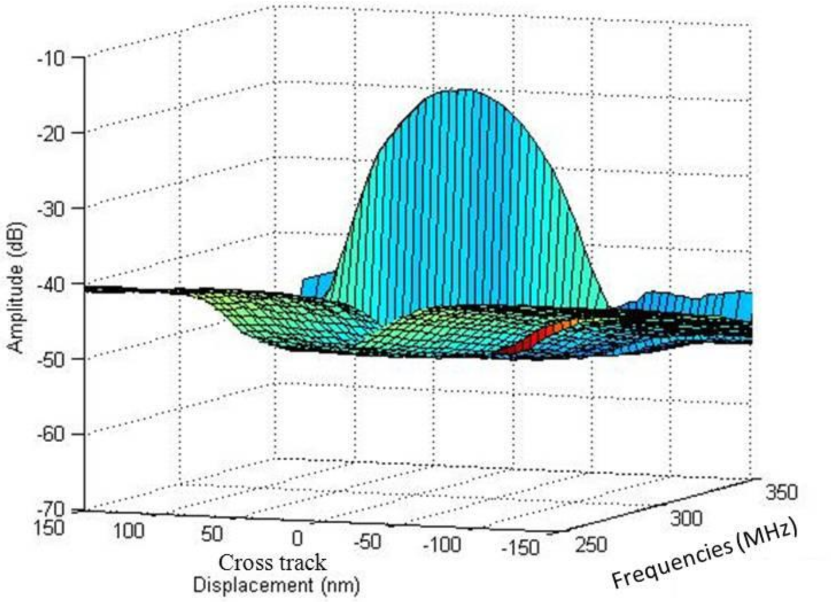

Figure 4 - 20: 3*D* view 2 of data frequency peak

From the 3*D* views (Figures 4-19, 4-20, 4-21), it is observed that the track center exhibits the best writing such that it has a low noise region at the low frequency area and best written amplitude at the desired written frequency; whereas the track edges are more difficult to define as it is a span of region where the desired written frequency drops and the noise level increases substantially at the low frequency region.

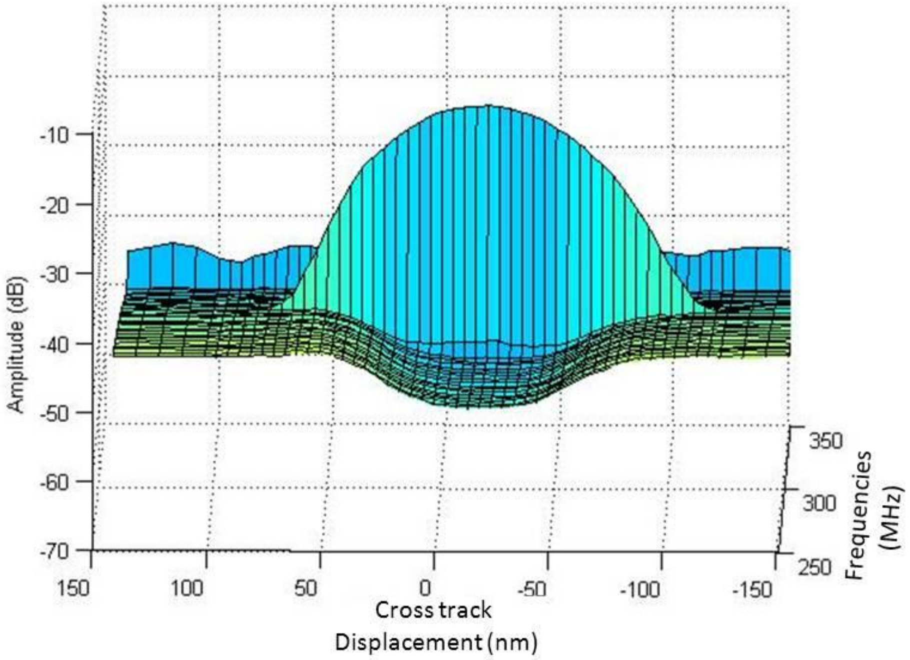

Figure 4 - 21: 3*D* view 3 of data frequency peak

The frequency spectrum is next separated into its individual frequencies to observe for any trends at their single detected frequencies. The results are plotted in Figure 4-22. In general, it is observed that for the writer used, there is a higher tendency for the positive track edge to generate more track edge erasure noise as compared to the negative track edge. Also, even though the written frequency is fixed at 300 *MHz*, it is noticed that the background detected noise floor has a general decreasing trend with an observed increase in the writer width, and decreased track edge noise at higher frequencies. This suggests that at this particular 300 *MHz* writing frequency case, the writer and system setup introduces more noise to the lower frequencies as compared to the higher frequencies. To improve the writing/reading performance of the system, a filter could be used to filter off the noisy low frequencies.

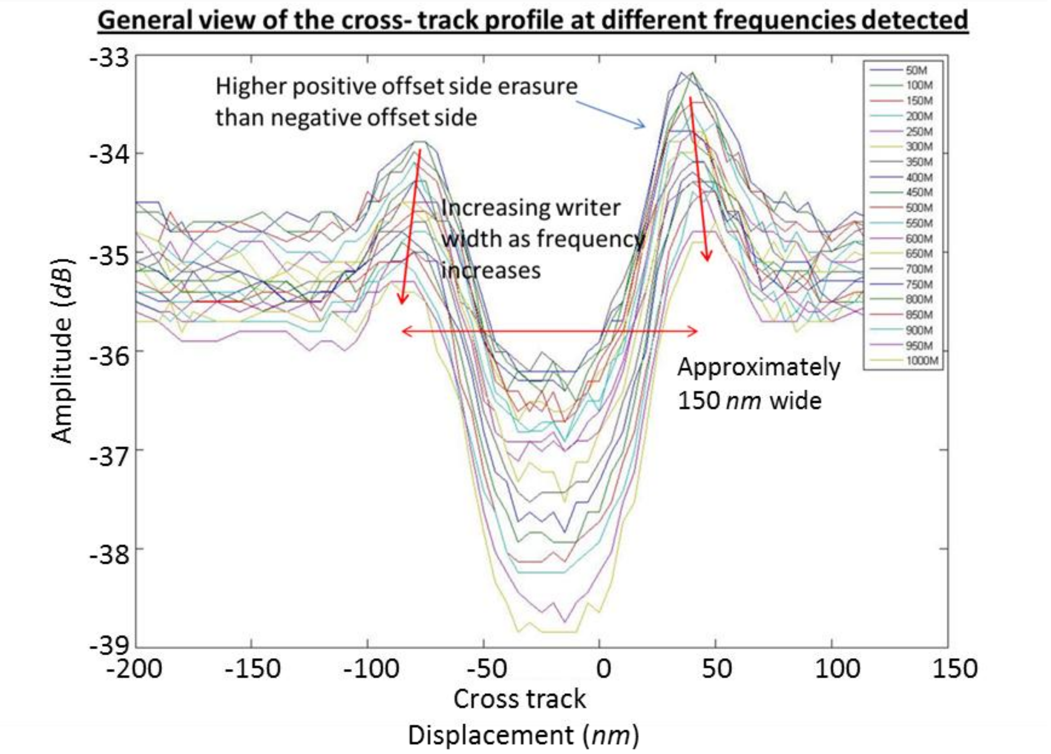

Figure 4 - 22: Dissection of the written 300 *MHz* spectrum into its individual detected frequencies

4.3 Conclusions

In this chapter, the track edge erasures occurrence on both conventional and shingled systems was first described. Important areal density tests, the *BER* and 747 tests, which help to determine the performance and potential areal density of the head-media combination, were subsequently described.

The chapter then proceeded to looked at the writing performance of a particular head, media combination. The writing performance of a particular commercial 250 *Gb*/platter write/read head and a commercial 375 *Gb*/platter media both in the time domain in terms of *TAA* and the spectral domain where data is captured using a spectrum analyzer; have been looked at. The experiments have all been conducted using the commercial Guzik *DTR*3004 spinstand.

TAA results have shown that at the track center region, the *TAA* will decrease due to the increasing ISIs. “Negative” *TAA* was also observed above 600 *MFlux*/*s* recording such that the *TAA* drops below the background noise due to combination effects of the single track writing, the influence of more *ISI*s due to the higher frequency written. Despite the “negative” *TAA* trend observed, the spectrum data revealed that the data peak was still detected and was observed to decrease in power as the written data frequency was increased. Systemic frequency peaks detected however were observed having similar strengths despite the increase in written data frequency. These peaks were thus hypothesized to account for the unique trends observed in the increase and decrease of *TAA*s when the written data frequency was changed.

Written data frequency of 600 *MFlux*/*s* was then specially selected to be investigated in detail. 3*D* data read-back across the track were plotted and revealed that the systemic frequency peaks were found across the tracks. Written data was best written at the track center where the detected frequency power is the highest. Track edge noise regions were observed at the track edges where the data frequency power dips below the systemic noise. In the setup, low frequency noise is highly prominent and a low frequency filter was recommended to improve the performance of the system.

In the next chapter, the described 747 tests and determined areal density values shall be conducted and determined where both the conventional and shingled writing schemes will be compared. The results will thus show the track edge noise’s impact to *BER* and *OTRC* between the two schemes.

Chapter 5: Shingled magnetic recording and its areal density gain

5.1 Introduction

In the previous chapter, the track edge noise at different frequencies and a selected case of 600 *MFlux*/*s* were looked into using both the time domain and frequency domain. In this chapter, the shingled magnetic recording scheme shall be studied.

One of the ways to increase recording density is to reduce the track width of the recorded tracks, thereby increasing the track density and thus increasing the areal density. It is possible to do so by designing side shields to be located nearer the writer head and to have a smaller writer main pole width. However, doing so will significantly reduce the effective magnetic writing field for the head to magnetize the media.

Shingled magnetic recording, on the other hand, is proposed to be one of the potential technologies to continue the areal density growth of hard disks. Shingled recording requires the usage of wide heads to record sequentially from a system designed single cross-track direction. This method of recording requires the wide head to be designed with a large wide side shield on one edge, while totally removing the other side shield. Stronger magnetic field could thus be produced which in turn allows higher anisotropy, smaller grain size yet thermally stable magnetic granular media to be used. In addition, due to the sequential overlapping way of writing the adjacent tracks, the tracks are subjected to only 1 single sided track edge erasure effect as compared to the conventional recording system where it is possible for the track to experience double sided squeezing resulting in track edge erasure effects from the both adjacent written tracks.

5.2 Experimental setup and results

5.2.1 Prerequisites

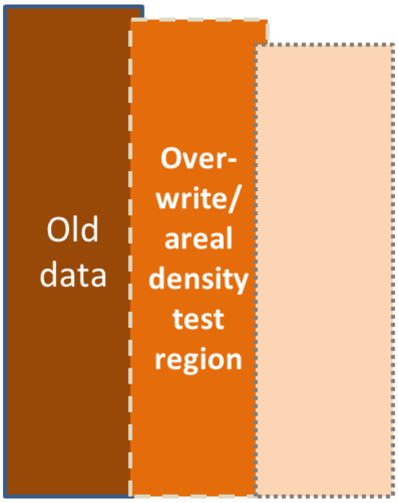

Figure 5 - 1: Illustration of the written shingled test scheme

In the experiment, 3 tracks are written onto the media in a shingled way as illustrated in Figure 5-1. The parameters are then measured only on the center track. Important parameters measured are the overwrite ratio, reverse overwrite ratio, the *SNR*, and *BER*.

The overwrite ratio is one of the important hard disk parameters normally used to determine the writing capability of the head and media. The experiment will first write a single track of a lower frequency data (13*T*). 13*T* data could be understood as data having a period of 13 times the written frequency. A filter which detects the amplitude of the target frequency is then used to measure the spectral amplitude of the written data, in this case the low frequency data (13*T*). After which, the track will be overwritten with a higher frequency data (2*T*), and the filter is again used to detect the resultant amplitude of the 13*T* data after being overwritten. The ratio of before overwritten amplitude divided by after written amplitude is known as overwrite ratio (Equation 5-1). An illustration of the process is shown below in Figure 5-2.

$$Overwrite\ ratio = \frac{spectral\ amplitude\ of\ 13T\ data}{spectral\ amplitude\ of\ 13T\ data\ after\ overwritten\ with\ 2T\ data}$$

(5 - 1)

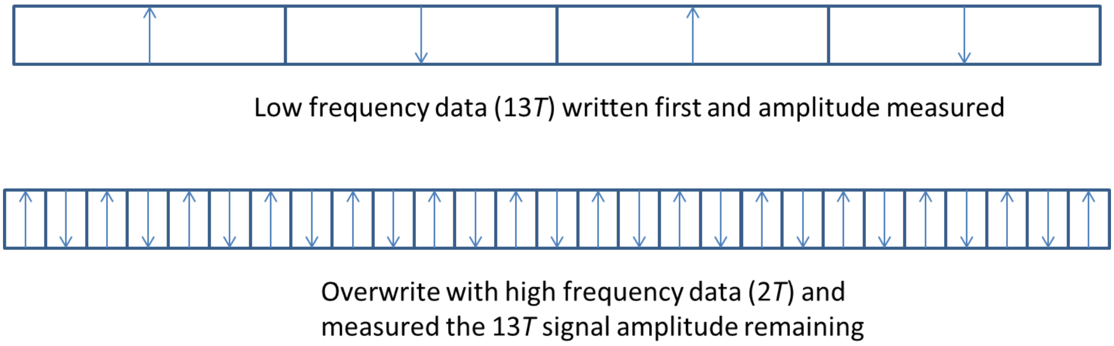

Figure 5 - 2: Illustration of the overwrite ratio test

It is suggested that poor overwrite ratio exists at regions where the writing current is not enough to magnetize or saturate the media properly, regions at track edges and regions where the cross-track head field gradient is low. In addition, imprint effect from the background low frequency data could cause non-linear transition shifts (*NLTS*) and undesired modulation to the incoming data signal especially at regions where the recording field is weak namely the track edges of the head field. A typical effect of poor overwrite is that additional harmonics of frequency sidebands about the written frequency could be detected when viewed via spectrum analyzer. [76]

Similar in concept, reverse overwrite ratio is the situation where the high frequency (2*T*) is measured and subsequently overwritten with a low frequency data (13*T*). An illustration of the reverse overwrite process is shown in Figure 5-3. The equation 5-2 is also as shown below.

$$\text{Reverse overwrite ratio} = \frac{\text{spectral amplitude of } 2T \text{ data}}{\text{spectral amplitude of } 2T \text{ data after overwritten with } 13T \text{ data}}$$

(5 - 2)

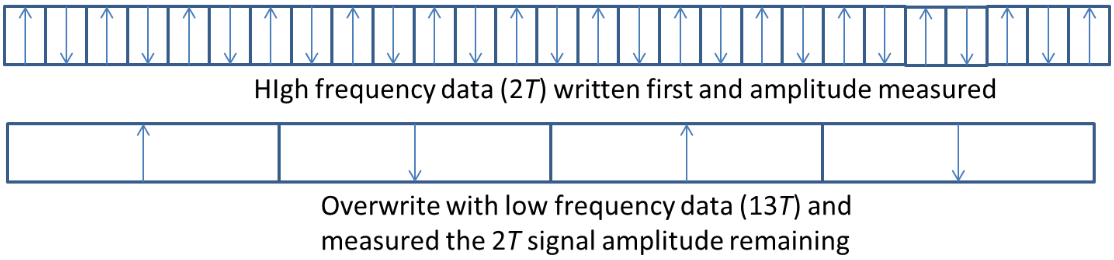

Figure 5 - 3: Illustration of the reverse overwrite ratio test

The background high frequency data before being overwritten could cause a modulation effect to the incoming low frequency data. This effect would be more prominent at track edge areas where the writing field is not strong enough to fully switch the grains, center region of the similarly-oriented magnetic grains where the strong demagnetization field would be coupled with the background high frequency field thus greatly counteracting the incoming low frequency writing field. Therefore, it is essential that in magnetic recording, both overwrite and reverse overwrite ratios should be of relatively high values (>20 *dB*) to ensure good writing at room temperature operating conditions.

Before further tests are conducted, the triple track tests are used to derive the *MWW* [77], whereas the micro-track method is used to derive the magnetic read width (*MRW*). In this experiment, the *MWW* is 75 *nm* while the *MRW* is 57 *nm*. The triple track method goes in 3 basic steps: 1) Write a single frequency, *f*1 on the track, 2) Overwrite *f*1 track with another frequency, *f*2 and ensure the *f*1 track is squeezed, 3) Overwrite the squeezed *f*1 track with the *f*1 track and ensure that the *f*1 track lies within the two *f*2 tracks. The illustration of the process is shown below in Figure 5-4.

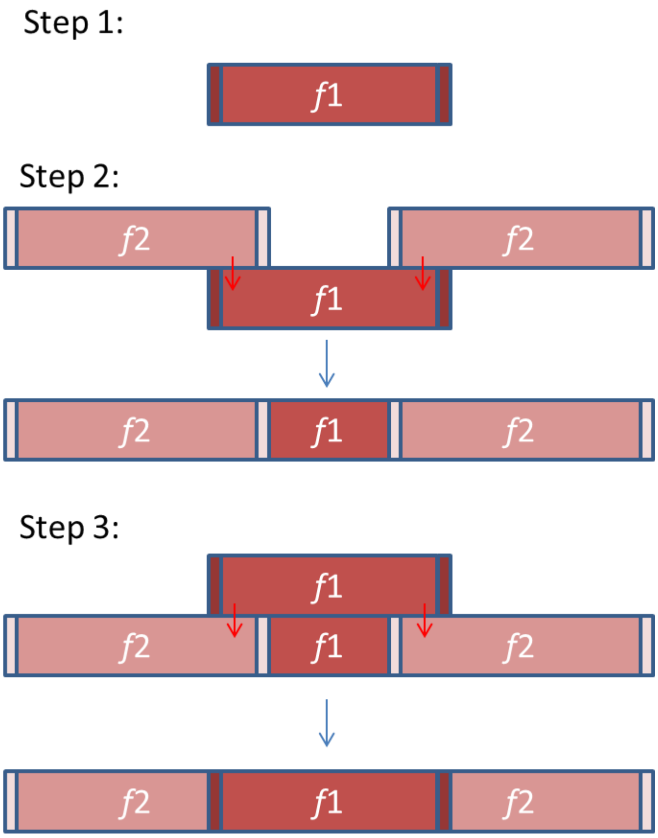

Figure 5 - 4: Illustration of the triple track test to derive the erasure bands

After the tracks have been written, do track profile scans using the overwrite filter to retrieve back the *f*1 profile as well as the *f*2 profiles. Normalised the read-back profiles and three parameters namely the written track width, the left erase band width and the right erase band width could be derived. The erase band region could be found where the gap exists at the 50 % amplitude of the normalised *f*1 and *f*2 profile. The processed experimental results illustrating the erasure bands is shown below in Figure 5-5.

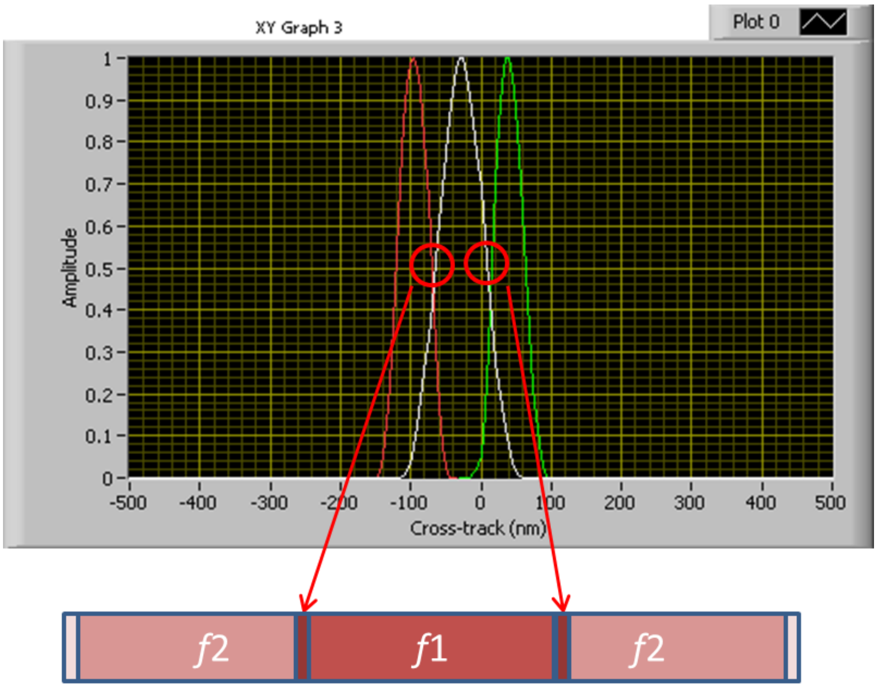

Figure 5 - 5: Illustration of the erasure bands from the center data track

As for the *MRW*, the typical method is to use the micro-track scheme as illustrated in Figure 5-6. The initial steps are similar to the triple track method. The only thing to take note is that the *f*1 track is not rewritten and the remaining *f*1 track width should be smaller than the expected *MRW* and approximately having a track profile peak of 10 % amplitude of the full track width profile. With this experimental setup, the track profile could then be conducted again and the *MRW* is determined from the 50 % amplitude of the track profile.

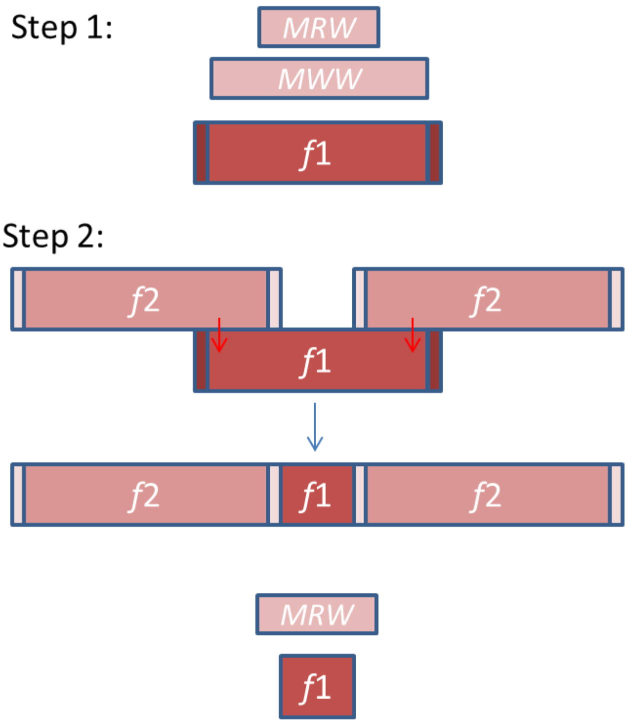

Figure 5 - 6: Illustration of the write/read test to derive the magnetic read width (*MRW*) of the reader

5.2.2 Experimental parameters

In the experimental setup, the test is conducted at the *MD* region, 22 *mm*. The media and spindle is rotating at the speed of 5400 *rpm*. Thermal fly-height control (*TFC*) is used to ensure the fly height of ~5 *nm* above the media. A list of Guzik parameters used during the experiments is tabulated in the table 5-1.

Parameters	**Values**
Radial location, *r* (*mm*)	22
Spindle speed, *s* (*rpm*)	5400
Write current (*mA*)	50
Read bias (*mV*)	140
Overshoot (*%*)	50
Overshoot duration (*ps*)	300
***TFC* write (*mW*)**	80
***TFC* read (*mW*)**	70
Sector control mode	Positive
No of sectors	100
Sector frequency calibration (*MHz*)	50
***AC* erasure frequency (*MFlux/s*)**	1200
Data rate, *f*	900 *MFlux/s* or 1837 *kFCI*

Table 5 - 1: Experimental parameters for the shingled and conventional write/read tests

Based on the above parameters tabulated in table 5-1, the linear density of the data track can be derived. With the radial location, r and revolution speed, s of the media, with s having the unit rounds per minute, the velocity, v of the media at the written location can be calculated using equation 5-3. With the written frequency, f, the bit length, bl of the written data track can be found. The bit length, bl can then be used to determine the linear density, ld, which will have the units of kilo flux change or bits per *inch* (*kFCI* or *kBPI*) (Equation 5-4, 5-5). By knowing track pitch, tp of the tracks, the track density in *kilo* tracks per *inch* (*kTPI*) could be found (Equation 5-6). Multiplying both the ld and td would yield the areal density, ad which has the units of kilo-bits per square *inch* (*kbpsi*) (Equation 5-7).

$$\text{Velocity}, v = \frac{2 * PI * r * s}{60}$$

(5 - 3)

$$\text{Bit length}, bl = \frac{\mathrm{v}}{f}$$

(5 - 4)

$$\text{Linear density}, ld = \frac{25.4}{bl * 10^{-3}}$$

(5 - 5)

$$\text{Track density}, td = \frac{25.4}{tp * 10^{-3}}$$

(5 - 6)

$$\text{Areal density}, ad = \text{Linear density}, ld * \text{Track density}, td$$

(5 - 7)

5.2.3 Experimental results

5.2.3.1 *TAA* and read-back track width after *AC* track erasure

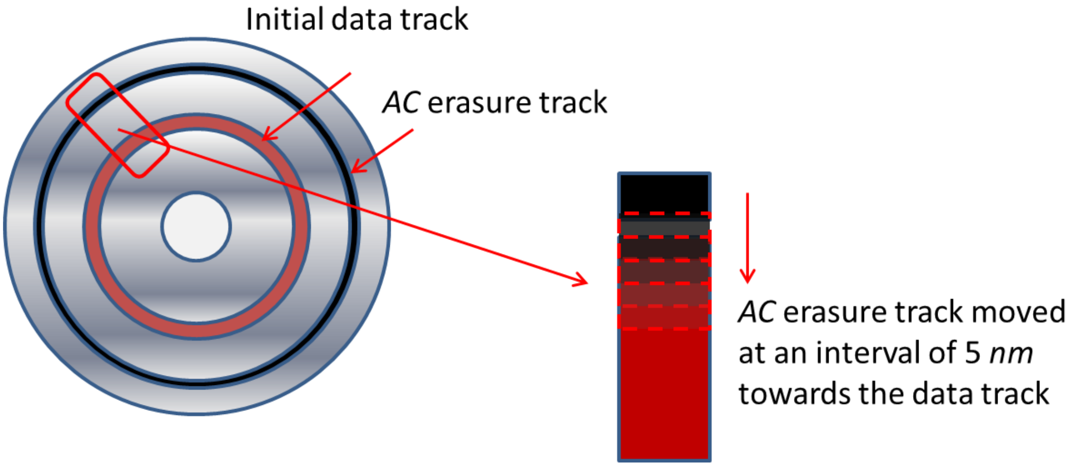

Figure 5 - 7: Illustration of the process of squeezing the data track using the *AC* erasure track

A typical squeeze of the tracks is shown in Figure 5-7. The *AC* erasure track is continually moved from an offset of 110 *nm* to 5 *nm* at 5 *nm* interval towards the center data track. At each interval, after the *AC* erasure track is written, the track profile using an overwrite filter is done across the cross track direction to retrieve the *TAA* profile.

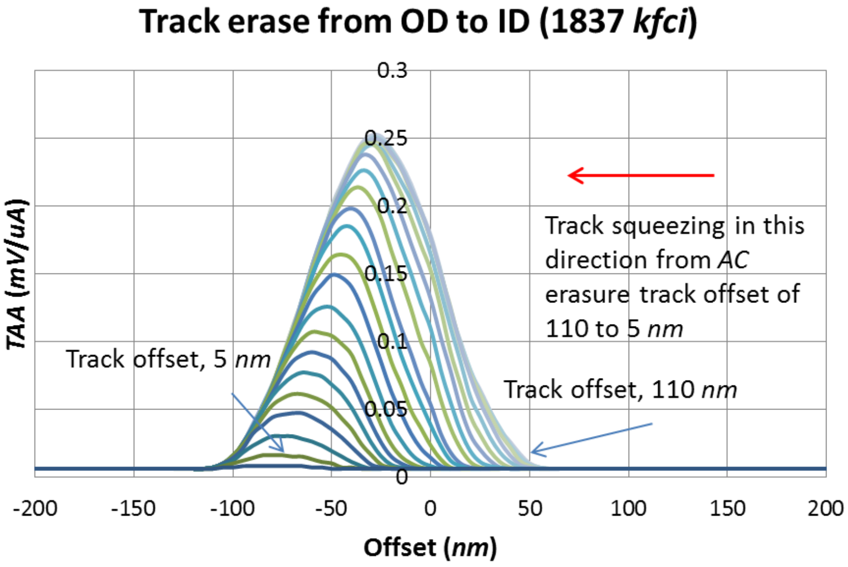

Figure 5 - 8: Experimental results of the squeezing effect on the read-back *TAA* after track squeezing from the positive offset at linear density of 1837 *kFCI*

Figure 5-8 shows that as the data track is squeezed with the *AC* erased track, the reader picks up lesser width of the data frequency thus the data amplitude decreases significantly as the *AC* erased track eats into the data track. It is observed that even though the *AC* erasure track is moved at 5 *nm* interval, the experimentally derived track width profile did not move at the expected value of 5 *nm*. Instead, probably due to the minute spindle fluctuation, and thus non-circular *AC* erasure condition, the interval change fluctuates about 1-4 *nm*. Despite the systemic experimental errors, these set of experimental results is still valid as the general trend is still consistent, such that the experimentally calculated track width is of a downward trend.

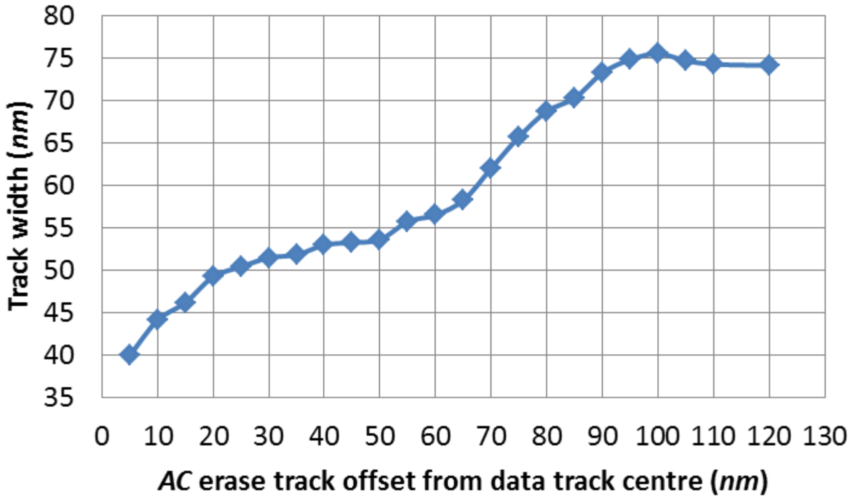

Figure 5 - 9: Experimentally derived track width versus track squeeze plot

Figure 5-9 is derived by normalizing each set of *TAA* data collected in Figure 5-8. After the data is normalized, the 50 % offset point is retrieved at both the left and the right edges. This width will be the read-back track width of the data track after *AC* erasure and is plotted in Figure 5-9 with its corresponding *AC* erase track offset value. This track width derivation process is illustrated in the Figure 5-10. The track width derived is then used to subtract with the adjacent one to derive the actual individual track erasure value when the *AC* erasure track is shifted 5 *nm* sequentially from the positive offset of 110 to 5 *nm*. These values will give a gauge of how much erasure in actual has been made. These values are collected and plotted in the Figure 5-11. As could be seen, these values differ between 0-4 *nm* which is the expected range to take considering only a maximum offset change of 5 *nm* is made.

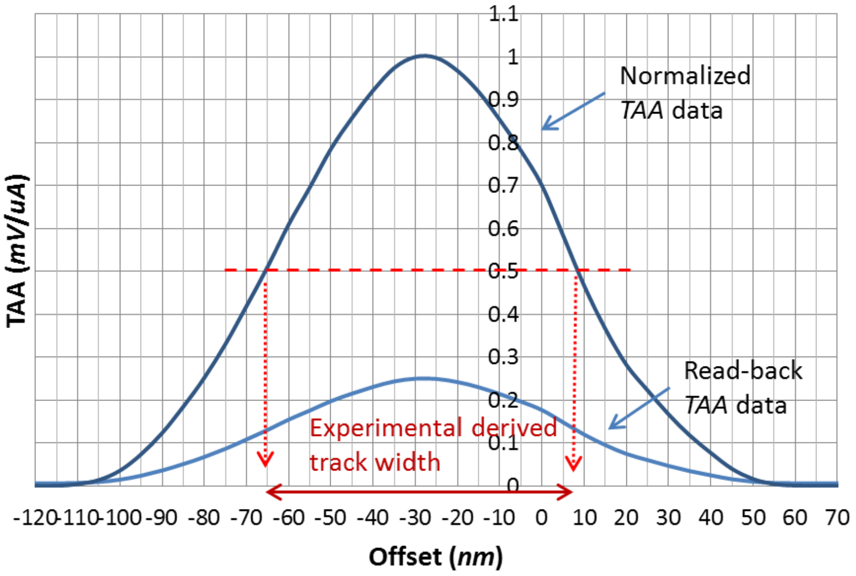

Figure 5 - 10: Illustration of the experimentally derived track width at different *AC* erasure track offset using the corresponding set of read-back *TAA* data

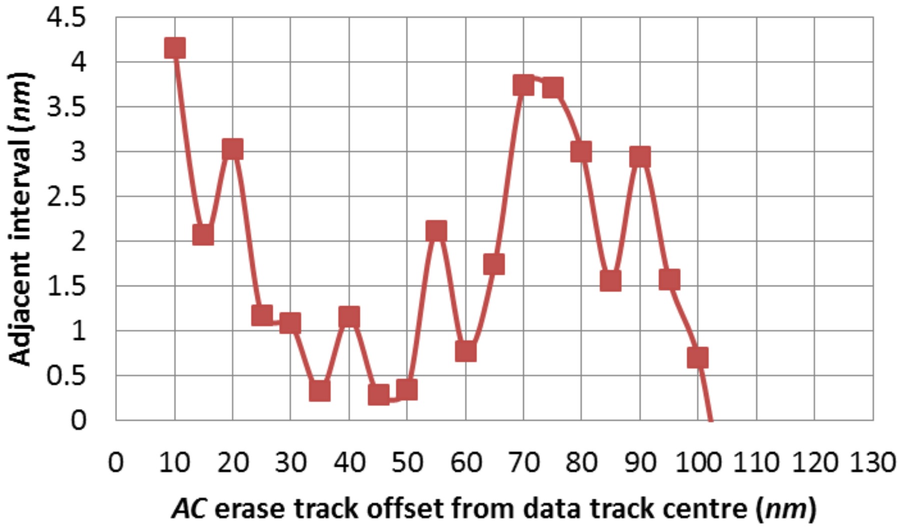

Figure 5 - 11: Actual experimentally derived track erasure values at different *AC* track offset

5.2.3.2 *BER* bathtub test

Next, the M7 Anaconda *BER* error analyzer board, which acts as a *NPML* detector that facilitates complex tests like the *BER* bathtub and 747 is used. The following results will illustrate the *BER* difference as the read head scans through the cross track profile of the above shingled tracks. *MRW* is a critical value here as it determines the read area of the data tracks, which in turns determines the *BER* of the read tracks [2].

The track profile test provided by the M7 Anaconda software is used to do the shingled writing and *BER* test. The screenshot of the configuration is shown in Figure 5-12. A background erase of *AC* 1*T* + Δ(1 % frequency) will be conducted first before each old and center data track write. Subsequently, the adjacent track is slowly shifted from the 110nm offset case to 5nm case. In the setup, the adjacent interfering track is chosen to be the same frequency but with 50 % frequency change of the original data frequency. As an example, if 900 *MFlux/s* is used for the data rate, 900±450 *MFlux/s* will be used as the erasure frequency.

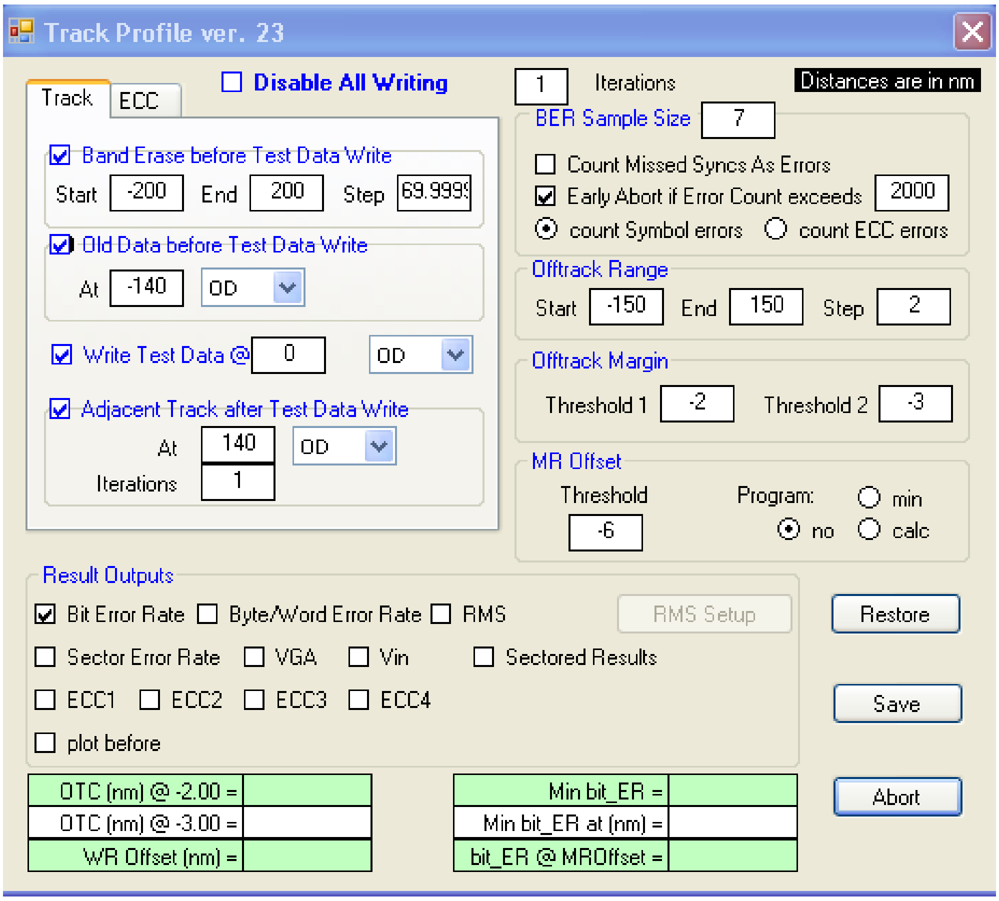

☐ Disable All Writing

1 Iterations

☑ Band Erase before Test Data Write
Start -200 End 200 Step 69.999

☑ Old Data before Test Data Write
At -140 OD

☑ Write Test Data @ 0 OD

☑ Adjacent Track after Test Data Write
At 140 OD
Iterations 1

BER Sample Size 7
☐ Count Missed Syncs As Errors
☑ Early Abort if Error Count exceeds 2000
● count Symbol errors ○ count ECC errors

Offtrack Range
Start -150 End 150 Step 2

Offtrack Margin
Threshold 1 -2 Threshold 2 -3

MR Offset
Threshold -6
Program: ○ min ● no ○ calc

Result Outputs
☑ Bit Error Rate ☐ Byte/Word Error Rate ☐ RMS
☐ Sector Error Rate ☐ VGA ☐ Vin ☐ Sectored Results
☐ ECC1 ☐ ECC2 ☐ ECC3 ☐ ECC4
☐ plot before

OTC (nm) @ -2.00 =
OTC (nm) @ -3.00 =
WR Offset (nm) =
Min bit_ER =
Min bit_ER at (nm) =
bit_ER @ MROffset =

Figure 5 - 12 (a): Anaconda M7 track profile test to conduct the experiment and to retrieve the data points of the *BER* bathtub curve

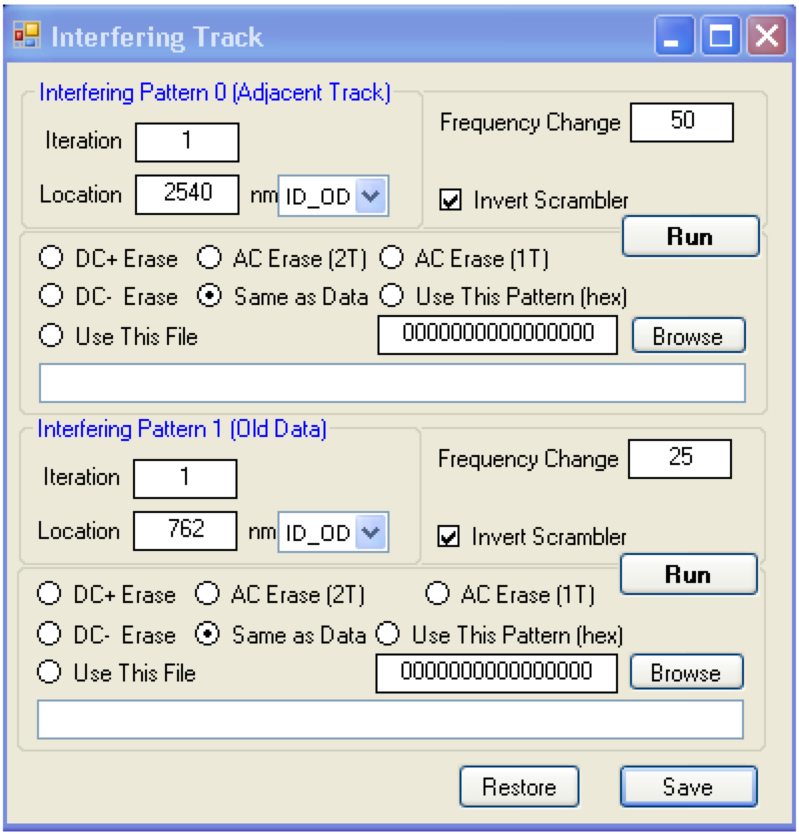

Interfering Track

Interfering Pattern 0 (Adjacent Track)

Iteration 1

Location 2540 nm ID_OD

Frequency Change 50

☑ Invert Scrambler

○ DC+ Erase ○ AC Erase (2T) ○ AC Erase (1T)

○ DC- Erase ● Same as Data ○ Use This Pattern (hex)

○ Use This File 0000000000000000

Interfering Pattern 1 (Old Data)

Iteration 1

Location 762 nm ID_OD

Frequency Change 25

☑ Invert Scrambler

○ DC+ Erase ○ AC Erase (2T) ○ AC Erase (1T)

○ DC- Erase ● Same as Data ○ Use This Pattern (hex)

○ Use This File 0000000000000000

Figure 5 - 12 (b): The configuration setup for the old and interfering tracks

In the *BER* bathtub curves done at linear density of 1837 *kFCI*, the *AC* erasure track is used to squeezed towards the data track from the negative offset at 5 *nm* intervals. It is observed that when the squeezing eats into the data track, the minimum peak for the *BER* shifts further down the cross-track along the same direction of the squeeze. The *BER* will also be poorer due to effects of the erase bands of the *AC* erased track. This effect is especially so in the case when the trimmed track width has been reduced to much smaller than the *MRW*, where the reader will read in much more interferences from both the *AC* track and the erase band and the track edge of the data track. Experiments on three different linear densities have been conducted and the plots are as displayed below in Figures 5-13, 5-14 and 5-15. The observations are that the *BER* becomes poorer due to higher inter-symbol intereferences, erasure issues and thus poorer read-back at higher linear densities.

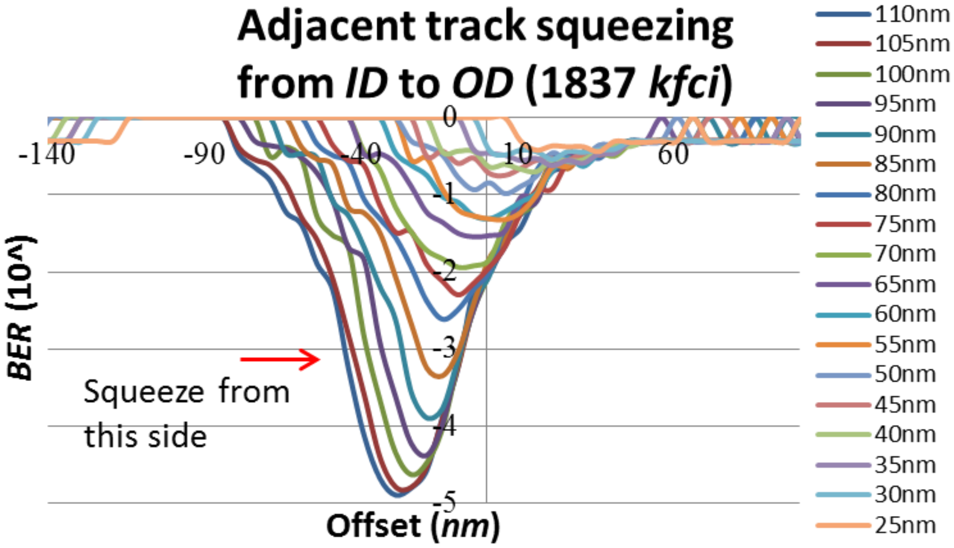

Figure 5 - 13: *BER* bathtub curve for single side track squeeze at linear density of 1837 *kFCI*

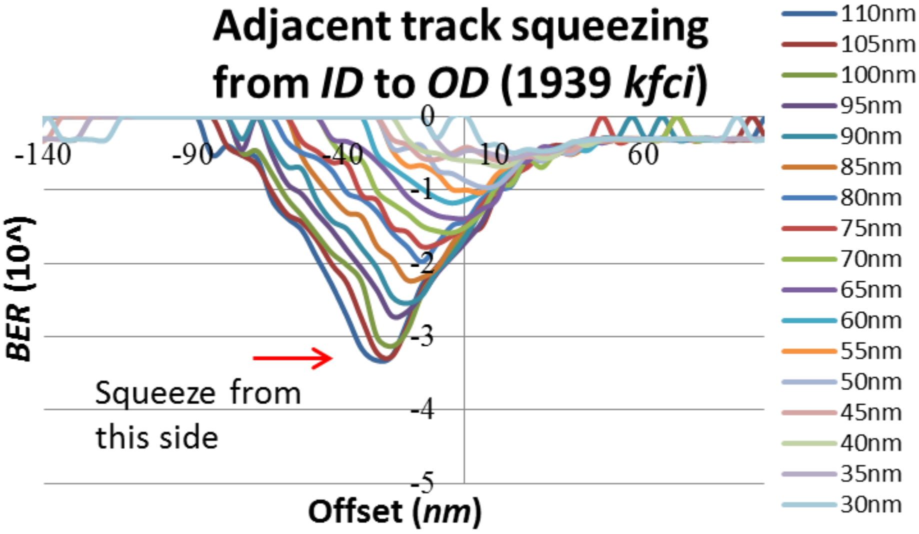

Figure 5 - 14: *BER* bathtub curve for single side track squeeze at linear density of 1939 *kFCI*

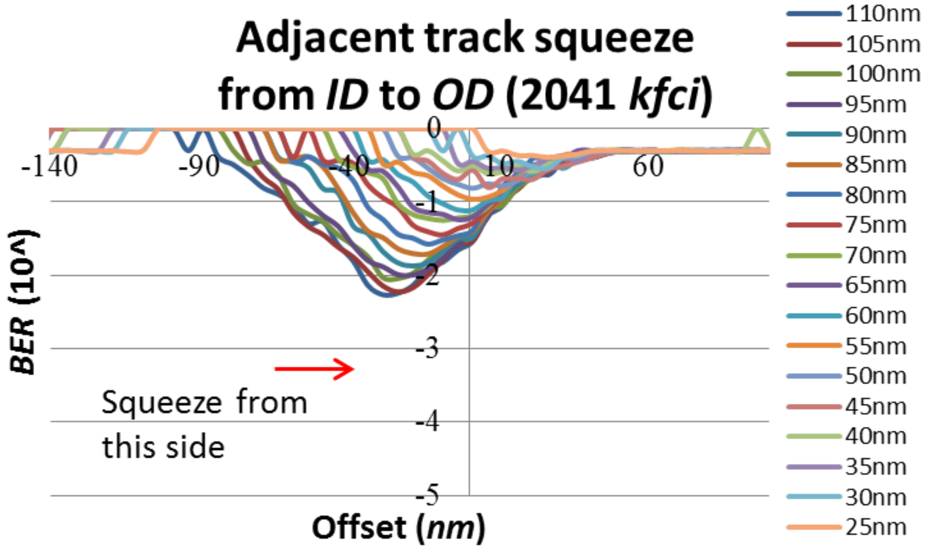

Figure 5 - 15: *BER* bathtub curve for single side track squeeze at linear density of 2041 *kFCI*

From Figures 5-13, 5-14, 5-15, let's look at the on-track *BER* depth, which is the minimum *BER* detected at the 3 different linear densities, to observe the rate of decline at the similar squeezing rate and to observe the relationship to *MRW*. This minimum *BER* values are retrieved for each track squeeze at the three different linear densities and then its magnitude are used to plot in Figure 5-16

From the three plotted lines in Figure 5-16, it is observed that initially as the *AC* track is significantly far away from the data track thus not causing much erasure effects to the data track, the rate of decline for the three densities are similar. The divergence in the decline rates occurs when the *AC* track is offset at 95-100 *nm* away from the data track center. The decline rate is highest for the lowest density, 1837 *kFCI* case and lowest for the highest density, 2041 *kFCI* case. The rationale is because at a lower density, the erasure bands from the *AC* track has more impact to the *BER* as compared to the higher density case where more inter-symbol intereferences are already influencing the data track.

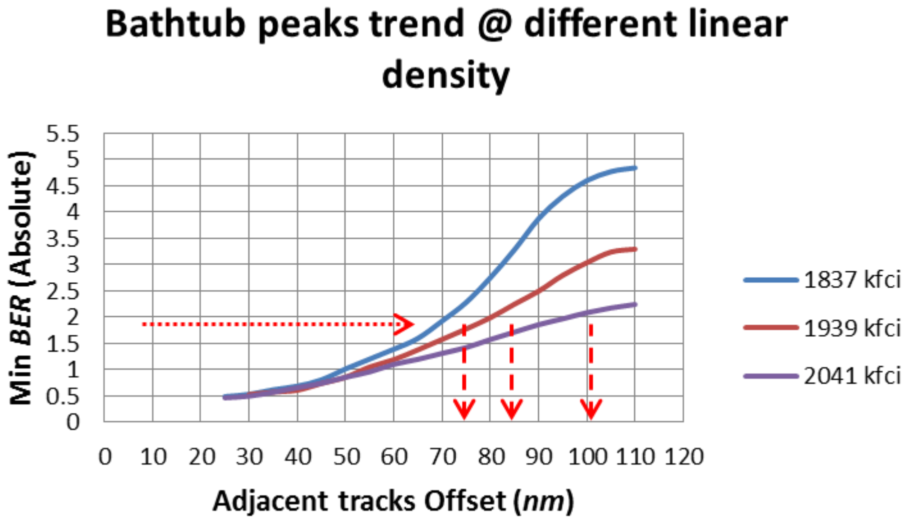

Figure 5 - 16: Plot of the absolute value of the minimum *BER* detected for different linear densities

From the plots, the drop of the *BER* can be determined from the degree of squeezing. For example, at *BER* of 10^{-2}, by drawing a red line on the plot, the tracks can be squeezed cross-track at approximately 70, 80, 100 *nm* interval respectively for the 1837, 1939, 2041 *kFCI* case. Using equation 5-4, the bit lengths can be derived to be 13.8, 13.1 and 12.4 *nm* respectively. Meaning to say, at such squeezing capability, at bit lengths of 13.8, 13.1 and 12.4 *nm*, the acheivable areal density is 666, 615 and 518 *Gbpsi* for a 2.5 *inch* media disc with no channel implemented. Note that if the logic of using the highest linear density for magnetic recording to achieve highest areal density works, the 2041 *kFCI* case would be expected to have the largest areal density. However, this is not so. The 1837 *kFCI* case is actually able to achieve a higher areal density of 666 *Gbpsi*. This shows that there needs to be a balance of high linear and and track density to achieve high areal density at the desired *BER*.

5.2.3.3 Analysis of areal density gain for shingled writing system

The next priority will be to determine the highest areal density possible for this head and media combination for different recording schemes: the conventional and the shingled write. Before this is done, the overwrite tests are conducted first to investigate on the trend of the overwrite profile at different shingled track widths. A WITE32 self-programmed module has been used to conduct the experiments and to sort and retrieve the results. The screenshot of the configuration is shown in Figure 5-17. The *MWW* is a required parameter to be measured and known first before conducting this test. The program will base on the *MWW* and write the adjacent tracks at the positive offset of *MWW* distance and negative offset of *MWW* distance. As illustrated in Figures 5-18, the adjacent tracks will be slowly moved towards the center track to represent the shingled squeeze and the overwrite values will be retrieved by applying the equations 5-1, 5-2 from the highest point amplitude in the track profile test of both normal case and the overwritten case.

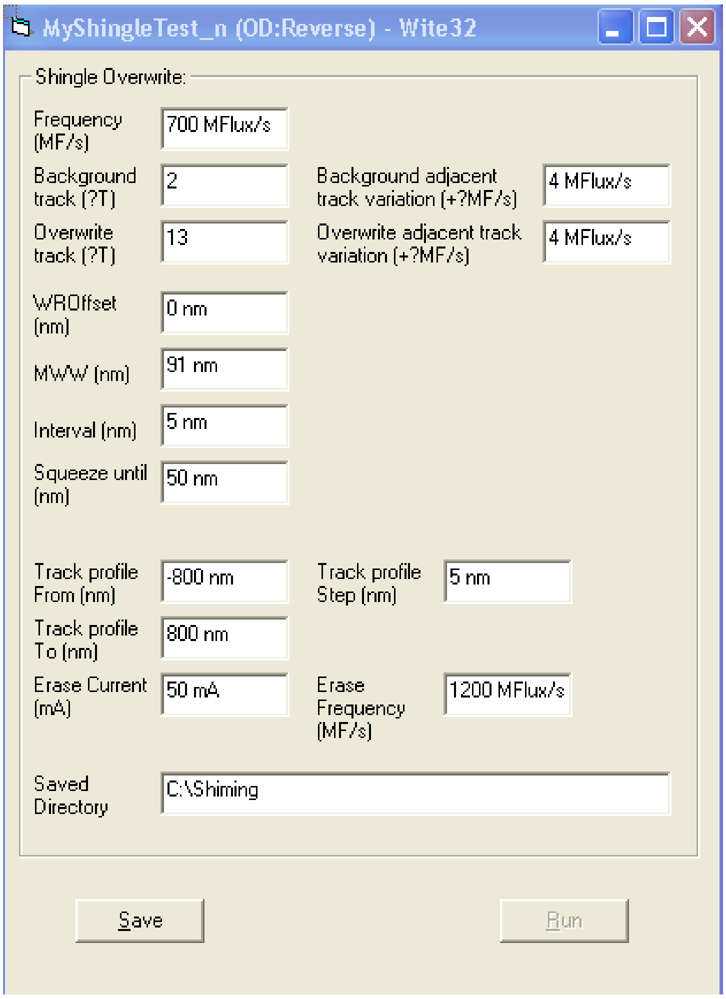

Shingle Overwrite:

Frequency (MF/s): 700 MFlux/s

Background track (?T): 2

Background adjacent track variation (+?MF/s): 4 MFlux/s

Overwrite track (?T): 13

Overwrite adjacent track variation (+?MF/s): 4 MFlux/s

WROffset (nm): 0 nm

MWW (nm): 91 nm

Interval (nm): 5 nm

Squeeze until (nm): 50 nm

Track profile From (nm): -800 nm

Track profile Step (nm): 5 nm

Track profile To (nm): 800 nm

Erase Current (mA): 50 mA

Erase Frequency (MF/s): 1200 MFlux/s

Saved Directory: C:\Shiming

Figure 5 - 17: Screenshot of the shingled overwrite test setup

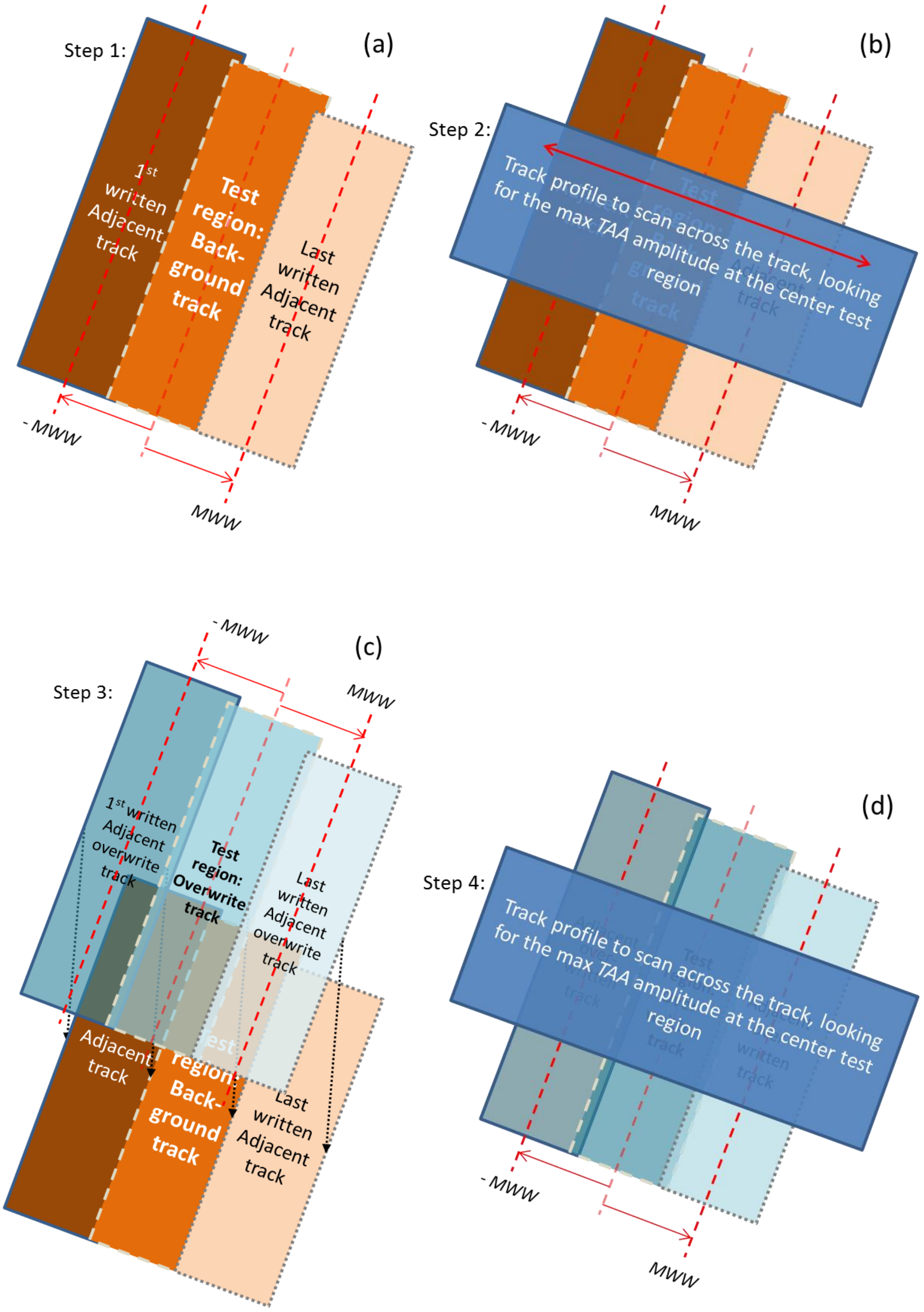

Figure 5 - 18 (a): Step 1 of shingled write overwrite test

Figure 5 - 18 (b): Step 2 of shingled write overwrite test

Figure 5 - 18 (c): Step 3 of shingled write overwrite test

Figure 5 - 18 (d): Step 4 of shingled write overwrite test

The different overwrite ratios conducted at different linear densities and different track squeezing are plotted in Figure 5-19. For the overwrite ratios, the range spans from 40-53 *dB* and as the linear density increases, which implies more squeezing of the tracks, the overwrite ratios also decrease. As for the reverse overwrite ratio, the range spans from 33-57 *dB*. Typically, overwrite and reverse overwrite ratios are considered good if the ratios are more than 20 *dB*. It is noticed that the trends of overwrite and reverse overwrite ratios for the different linear densities appear similar. However, a minute difference could be observed such that at low track squeezing, high linear density systems tend to perform poorer than low linear density ones. However at high track squeezing, the trend is opposite, high linear density systems tend to perform better in the ratios compared to the low linear density ones.

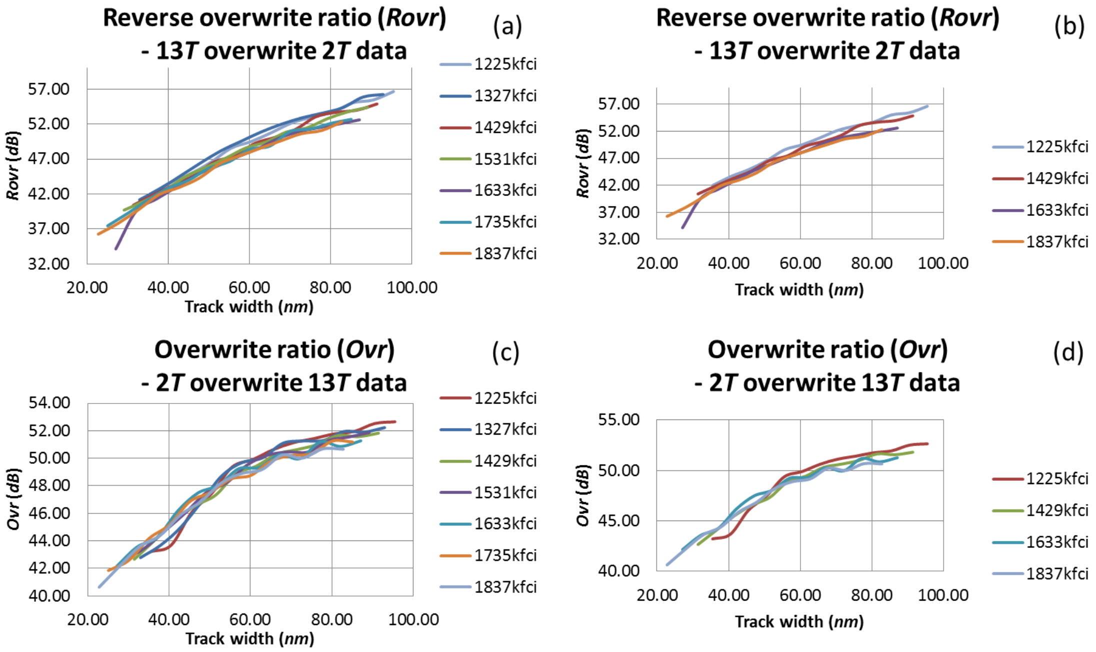

Figure 5 - 19 (a): Reverse overwrite ratio of 13*T* signal overwriting the 2*T* data at different shingled track squeeze at different linear densities

Figure 5 - 19 (b): Reverse overwrite ratio of 13*T* signal overwriting the 2*T* data at different shingled track squeeze for selected linear densities of 1225, 1429, 1633, 1837 *kFCI*

Figure 5 - 19 (c): Overwrite ratio of 2*T* signal overwriting the 13*T* data at different shingled track squeeze at different linear densities

Figure 5 - 19 (d): Overwrite ratio of 2*T* signal overwriting the 13*T* data at different shingled track squeeze for selected linear densities of 1225, 1429, 1633, 1837 *kFCI*

In Figure 5-20, the *MWW*, *MRW* using the data retrieved from the standard track profile test of the Guzik spin-stand is plotted. It is noticed that at higher linear densities, the *MWW* is observed to decrease by 14 %, around 14 *nm* when there is an increase of 50 % in linear density from 1200 to 1800 *kBPI*. This decrease in the *MWW* at higher densities is expected when there is more *ISI*s. This decrease in the *MWW* however is not the key reason why the reverse overwrite and overwrite ratios appear to be better for higher linear densities as compared to lower linear densities, considering that for both cases, the shingled track width are similar. One of the possible reasons is that for the lower linear density case, lower linear density tracks are used to shingle and thus introduces stronger track erasure effects to the center track as compared to the higher density case. As a result, the initial data read-back after writing the shingled tracks is relatively poorer at low density as compared to high density ones.

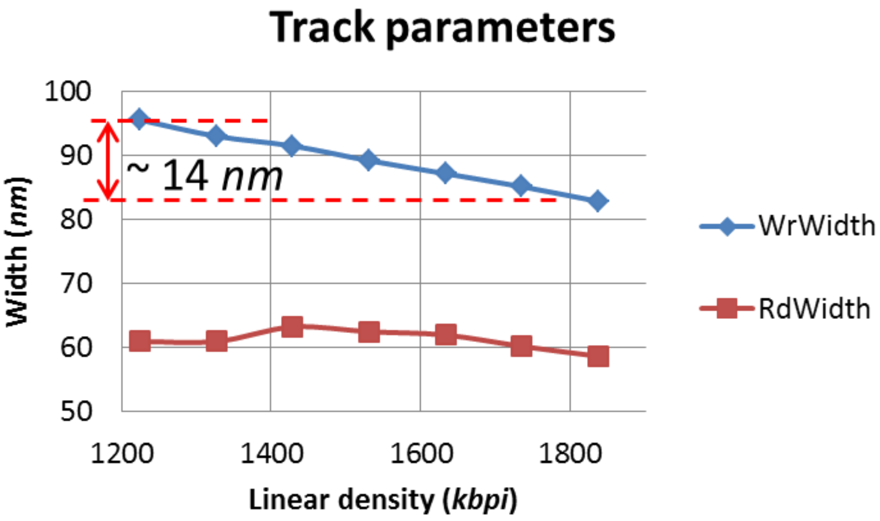

Figure 5 - 20: Plot of the track paramters namely *MWW* and *MRW* retrieved for different written linear densities

For each linear density, all the *BER* peaks are first collected at different adjacent track squeeze. Then the curves for each linear density are plotted together in Figure 5-21. This method of plotting and sorting of data allows the users to know the trend of the *BER* against the linear densities and also the trend of the *BER* at different adjacent track squeeze.

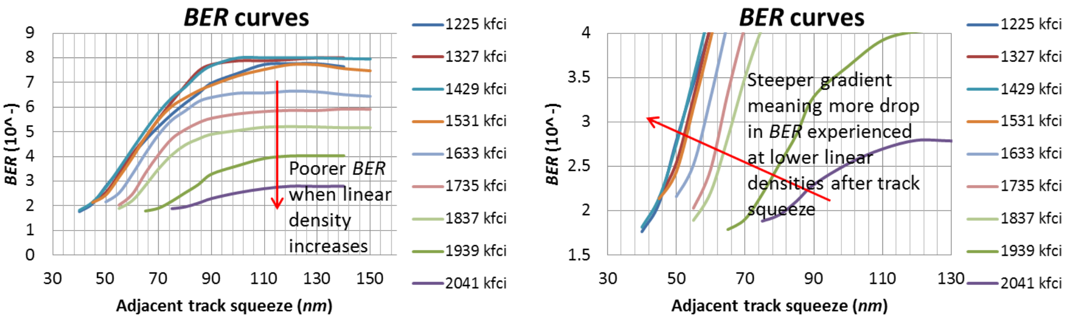

Figure 5 - 21 (a): *BER* trends for different linear densities

Figure 5 - 21 (b): Zoomed in view of the *BER* trends for different linear densities

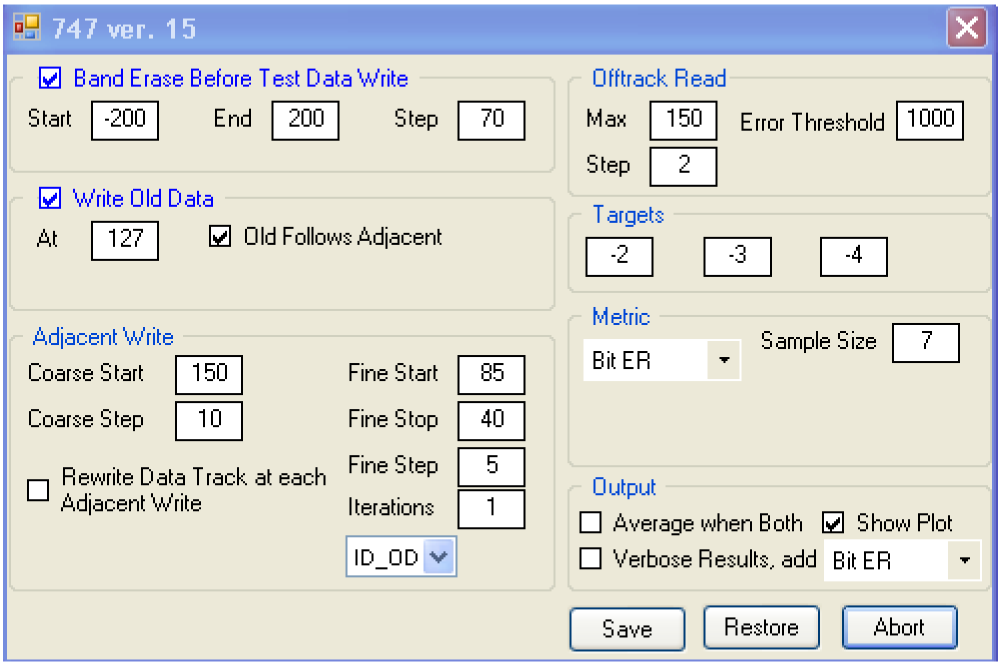

747 ver. 15

☑ Band Erase Before Test Data Write
Start -200 End 200 Step 70

☑ Write Old Data
At 127 ☑ Old Follows Adjacent

Adjacent Write
Coarse Start 150 Fine Start 85
Coarse Step 10 Fine Stop 40
☐ Rewrite Data Track at each Adjacent Write Fine Step 5
Iterations 1
ID_OD

Offtrack Read
Max 150 Error Threshold 1000
Step 2

Targets
-2 -3 -4

Metric
Bit ER Sample Size 7

Output
☐ Average when Both ☑ Show Plot
☐ Verbose Results, add Bit ER

Figure 5 - 22: Conventional test - Guzik M7 Anaconda configuration setup for the 747 test

The *OTRC* for the conventional write are conducted using the methodologies described in Figures 4-6, 4-7. The test setup is shown in Figure 5-22. Basically, a line that is 15% of the track pitch is drawn and its intersection with the 747 curves is used to determine the *OTRC* of the conventional writing case. The intersection points imply that those are the design track pitches that ensure that as long as the reader head is within 15% of the center track pitch, the *BER* read-back will at least hit the desired value and not be any larger value. In the implementation, the desired *BER* targets are 10^{-2}, 10^{-3} and 10^{-4}.

The method used to determine the *OTRC* for the shingled tracks is to determine the lowest *BER* first. Then based on this offset, determine the distance where the *BER* bathtub curve increases to the 10^{-3} or 10^{-2} range. That distance would be the *OTRC* of the shingled recording system at that particular adjacent track squeeze. Note that the *OTRC* is retrieved from the side where it experienced the track squeeze and not the other side of the track where no track squeezing is experienced. This way of deriving the *OTRC* ensures that the designed track pitch after squeezing is really able to achieve the correct *BER*. This methodology is illustrated in Figure 5-23. All the *OTRC* values will be collected for the different track squeeze and then plotted as the 747 curve. Similar to the conventional recording system case, the 747 curve is then plotted with the 15 *%* track pitch line to determine the design track pitch for that linear density. The designed *OTRC* for the shingled write are then tabulated in table 5-2 to their corresponding linear density.

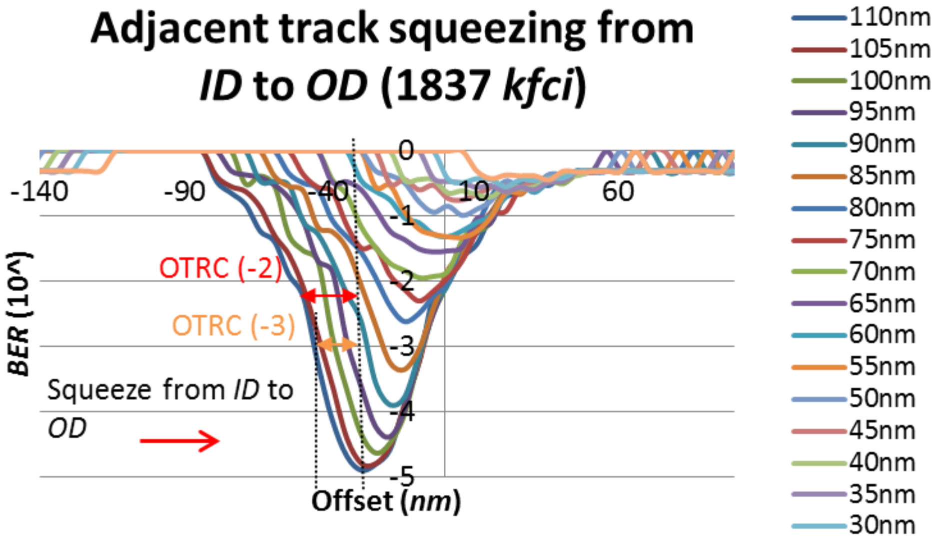

Figure 5 - 23: Illustration of the method of deriving the *OTRC* values to plot the 747 curves from the *BER* plots

Linear density (*kFCI*)	**747 test – *OTRC* (*nm*)**				
	Conventional			**Shingled**	
	***BER* - 10^{-2}**	***BER* - 10^{-3}**	***BER* - 10^{-4}**	***BER* - 10^{-2}**	***BER* - 10^{-3}**
1225	92.13	99.51	101.90	46	68
1327	92.75	98.68	101.61	48	62
1429	90.99	96.34	101.07	47	60.5
1531	92.08	97.87	102.54	51	65
1633	95.28	100.48	106.07	58.5	69
1735	93.59	100.91	104.23	67.5	73
1837	97.66	105.29	113.82	67	79
1939	103.07	119.02	-	83	98
2041	109.30	-	-	95	-

Table 5 - 2: *OTRC* values against the linear density

In total, 9 linear densities have been tested and for each of the densities tested, 5 *OTRC* values in total have been determined for the conventional and shingled recording case by using the methodologies described in Figures 4-7 and 5-23 respectively. As the experiments are done at the *MD* region at 22 *nm* radius, 5400 *rpm*, the areal density could be tabulated accordingly in table 5-3 based on the above track pitch derived using equations 5-6 and 5-7.

Linear density (*kFCI*)	**747 test – Areal density (*Gbpsi*)**				
	Conventional			**Shingled**	
	***BER* - 10^{-2}**	***BER* - 10^{-3}**	***BER* - 10^{-4}**	***BER* - 10^{-2}**	***BER* - 10^{-3}**
1225	337	312	305	676	457
1327	363	341	331	702	543
1429	399	377	359	772	600
1531	422	397	379	762	598
1633	435	412	391	709	601
1735	470	436	422	652	603
1837	477	443	409	696	590
1939	478	413	-	593	502
2041	475	-	-	545	-

Table 5 - 3: Areal density against the linear density

The plots from the tabulated values in table 5-3 are then plotted in Figure 5-24. The purpose of these plots is to know the trend of the areal density against the linear density and to identify the desired linear density to achieve the highest areal density. From the plots, for *BER* of 10^{-2}, the shingled system is able to reach a higher areal density of 775 *Gbpsi* as compared to 475 *Gbpsi*. This is an increase of 163 *%*. In addition, the linear density required is also lesser at 1450 *kBPI*, instead of 1800 *kBPI*. Recording at lower linear density is usually preferred as there tends to be more *ISI*s and thus higher demagnetization fields which would affect the integrity of the recorded data at higher linear recording densities. For the *BER* of 10^{-3} case, the increase in areal density is 134 *%* from 450 to 603 *Gbpsi*. At the time of analysis due to differences in the data processing and collection stage of the shingled write system, data for the BER of 10^{-4} cannot be retrieved together at one go with the BER of 10^{-2} and 10^{-3} case. Whereas for the conventional write system, as we are using the built-in Anaconda 747 test to do the experiments, we are able to easily retrieve the data for BER of 10^{-4}, 10^{-3} and 10^{-2} at one go. The areal density plot for the *BER* of 10^{-4} case for the conventional write case is still attached below for reference purposes.

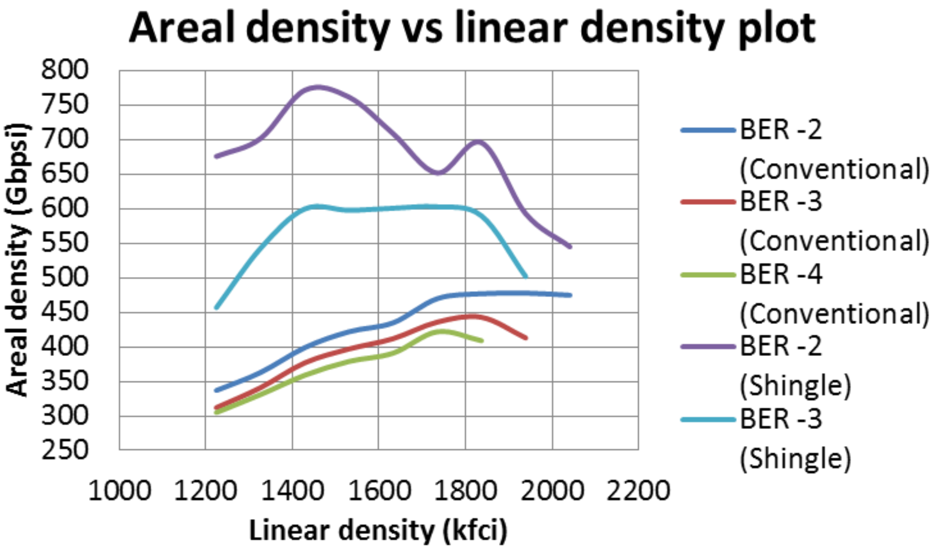

Figure 5 - 24: Comparison of areal density vs linear density for conventional and shingled write systems

System/ *BER*	10^{-2}	10^{-3}	10^{-4}
Conventional	475 *Gbpsi* @ 1800 *kBPI* linear density	450 *Gbpsi* @ 1800 *kBPI* linear density	425 *Gbpsi* @ 1725 *kBPI* linear density
Shingled	775 *Gbpsi* @ 1450 *kBPI* linear density	603 *Gbpsi* @ 1450 *kBPI* linear density	-
% increase in areal density	163%	134%	-

Table 5 - 4: Comparison of acheivable maximal areal density for shingled and conventional recording systems

5.3 Implementation issues in a practical drive

In order for shingled writing to be implemented in a practical drive, several factors are needed to be resolved and optimized. Some of these factors are a) inter-track interference (*ITI*) cancellation during the read process or for offline error recovery when multiple wide read heads are used [78], b) read latency issues if only a single read head is used and thus a need to use stronger *ECC* codes in order to compensate for *ITI* [79], c) random write and write amplification issues thus a need to consider hybrid schemes to buffer data and to improve write performance [80, 81], d) update latency issues [82] and e) the optimum shingling percentage for a practical drive [83]. Note that this list is not exhaustive and not meant to be as well. This section serves more to highlight the possible issues and possible research directions on implementing shingled writing in a practical drive.

5.4 Conclusions

In this chapter, the important recording system parameters like the over-write and reverse over-write ratios, erasure band width and *MWW* using the triple track method, *MRW* using the micro-track method, design track pitch for deriving the achievable areal densities, have been described. Descriptions were also given for the experimental setup, experimental parameters and the equipment, software that has been developed and used to analyze the areal densities achievable via different recording systems: conventional and shingled write.

From the experimental results, it was observed that over-write and reverse over-write ratios retrieved are of the range 40-53 and 33-57 *dB* respectively. These values are considered to be of a good range for commercial data recording and storage.

The achievable areal densities of shingled write system are at 775 *Gbpsi* vs the areal density of 475 *Gbpsi* for the conventional write system case. This is a gain of 163%. From the above experimental results, it is evident that the shingled write system has the capability to surpass the performance of the conventional write system without much advanced technological changes to the head or media configuration as compared to the *HAMR* and *BPMR* systems.

Chapter 6: Conclusions

Current conventional hard disks used for data storage are facing limitations to continue the push for higher areal density. The magnetic recording tri-lemma and the super-paramagnetic limit are some of the crucial factors constraining the size of the magnetic grains. Shingled writing is seen to be one of the possible cost effective ways to improve the areal density yet without many changes to the current conventional recording media and head structure. This thesis's objective was to look at some of the factors affecting the performance of a conventional recording system before looking at the shingled system and the potential areal density gain against a conventional system using a commercial spin-stand.

Ever since its introduction, the hard disk drives have evolved in terms of the technology used and has continued its push for areal density gain. The key important issues affecting magnetic recording are the magnetic recording tri-lemma and the super paramagnetic limit. Because of the super-paramagnetic limit and tri-lemma issue, there is a need to find a compromise between writability, thermal stability and medium *SNR*. To write higher areal densities, magnetic grains cannot be simply reduced in volume without much change to current technology in the writing process or write head or media. With the key issues affecting the areal density push as a background, *HAMR* and *BPMR* are expected to be the next generation of magnetic recording technologies. Both of them have both the technical challenges and cost effective consideration for them to be implemented in the near term of *HDD* products. In this work, we focus on the extension of the conventional perpendicular recording to support the areal density growth in the next 2 to 3 years' time frame. We studied the key issues to implement the shingled writing scheme.

To implement shingled magnetic recording system and future *HAMR* system, the coding and signal processing are the key enabling technologies to deal with the magnetic recording systems with reduced system *SNR*. Recording channels like the *PRML*, *NPML and PDNP* were reviewed. For the channels discussed, input signals have to be converted via equalizers to *PR* signals to reduce the influence of *ISI*s to nearby symbols and to facilitate detection. The conventional *PRML* channel is a *ML* based channel which uses the Viterbi algorithm in its detection. *NPML* was described to be able to improve the performance of *PRML* by including a noise whitening process. *PDNP* further improves the system by including the data dependent noise prediction process in the detection loop. For the detection algorithms, *MAP* based *BCJR* algorithm, had been compared against the widely implemented conventional *ML* based Viterbi algorithm. Error correction code, *LDPC* was also described with brief mention of the *RS* code. For code based implementations, the *LDPC* would be much preferred against the *RS* code especially at higher recording densities. The *PDNP* modification would help to reduce data correlated noise effects. As for the detector, depending on the computational and accuracy requirements, Viterbi or *BCJR* detectors are both possible contenders.

The writing process induced media noise is one of the dominant noise sources in magnetic recording as linear densities increase. Transition jitter which is one of the dominant media noise, was also investigated. The medium noise characteristics and jitter distributions across the track at different offset positions for different writing conditions were investigated by varying the write current. Descriptions were given for the different averaging and data processing methods that had been used to analyze the data. Comparisons between two write/read heads were made and the process of determining the better writer and better writing condition was also gone through.

The track edge erasures occurrence on both conventional and shingled systems was discussed. Important areal density tests, the *BER* and 747 tests, which help to determine the performance and potential areal density of the head-media combination, were also reviewed. With the background knowledge, the track edge noise and its impact to *BER* and *OTRC* were discussed. The writing performance of the recording system was looked at both in the time domain in terms of *TAA* and the spectral domain where data was captured using a spectrum analyzer. The noise characteristics for pushing the areal density more from the track density aspect were discussed.

The implementation of shingled writing and some of the important parameters, *MWW, MRW,* erase band width, overwrite ratio, reverse overwrite ratio that characterize a recording system were described and looked at. Comparing the areal density gain of shingled write vs conventional write systems with a commercial *NPML* channel and spin-stand, for similar media and head configuration, the shingled system was able to achieve an areal density of 775 *Gbpsi* at linear density of 1450 *kBPI* which is much higher as compared to 450 *Gbpsi* at linear density of 1800 *kBPI.*

For future works, research could be conducted on producing shingled write heads that are wider and be able to produce stronger magnetization field. The heads have to be well enclosed with a single side shield enclosing one side of the write head for sharper and stronger writer head field. Media research could also be done to produce media that have smaller grains that are still thermally stable at standard operating temperatures. These media would be expected to have relatively high coercivity and high anisotropy constant, K_u. The media and writer head has to be matched so that the media is still able to be saturated by the writer and the writer has to be able to produce sharp writer head field to overcome the coercivity and have low transition noise. Spin-stand studies could then be conducted to evaluate upon the performance of the head-media configuration using the tests described in the thesis. With properly matched shingled writer and smaller grain size medium, it is expected to realize the areal density towards 1.5 Tb/In2 and even beyond.

I. BIBLIOGRAPHY

[1] "The History of Magnetic Recording," [Online]. Available: http://www.h2g2.com/approved_entry/A3224936. [Accessed 21 Mar 2013].

[2] "IBM 350 Disk Storage Unit," IBM, [Online]. Available: http://www-03.ibm.com/ibm/history/exhibits/storage/storage_350.html. [Accessed 22 Mar 2013].

[3] "History of IBM Magnetic Disk Drives," [Online]. Available: http://en.wikipedia.org/wiki/Early_IBM_disk_storage#Early_IBM_HDDs. [Accessed 22 Mar 2013].

[4] "IBM 1301 Disk Storage Unit," IBM, [Online]. Available: http://www-03.ibm.com/ibm/history/exhibits/storage/storage_1301.html. [Accessed 22 Mar 2013].

[5] "Five Decades of Disk Drive Industry Firsts," [Online]. Available: http://web.archive.org/web/20110726102519/http://www.disktrend.com/5decades2.htm. [Accessed 22 Mar 2013].

[6] "IBM 2310," Computer History Museum, [Online]. Available: http://www.computerhistory.org/groups/storagesig/media/docs/IBM-2310.pdf. [Accessed 22 Mar 2013].

[7] "IBM 3330 Data Storage," IBM, [Online]. Available: http://www-03.ibm.com/ibm/history/exhibits/storage/storage_3330.html. [Accessed 22 Mar 2013].

[8] "IBM 3340 Disk Unit," IBM, [Online]. Available: http://www-03.ibm.com/ibm/history/exhibits/storage/storage_PH11-52.html. [Accessed 22

Mar 2013].

[9] Shan X. Wang and Alexander M. Taratorin, Magnetic Information Storage Technology, Academic Press, 1998.

[10] "IBM 3340 Direct Access Storage Facility, 1973," Computer History Museum. [Online]. Available: http://www.computerhistory.org/groups/storagesig/media/docs/ds_ibm%203340.pdf. [Accessed 22 Mar 2013].

[11] "Timeline of Computer History," Computer History Museum, [Online]. Available: http://www.computerhistory.org/timeline/?category=stor. [Accessed 22 Mar 2013].

[12] "Rodime RO352," Computer History Museum. [Online]. Available: http://www.computerhistory.org/groups/storagesig/media/docs/DS_Rodime%20RO352_120726.pdf. [Accessed 22 Mar 2013].

[13] "PrairieTek 220, 1998," [Online]. Available: http://www.computerhistory.org/groups/storagesig/media/docs/DS_PrarieTek%20220_20121211.pdf. [Accessed 22 Mar 2013].

[14] "A Brief History of the Hard Disk Drive," The PC Guide, [Online]. Available: http://www.pcguide.com/ref/hdd/hist-c.html. [Accessed 22 Mar 2013].

[15] Andreas Moser, Kentaro Takano, David T Margulies, Manfred Albrecht, Yoshiaki Sonobe, Yoshihiro Ikeda, Shouheng Sun and Eric E Fullerton, "Magnetic Recording: Advancing into the Future," *J. Phys. D: Appl. Phys.,* vol. 35, pp. R157-R167, 2002.

[16] "Magnetic Recording Crisis and Challenges," [Online]. Available: http://www.fgarciasanchez.es/thesisfelipe/node5.html. [Accessed 22 Mar 2013].

[17] H.J. Richter and S.D. Harkness IV, "Media for Magnetic Recording Beyond 100 Gbit/In.2," May 2006. [Online]. Available: http://physics.ucsc.edu/~galers/class/Reference/Disk-materials.pdf. [Accessed 22 Mar 2013].

[18] H. Gavrila, "Coupled Granular/Continuous Media," *Proceedings of the Romanian Academy, Series A*, vol. 11, no. 1, pp. 41-46, 2010.

[19] "Basics of Magnetic Recording," Read-Rite, [Online]. Available: http://www.readrite.com/magbasic.html. [Accessed 21 Mar 2013].

[20] "Perpendicular Recording," [Online]. Available: http://en.wikipedia.org/wiki/Perpendicular_recording. [Accessed 21 Mar 2013].

[21] Alexander Q. Wu., Yukiko Kubota, Timothy Klemmer, Tim Rausch, Chubing Peng, Yingguo Peng, Darren Karns, Xiaobin Zhu, Yinfeng Ding, Eric K. C. Chang, Yongjun Zhao, Hua Zhou, Kaizhong Gao, Jan-Ulrich Thiele, Mike Seigler, Ganping Ju and Edward Gage, "HAMR Areal Density Demonstration of 1+ Tbpsi on Spinstand," *IEEE Trans. on Magn.*, vol. 49, no. 2, pp. 779-782, Feb 2013.

[22] Xiaobin Wang, Kaizhong Gao, Hua Zhou, Amit Itagi, Mike Seigler and Edward Gage, "HAMR Recording Limitations and Extendibility," *IEEE Trans. on Magn.*, vol. 49, no. 2, pp. 686-692, Feb 2013.

[23] "Partial Response Signalling," [Online]. Available: http://www.dip.ee.uct.ac.za/~nicolls/lectures/eee482f/08_prsig.pdf. [Accessed 18 Mar 2013].

[24] "Partial Response Maximum Likelihood (PRML)," [Online]. Available: http://www.lintech.org/comp-per/09PRML.pdf. [Accessed 18 Mar 2013].

[25] R. D. Cidecyan, F. Dolvio, R. Hermann, W. Hirt and W. Schott, "A PRML System for Digital Magnetic Recording," *IEEE Journal on Selected Areas in Communications*, vol. 10, no. 1, pp. 38 -56, 1992.

[26] H.Thapar and A.Patel, "A Class of Partial Response Systems for Increasing Storage Density in Magnetic Recording," *IEEE Trans. Magnetics,* vol. 23, no. 5, pp. 3666-3668, 1987.

[27] A. Taratorin, Characterization of Magnetic Recording Systems: A Practical Approach, Guzik Technical Enterprises, 1996.

[28] Erozan M. Kurtas, Jonseung Park, Xueshi Yang, William Radich and Aleksandar Kavcic, "Detection Methods for Data-Dependent Noise in Storage Channels," [Online]. Available: http://citeseerx.ist.psu.edu/viewdoc/download?doi=10.1.1.85.622&rep=rep1&type=pdf. [Accessed 15 Mar 2013].

[29] Viterbi AJ, "Error Bounds for Convolutional Codes and an Asymptotically Optimum Decoding Algorithm," *IEEE Trans. on Information Theory,* vol. 13, no. 2, pp. 260-269, Apr 1967.

[30] Piya Kovintavewat, Inci Ozgunes, Erozan Kurtas, John R. Barry and Steven W. McLaughlin, "Generalized Partial-Response Targets for Perpendicular Recording with Jitter Noise," *IEEE Trans. on Magn.*, vol. 38, no. 5, pp. 2340-2342, Sept 2002.

[31] "Technologiepreis - Technology Award 2005," [Online]. Available: http://www.eduard-rhein-stiftung.de/html/2005/T2005_e.html. [Accessed 16 Mar 2013].

[32] Coker, J. D., E. Eleftheriou, R. L. Galbraith and W. Hirt, "Noise-Predictive

Maximum Likelihood (NPML) Detection," *IEEE Trans. on Magn.,* vol. 34, no. 1, pp. 110-117, Jan 1998.

[33] Eleftheriou, E. and W. Hirt, "Improving Performance of PRML/EPRML through Noise Prediction," *IEEE Trans. on Magn.,* vol. 32, no. 5, pp. 3968-3970, Sept 1996.

[34] Eleftheriou, E. and W. Hirt, "Noise-Predictive Maximum-Likelihood (NPML) Detection for the Magnetic Recording Channel," *Proc. IEEE Intl. Conf. On Commun.,* vol. 1, pp. 556-560, 1996.

[35] J. W. M. Bergmans, S. A. Rajput and F. A. M. Van de Laar, "On the Use of Decision Feedback for Simplifying the Viterbi Detector," *Philips J. Res.,* vol. 42, pp. 399-428, 1987.

[36] V. M. Eyuboglu and S. U. Qureshi, "Reduced-State Sequence Estimation with Set Partitioning and Decision Feed-back," *IEEE Trans. Commun.,* vol. 36, no. 1, pp. 13-20, Jan 1988.

[37] A. Duell-Hallen and C. Heegard, "Delayed Decision Feed-Back Sequence Estimation," *IEEE Trans. Commun.,* vol. 37, no. 5, pp. 428-436, May 1989.

[38] P. R. Chevillat, E. Eleftheriou and D. Maiwald, "Noise Predictive Partial Response Equalizers and Applications," *IEEE Conf. Records ICC'92,* vol. 2, pp. 942-947, 1992.

[39] M. R. Elidrissi, K. K. Teo and K. S. Chan, *Pattern Dependent Noise-Predictive Detection Applied to Spin-Stand Signals,* Singapore: Disk Drive Systems (DDS), Data Storage Institute (DSI), 2012.

[40] Jaekyun Moon and Jongseung Park, "Pattern-Dependent Noise Prediction in Signal-Dependent Noise," *IEEE Journal on Selected Areas in Communications,*

vol. 19, no. 4, Apr 2001.

[41] "BCJR," [Online]. Available: http://site.iugaza.edu.ps/ahdrouss/files/2011/03/SOVA-and-BCJR.pdf. [Accessed 18 Mar 2013].

[42] "Introduction to Bayes Theorem, MAP and ML," [Online]. Available: https://www.cs.princeton.edu/courses/archive/spring02/cs493/lec11.ps. [Accessed 18 Mar 2013].

[43] S. Mahadevan, "Maximum Likelihood vs Bayesian Estimation," University of Massachusetts, [Online]. Available: http://www-edlab.cs.umass.edu/cs689/2010-lectures/ml-vs-bayes-estimation.pdf. [Accessed 18 Mar 2013].

[44] A. Kak, "ML, MAP, and Bayesian — The Holy Trinity of Parameter Estimation and Data Prediction," Purdue University, [Online]. Available: https://engineering.purdue.edu/kak/Trinity.pdf. [Accessed 18 Mar 2013].

[45] Dong-Feng Yuan and Xiao-Hong Shan, "Research on the Viterbi and BCJR Decoding Schemes of Convolutional Codes under Different Sources," *IEEE VTS 53rd*, vol. 2, pp. 1377-1381, 2001.

[46] R. G. Gallager, "Low-Density Parity-Check Codes," M.I.T, Jul 1963. [Online]. Available: http://www.rle.mit.edu/rgallager/documents/ldpc.pdf. [Accessed 18 Mar 2013].

[47] Martyn Riley and Iain Richardson, "Reed-Solomon Codes," [Online]. Available: http://www.cs.cmu.edu/afs/cs.cmu.edu/project/pscico-guyb/realworld/www/reedsolomon/reed_solomon_codes.html. [Accessed 18 Mar 2013].

[48] L. v. d. Pavert, "Reed-Solomon Encoding and Decoding," Turku University of Applied Sciences, 2011. [Online]. Available: http://publications.theseus.fi/bitstream/handle/10024/32913/Reed-Solomon%20Encoding%20and%20Decoding.pdf. [Accessed 18 Mar 2013].

[49] "Decoding Methods," [Online]. Available: http://en.wikipedia.org/wiki/Syndrome_decoding#Syndrome_decoding. [Accessed 18 Mar 2013].

[50] Xiao, Youan, Luo, Chunling and Yang, Chao, "The Comparative Analysis of LDPC and RS Code," *2011 International Conference on Consumer Electronics, Communications and Networks (CECNet),* p. 4510 – 4513, 2011.

[51] Bo Zhou, Li Zhang, Jingyu Kang, Qin Huang, Ying Y. Tai and Shu Lin Meina Xu, "Non-Binary LDPC Codes vs. Reed-Solomon Codes," *Information Theory and Applications Workshop 2008,* pp. 175-184, 2008.

[52] "IDEMA - Advanced Formats Downloads," International Disk Drive Equipment and Materials Association (IDEMA), [Online]. Available: http://www.idema.org/?page_id=2172. [Accessed 18 Mar 2013].

[53] "Low-Density Parity-Check Code," [Online]. Available: http://en.wikipedia.org/wiki/Low-density_parity-check_code. [Accessed 18 Mar 2013].

[54] Bernhard M.J. Leiner, "LDPC Codes – A Brief Tutorial," [Online]. Available: http://www2.engr.arizona.edu/~ece506/readings/project-reading/5-ldpc/LDPC_Intro.pdf. [Accessed 18 Mar 2013].

[55] "NP-Complete," [Online]. Available: http://en.wikipedia.org/wiki/NP-complete. [Accessed 18 Mar 2013].

[56] "Low-Density Parity Check Codes," [Online]. Available: http://users.ece.gatech.edu/~swm/ECE6606/Steveldpc1.pdf. [Accessed 18 Mar 2013].

[57] Jian Sun, "An Introduction to Low Density Parity Check (LDPC) Codes," West Virginia University, 3 Jun 2003. [Online]. Available: http://materias.fi.uba.ar/6624/index_files/outline_archivos/slideldpc.pdf. [Accessed 18 Mar 2013].

[58] Shiming Ang, Chun Lian Ong, Zhimin Yuan and Chee Khiang Pang, "Writing Process Induced Media Noise Measurement," *IEEE Trans. on Magn.,* vol. 48, no. 5, pp. 1738-1743, May 2012.

[59] Shiming Ang, Chun Lian Ong, Zhimin Yuan and Chee Khiang Pang, "Probabilities of Transition Jitter at Different Off-Track Positions," *IEEE Trans. on Magn.* (to be published).

[60] M. Shiimoto, H. Katada, Y. Urakami, M. Hashimoto, M. Sugiyama, T. Na, Takayuki Ichihara and Kazuhiro Nakamoto, "Effect of Transition Curvature and Track Edge Fluctuation on Track Edge Noise for Narrow Track Recording," *IEEE Trans. on Magn.,* vol. 46, no. 6, pp. 1428-1431, Jun 2010.

[61] S. N. Piramanayagam, H. K. Tan, M. Ranjbar, S. K. Wong, Sbiaa, R. and Chong, T. C., "Magnetic Interaction in Perpendicular Recording Media with Synthetic Nucleation Layers," *Applied Physics Letters,* vol. 98, no. 15, Apr 2011.

[62] Zhi-Min Yuan, Shengbin Hu, Guchang Han and Bo Liu, "Relaxed Head Media Spacing by High Resolution DDSV Reader at Multi-Tb/In2 Areal Density," *IEEE Trans. on Magn.,* vol. 47, no. 7, pp. 1974-1980, Jul 2011.

[63] M. Hashimoto, M. Salo, Y. Ikeda, A. Moser, R. Wood and H. Muraoka, "Analysis of Written Transition Curvature in Perpendicular Magnetic Recording from Spin-Stand Testing," *IEEE Trans. on Magn.*, vol. 43, no. 7, pp. 3315-3319, Jul 2007.

[64] D. J. Seagle, M. C. Barsotti, M. L. Osborn and V. M. Tobin, "Transition Curvature Analysis," *IEEE Trans. on Magn.*, vol. 35, no. 2, p. 619–624, Mar 1999.

[65] F. Liu, S. Li, D. Bai, H. Mendez, T. Pan, D. Han and S. Mao, "Effect of Track Asymmetry and Curvature on Shingle Writing Scheme," *J. Appl. Phys.*, vol. 109, no. 7, Mar 2011.

[66] G.F. Hughes, et. al., "Time Interval Analysis Errors in Measuring Recording Media Transition Jitter," *IEEE Trans. on Magn.*, vol. 33, no. 6, pp. 4475-4481, Nov 1997.

[67] M. Hashimoto, et. al., "Magnetic Cluster Size Distribution and its Relation to Read/Write Performance from Spinstand Testing," *IEEE Trans. on Magn.*, vol. 45, no. 10, pp. 3718-3721, Oct 2009.

[68] S.W. Yuan, et. al., "Statistical Data Analysis of Magnetic Recording Noise Mechanisms," *IEEE Trans. on Magn.*, vol. 28, no. 1, pp. 84-92, Jan 1992.

[69] H. Katada, et. al., "Head/Media Integration Challenge toward 1Tb/In2 Perpendicular Recording," *IEEE Trans. on Magn.*, vol. 46, no. 3, pp. 798-803, Mar 2010.

[70] Y. Zhou and J. G. Zhu, "Effect of Pole Tip Size on Perpendicular Recording Head Remanence," *IEEE Trans. on Magn.*, vol. 41, p. 4449–4453, Dec 2005.

[71] B. Valcu, B. Allimi, A. Dobin, R. Lynch, H. Richter and R. Brockie, "Effect of

Media Reversal Mode on Head Footprint," *IEEE Trans. on Magn.*, vol. 44, pp. 3412-3415, Nov 2008.

[72] A. Taratorin and K. Klaassen, "Media Saturation and Overwrite in Perpendicular Recording," *IEEE Trans. on Magn.*, vol. 42, pp. 157-162, Feb 2006.

[73] Zhi-Min Yuan, Chun Lian Ong, Shiming Ang, Siang Huei Leong and Mingsheng Zhang, "Writer Footprint Measurement on Spinstand and Media Transition Curvature Characteristics," *IEEE Trans. on Magn.*, vol. 48, no. 5, pp. 1738-1743, May 2012.

[74] Zhen Jin, Michael Salo and Roger Wood, "Areal-Density Capability of a Magnetic Recording System using a “747” Test Based Only on a Data-Block Failure-Rate," *IEEE Trans. on Magn.*, vol. 44, no. 11, pp. 3718-3721, Nov 2008.

[75] R. S. Beach and P. I. Bonyhard, "An Off-Track Capability Model including Noise," *IEEE Trans. on Magn.*, vol. 34, no. 4, Jul 1998.

[76] Shaoping Li, Huaan Zhang and W. Zhu, "A General Approach for Overwrite Spectra," *J. Appl. Phys.*, vol. 93, no. 10, 2003.

[77] E. E. Lin, S. Li, D. Bai, S. Mao, Bo Zhang, Stoev, K. and Tao Pan, "High Precision Erase Band Measurement with Four Written Tracks," *IEEE Trans on Magn.*, vol. 47, no. 10, p. 2984 – 2987, Oct 2011.

[78] F. H. Erich, M. George, P. Jongseung, J. Ming, J. W. Kurt and X. L. Yuan, "Intertrack Interference Cancellation for Shingled Magnetic Recording," *IEEE Trans. on Magn.*, vol. 47, no. 10, pp. 3698-3703, Oct 2011.

[79] S. V. Kalyana, D. Guiqiang, X. Ningde and Z. Tong, "Reducing Read Latency

of Shingled Magnetic Recording with Severe Inter-Track Interference using Transparent Lossless Data Compression," *IEEE Trans. on Magn.*, 2013.

[80] W. Jiguang, Z. Nannan, Z. Yifeng, W. Jibin, M. Yu, C. Peng and X. Changsheng, "High Performance and High Capacity Hybrid Shingled-Recording Disk System," *IEEE International Conference on Cluster Computing*, pp. 173-181, 2012.

[81] W. Jiguang, W. Jibin, C. Xiang and T. Zhihu, "An Efficient Mapping Scheme for Shingled Recording Hard Drives," *International Conference on Industrial Control and Electronics Engineering*, 2012.

[82] S. V. Kalyana, D. Guiqiang and Z. Tong, "Techniques Mitigating Update-Induced Latency Overhead in Shingled Magnetic Recording," *IEEE Trans. on Magn.*, vol. 48, no. 5, pp. 1899-1905, May 2012.

[83] C. Selvan and S. Pornchai, "A Spinstand Study in Determining the Optimum Shingling Percentage for Shingled Write Recording," *IEEE Trans. on Magn.*, vol. 49, no. 6, pp. 2544-2547, June 2013.

II. AUTHOR'S PUBLICATIONS

1. A. Shiming, O. Chun Lian, Y. Zhimin, "Writing Process Induced Media Noise Measurement," in *Proceedings of IEEE International Magnetics Conference*, FH-09, Vancouver, Canada, 7-11 May 2012.
2. Shiming Ang, Chun Lian Ong, Zhimin Yuan and Chee Khiang Pang, "Writing Process Induced Media Noise Measurement," *IEEE Trans. on Magn.*, vol. 48, no. 5, pp. 1738-1743, May 2012.
3. A. Shiming, O. Chun Lian, Y. Zhimin, "Probabilities of Transition Jitter at Different Off-Track Positions," in *Proceedings of the 12th Joint MMM-Intermag Conference*, HW-01, Chicago, IL, USA, 14-18 January 2013.
4. Shiming Ang, Chun Lian Ong, Zhimin Yuan and Chee Khiang Pang, "Probabilities of Transition Jitter at Different Off-Track Positions," *IEEE Trans. on Magn.* (to be published).
5. Zhi-Min Yuan, Chun Lian Ong, Shiming Ang, Siang Huei Leong and Mingsheng Zhang, "Writer Footprint Measurement on Spinstand and Media Transition Curvature Characteristics," *IEEE Trans. on Magn.*, vol. 48, no. 5, pp. 1738-1743, May 2012.